Akita University

COPPER-SILVER MINERALIZATION IN THE KHOEMACAU ZONE 5 DEPOSIT, KALAHARI COPPERBELT, NORTHWEST BOTSWANA

a PhD Dissertation

by

Mpho Keeditse

ID No. 6519101

Submitted to

Department of Geosciences, Geotechnology and Materials Engineering for Resources

Graduate School of International Resource Science

Akita University, Japan

2022

Akita University

TABLE OF CONTENTS

Akita University

Akita University

ABSTRACT

The Zone 5 Cu-Ag deposit in northwest Botswana extends for 4.2 km in length and contains a resource of 100 Mt grading 2% Cu and 21g/t Ag. Zone 5 is the main deposit in the Khoemacau district of the Kalahari Copperbelt. Despite the recent studies of mineralization in the Kalahari Copperbelt in Botswana, the fundamental question on the origin of the Zone 5 deposit remains contentious. This thesis presents a documentation of Cu-Ag mineralization across the width of the Zone 5 and contributes to a better understanding of the origin of the Cu-Ag deposit and the development of improved exploration models.

At Zone 5, the redox-buffered metal-zoned ore body (~10 m average thickness) is preferentially hosted by chemically reduced metasedimentary rocks overlying oxidized, hematite-bearing arkosic sandstone. Locally, the ores are concentrated along bedding and foliation planes and within structures such shear fabrics, veins, and metamorphic cleavage. A combination of detailed microscopic, SEM-EDS, EPMA analyses, indicate that the Cu-Ag deposit is controlled by both lithologic and structural parameters and formed from a multi-stage mineralization history that includes both diagenetic and epigenetic events.

The early, diagenetic mineralizing event is characterized by fine-grained stratiform pyrite, including recrystallized framboidal pyrite, intergrown with diagenetic mineral assemblages in the host-rock. Diagenetic pyrite is in textural equilibrium with chalcopyrite, sphalerite, galena, and (Fe-Co-Ni) sulfarsenide. These minerals were subsequently overprinted by a more intense, multi-stage, structurally controlled hydrothermal Cu-Ag mineralization event related to the Damaran orogeny (~600-480 Ma).

Mineral chemistry results reveal an apparent overlap in trace metal associations (Cu, Fe, As, Zn, Pb, Ni, Co) between the two mineralizing events, which can be explained by remobilization of precursor sulfides. Microscopic and micro-XRF data indicate that the major Ag-carriers in the ore are chalcocite, covellite, and bornite. The main hydrothermal Cu-Ag mineralization precipitated from hot (P corrected Th = ~236-265°C), high salinity (19-24.6 wt. % NaCl equiv.) hydrothermal ore fluids.

The $\delta^{34}S$ values of diagenetic pyrite range from -35.8 to +11.4 ‰, whereas those of hydrothermal epigenetic sulfides, including pyrite, range from -28.0 to +3.0 ‰. These results suggest that hydrothermal sulfides acquired some bacterially-reduced sulfur from earlier-formed minerals. The $\delta^{18}O$ and $\delta^{13}C$ values of quartz and calcite associated with the hydrothermal mineralization are typical of Neoproterozoic sediment-hosted Cu-Ag deposits. However, the $\delta^{18}O$ isotopic values of the calcite gangue are anomalously depleted, likely due to recrystallization under metamorphic conditions.

Akita University

ACKNOWLEDGEMENTS

I would like to begin by expressing my utmost gratitude to my advisors Profs. Antonio Arribas and Yasushi Watanabe for their guidance, mentorship, and inspiration they have instilled in me. I cannot thank Associate Professor Dr. Takuya Echigo enough for the technical training and assistance he offered me during my various laboratory analyses. The technical support I was offered by Dr. Shogo Aoki is greatly appreciated.

This work would not have been possible without the funding provided by Japan International Corporation Agency (JICA) through the KIZUNA scholarship (2018-2022) awarded to me. Khoemacau Copper Mining (KCM) Ltd. Is immensely thanked for the permission to publish the documentation of the Zone 5 Cu-Ag deposit. The technical support and intellectual inputs from the KCM Ltd. staff, made this work materialize.

I am thankful to Hannah Buamono of the University of Texas at El Paso for support with the micro-XRF analyses. I also would like to acknowledge Dr. Hinako Sato of the Akita University for support with the sulfur isotope analyses.

I also would like to convey my sincere gratitude to my thesis panel (Profs. Yasushi Watanabe, Tsukasa Ohba, and Andrea Agangi) for their rigorous assessment of my thesis and their constructive and insightful comments that greatly improved the thesis.

No mention of thanks would be complete without mentioning my lovely family (TJ and Base), for their constant unwavering support, particularly during the most challenging time of our lives caused by the COVID-19 pandemic.

Akita University

Chapter 1

INTRODUCTION

1.1 Introduction

Copper is one the key critical metals for carbon-free energy generation (developing battery technologies and 'green energy revolution'). Copper is primarily sourced through the exploitation of porphyry and sediment rock-hosted copper deposits which, together, account for over 80% of known copper resources (Singer, 2017). As opposed to the well-advanced understanding of porphyry systems (e.g. Sillitoe, 2010; Wilkinson et al., 2015), processes associated with formation of the sedimentary-rock hosted copper systems are still not fully understood. It is therefore imperative to understand the processes through which copper and other critical metals are deposited in sediment-hosted stratiform copper systems to counteract the declining trend of global discoveries and secure a future supply of the metal.

1.2 Sedimentary rock-hosted stratiform copper deposits

The sediment-hosted stratiform Cu deposits account for approximately 23 % of the global Cu production and known reserves, in addition to being significant sources of cobalt and silver (Hitzman et al., 2005). These deposits are typically a product of movement of evolving moderate to highly saline oxidized, copper-bearing fluids across a reduction front that results in

the precipitation of copper sulfides within an intracratonic basin that becomes hydrologically closed (Hitzman et al., 2010; Fig. 1.1). The distribution of these deposits is fundamentally controlled by chemical and permeability frameworks upon which ore fluids are superimposed (Selley et al., 2018). Generally, sediment-hosted copper deposits occur in fault-controlled sedimentary basins linked to intracontinental rifting and consist of relatively thin (generally <30 m and commonly <3 m) orebodies that are peneconcordant with lithologic layering (Hitzman et al., 2010). Despite the ongoing discussions on the topic, it is commonly believed that the red-bed sedimentary rocks which contain iron oxyhydroxides (capable of weakly binding metals) are the plausible metal sources, with some authors proposing proximal basement rocks as sources. Evaporite sequences, reduced seawater, and hydrogen sulfide-bearing petroleum are the main sources of sulfur. Sulfide precipitation results from interaction of the ore fluid with either in-situ or mobile reductant. The in-situ reductant may be present in form of diagenetic pyrite or bacterially reduced sulfate whereas the mobile reductant would commonly be trapped hydrocarbons that have accumulated in structural trap sites (Hitzman et al., 2010).

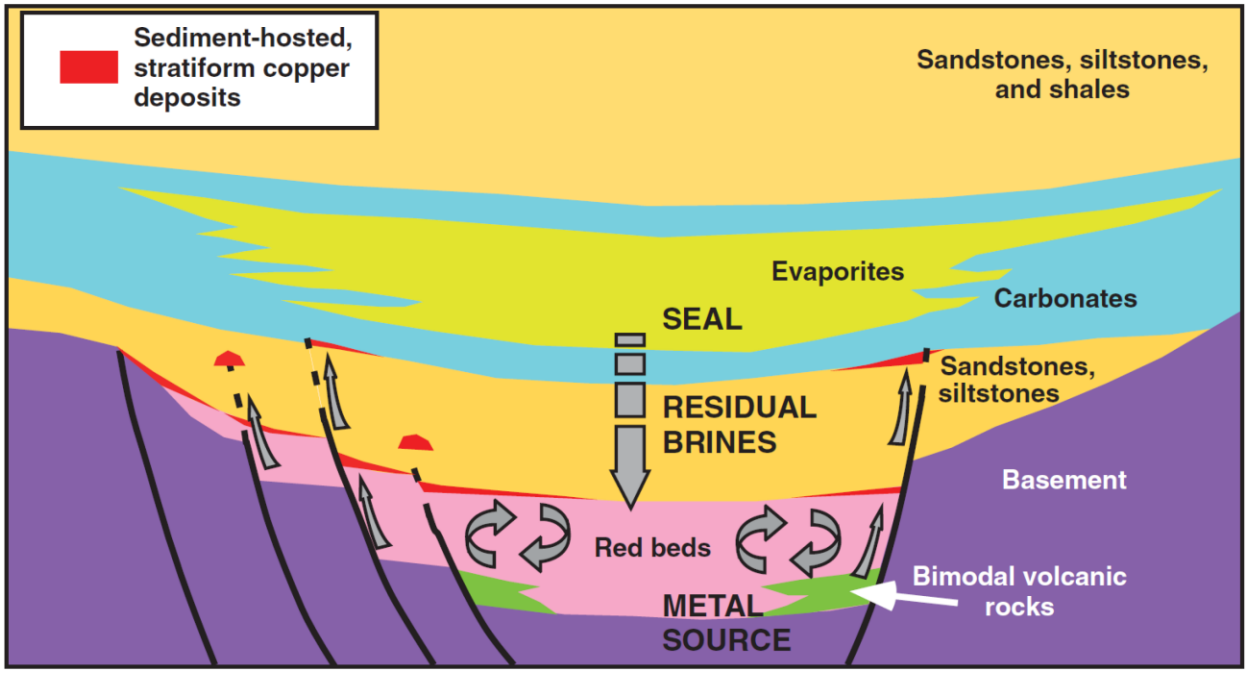

Figure 1.1 Schematic cross section across an intracratonic, hydrological closed basin that is typical of those hosting sediment-hosted stratiform copper deposits (mostly applicable for supergiant and giant deposits). The diagram highlights the various geologic factors and processes involved in mineralizing system. Cu (+ other metals) is derived from red-beds, bimodal volcanics and/or basement rocks. Reduced, organic-rich siltstones and mudstones provide a redox trap for the oxidized Cu-rich brines, resulting in ore precipitation. From Hitzman et al. (2010).

The temporal distribution of this deposit-type has been controlled by global-scale geologic processes throughout the Earth's history, with no deposits forming until after the early Paleoproterozoic Great Oxidation Event (~2.4 Ga; Fig. 1.2). Subsequent to the oxygenation of the atmosphere, oxidized red beds (the likely source of Cu in majority of the basins) became prevalent and basinal brines became oxidized, often sulfate-rich as opposed to H_2S (Hitzman et al., 2010; Large et al., 2017). This transition to oxidizing atmospheric conditions was fundamental in promoting the diagenetic 'reddening' of basal siliciclastic sequences, a process

thought to have significantly increased the proportion of the bulk rock Cu content that is 'available' to pore fluids for remobilization (Brown, 2009).

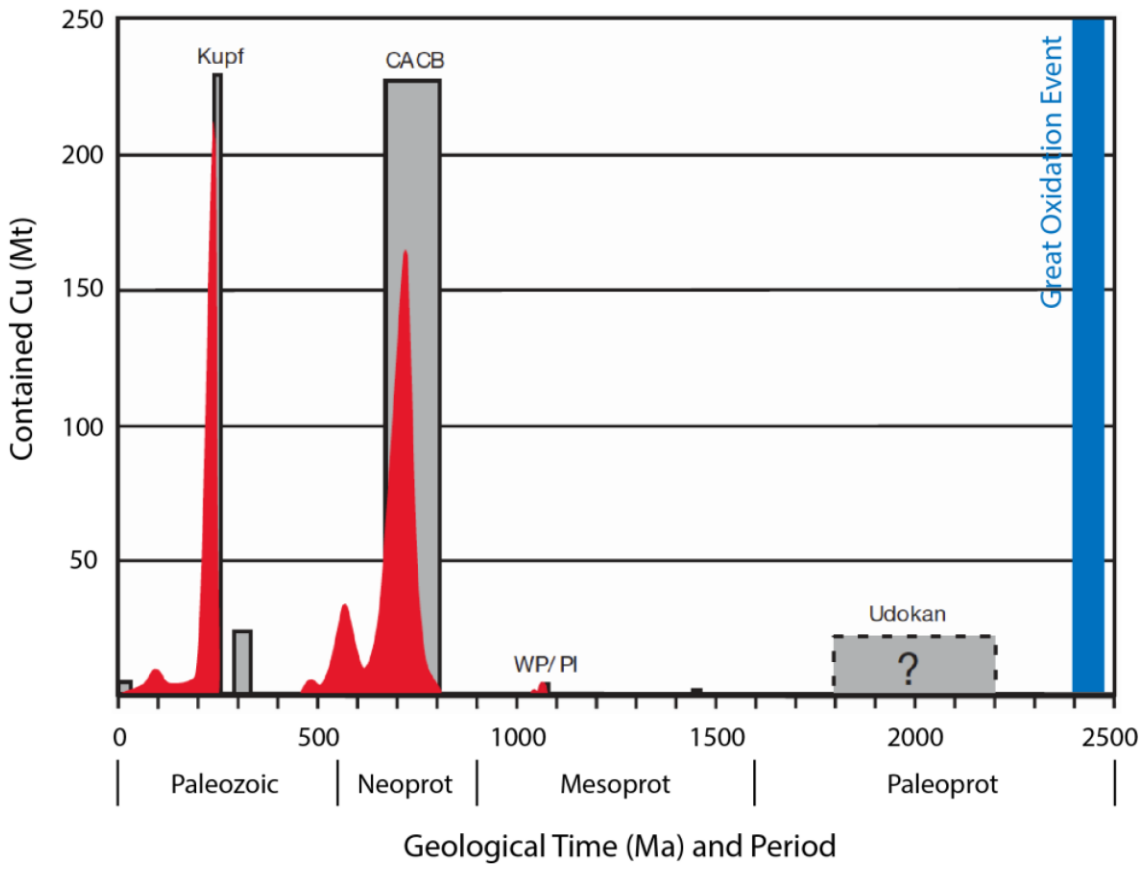

Figure 1.2 Temporal distribution of supergiant and giant sediment-hosted stratiform Cu deposits. Grey bars represent the contained Cu (Mt) and approximate age of each of the deposits. The red curve illustrates the probable age of mineralization. Adapted from Hitzman et al. (2010).

1.3 Thesis rationale

Successful past exploration results (e.g., Anglovaal South West Africa, Pty, 1967-1971; U.S. Steel 1972-1978; Anglo-American Corporation, 1990-1993) in the Kalahari Copperbelt (KCB) and a favourable investment environment in the country have triggered a renewed interest on mineral exploration in the Ghanzi Ridge zone of the KCB in Botswana (Fig. 1.3). Early explorers outlined a number of deposits including the Ngwako Pan deposit (now the area of the Boseto mine within the Khoemacau Cu district) with an inferred reserve of 20 Mt at 2% Cu and 39 g/t Ag (U.S Steel 1978; Schwartz et al., 1995). The Boseto copper deposit was the second in the Kalahari Copperbelt (KCB), to go into commercial production in 2012 after the closure of the Klein Aub Copper Mine in Namibia in 1987. However, the activities of these early explorers were largely restricted to areas with a limited thickness of the Kalahari Sands that cover the Kalahari Group basement rocks.

Subsequent to renewed interest in the Kalahari Copperbelt, particularly the Ghanzi-Chobe zone, Cupric Canyon Capital since acquiring Khoemacau project (KCM) in 2013 have delineated and expanded the Zone 5' s high-grade Cu-Ag resource whose mineralization is relatively continuously for more than 4 km. Khoemacau project presented a great opportunity for research on the copper-silver deposits within the KCM property.

Recent advances in understanding the geology and origin of Cu-Ag mineralization in the KCB have resulted from in-depth studies on subjects spanning regional- to deposit-scale characterization and delineation of the KCB (e.g. Schwartz et al., 1995; Morgan, 2013; Shepard,

2013; Gorman, 2014; Lehmann et al., 2015; Hall et al., 2018b), depositional environment and geochronology (e.g. Modie, 1996, 2000; Hall et al., 2018a, 2021) and provenance and distribution of metals (e.g. Schwartz et al., 1995; Modie et al., 1996, 2000; Kelepile et al., 2017, 2020; Hall et al., 2018a). Among these studies, there is agreement that the litho-structural control, permeability, metal source, sulfur source, and a reductant (in-situ or mobile) were key elements for precipitation of the Cu-Ag ores. It has also been documented that Cu-Ag mineralization is associated with regional fold limbs and hinges, rendering the structural setting a key element in the exploration for potential ore trap sites (e.g. Hall et al., 2018b).

Despite this progress, the understanding of genesis of the Cu-Ag mineralization the Khoemacau metallogenic district remains contentions, particularly the metallogenic models which are a fundamental component in unravelling the origins of any ore deposit. Models advanced for the KCM comprise syngenetic-diagenetic (e.g. Ruxton, 1986; Ruxton and Clemmey, 1986; Schwartz et al., 1996; Borg, 1995), purely epigenetic (Sillitoe et al., 2010; Maiden and Borg, 2011, Hall et al., 2018b) and two (or more) stage models requiring overprinting and/or remobilization of a diagenetic precursor or early hydrothermal base metals sulfides (Borg and Maiden, 1986b, 1987, 1989; Borg, 1988, 1995; Walraven and Borg, 1992; Van der Heever et al., 2009; Hall et al., 2021; Keeditse et al. *under review*). The disagreement between these models is in part linked to challenges associated with documenting detailed in-depth parageneses, particularly at deposit scale.

The Zone 5 deposit being the most economically significant and currently the newest operational Cu mine in the KCM, present an opportunity to carry out a detailed study of the deposit to improve the understanding of its origins. The objectives of this study are 2-fold: first,

is to better document the mineralization across the width of the deposit particularly silver mineralization and distribution of sulfide minerals, through drill core examination and various petrographic investigations. Secondly, improve the understanding of the genesis of a hydrothermal system, such as the Zone 5, in order identify and develop exploration tools.

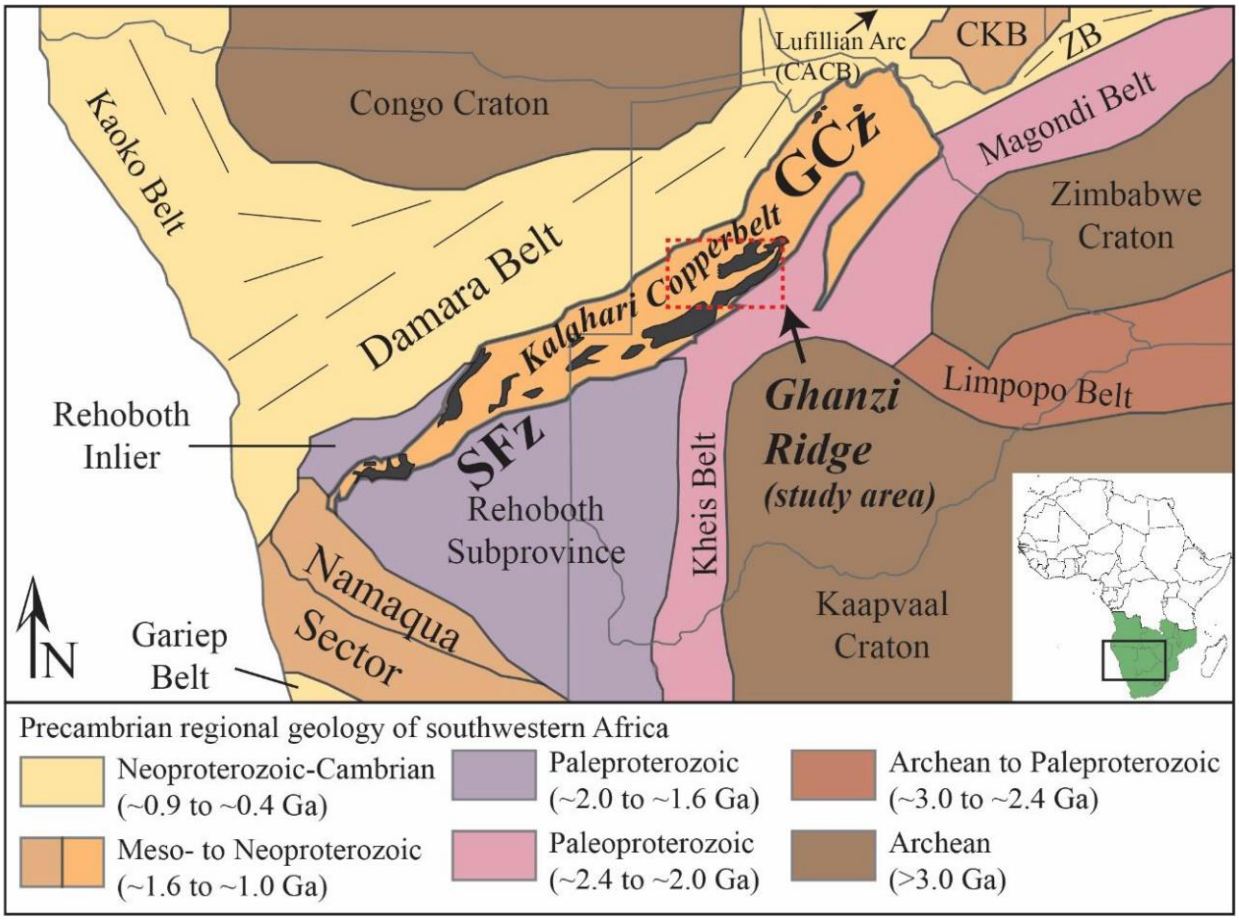

Figure 1.3 Location map of the Ghanzi Ridge Zone (within which the study area lies) within the Precambrian crustal framework of Southern Africa. Adapted from Hall (2017) and references therein.

Akita University

Chapter 2

REGIONAL GEOLOGIC BACKGROUND

2.1 Southern African copperbelts

The Kalahari Copperbelt (KCB) in Botswana and Namibia is broadly considered a n equivalent of the Central African Copperbelt (CACB) that straddles Zambia and the Democratic Republic of Congo (Sillitoe et al., 2010; Fig. 2.1). Although the CACB is a supergiant sedimentary rock-hosted stratiform Cu district (endowment of >270 Mt Cu, + > 5Mt Co) compared to the considerably smaller KCB, the two copperbelts share similarities with respect to age, geotectonic position, and depositional environment (Schwartz et al., 1996). The latest U-Th-Pb ages reported in the Kalahari Copperbelt indicate that the ore-grade Cu mineralization occurred during the Pan-African (~600-480 Ma) fold-thrust evolution of the KCB and were broadly synchronous with the Cu-Co mineralization event in the CACB (Hall et al., 2021).

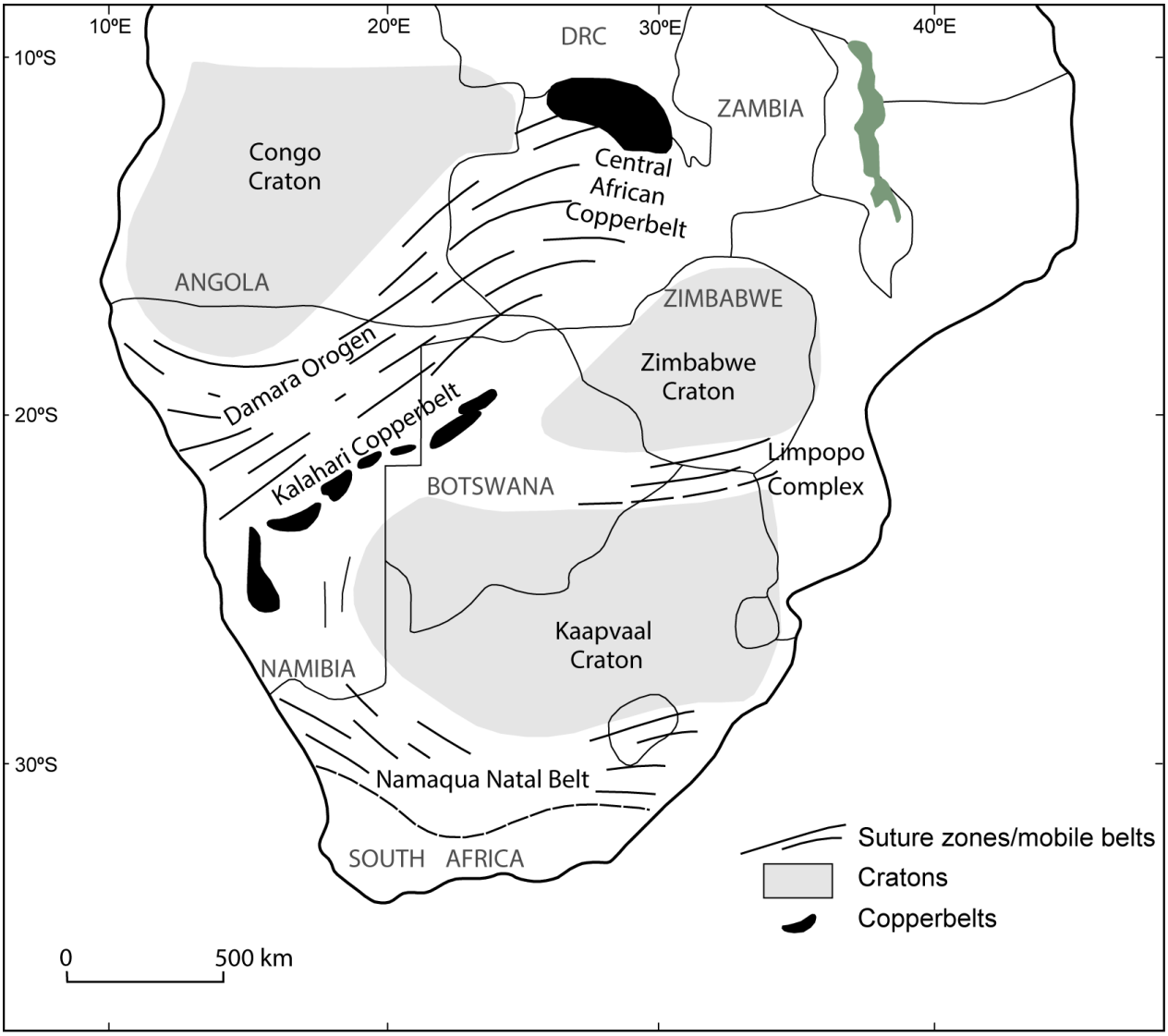

Figure 2.1 Sub-continental map showing the locations of the Kalahari Copper belt and the Central African Copperbelt (modified from Median and Borg, 2011).

2.2 The Kalahari Copperbelt in Botswana

The Kalahari Copperbelt is located in the Neoproterozoic Damara fold-and-thrust belt (Schwartz et al., 1995, 1996; Lehmann et al., 2015; Hall et al., 2018b) that occupies the north-western margin of the Kalahari Craton (Borg and Maiden, 2011; Lehmann et al., 2015; Fig. 2.2). It is defined by a series of sedimentary rock-hosted Cu-Ag deposits within a NE-trending 1000

km-long by up to 250 km-wide Meso-to Neoproterozoic geophysically-linked volcano-sedimentary basins that stretch intermittently from Namibia to Botswana (Lehmann et al., 2015). Previous workers (e.g. Borg and Median, 1989, Schwartz et al., 1996) attributed the Copperbelt descriptor to the widespread stratabound and structurally controlled Cu-Ag deposits that accumulated within rift-related volcano-sedimentary basins. In Botswana, the fold belt is termed the Ghanzi-Chobe zone (GCZ), whereas in Namibia it is known as the Southern Foreland Zone (SFZ) (e.g. Revees and Hutchins, 1982; Meixner, 1983; Miller, 2008; Lehmann et al., 2015; Fig. 2.2).

The GCZ records bimodal magmatism at 1106-1085 Ma (Schwartz et al., 1995; Hall et al., 2018a) and inversion at ~600-480 Ma associated with the Damaran orogenesis (e.g. Schwartz et al., 1996; Modie, 1996; Gray et al., 2008). The Pan African Damara orogenesis formed the present-day structural configuration of the KCB. The KCB is characterized by upright to slightly inclined, overturned fold systems with steeply dipping axial planes having hinge lines that are sub horizontal and/or plunge to both northeast and southwest (e.g. Schwartz et al., 1995, Modie, 1996; Lehmann et al., 2015; Hall et al., 2018b). Subsequently, the rocks were metamorphosed to regional lower greenschist facies (muscovite-chlorite-actinolite-epidote-clinozoisite-calcite-rutile), locally approaching amphibolite facies (Carney et al., 1994; Schwartz et al., 1995; Miller, 2008; Lehmann et al., 2015); however, the age of metamorphism is unknown in the GCZ.

Peak metamorphism has been constrained at ~530 Ma in the adjacent Damara belt of Namibia (Ahrendt et al., 1978; Gray et al., 2008; Miller, 2008). Despite being widely concealed by tens of meters of the Kalahari Sands which precludes direct correlation between known Cu-

Ag districts (Lehmann et al., 2015), lithostratigraphic correlation of the two magnetic domains of the KCB have been extensively studied by numerous recent researchers (e.g. Schwartz et al., 1995, Lehmann et al., 2015; Hall et al., 2017).

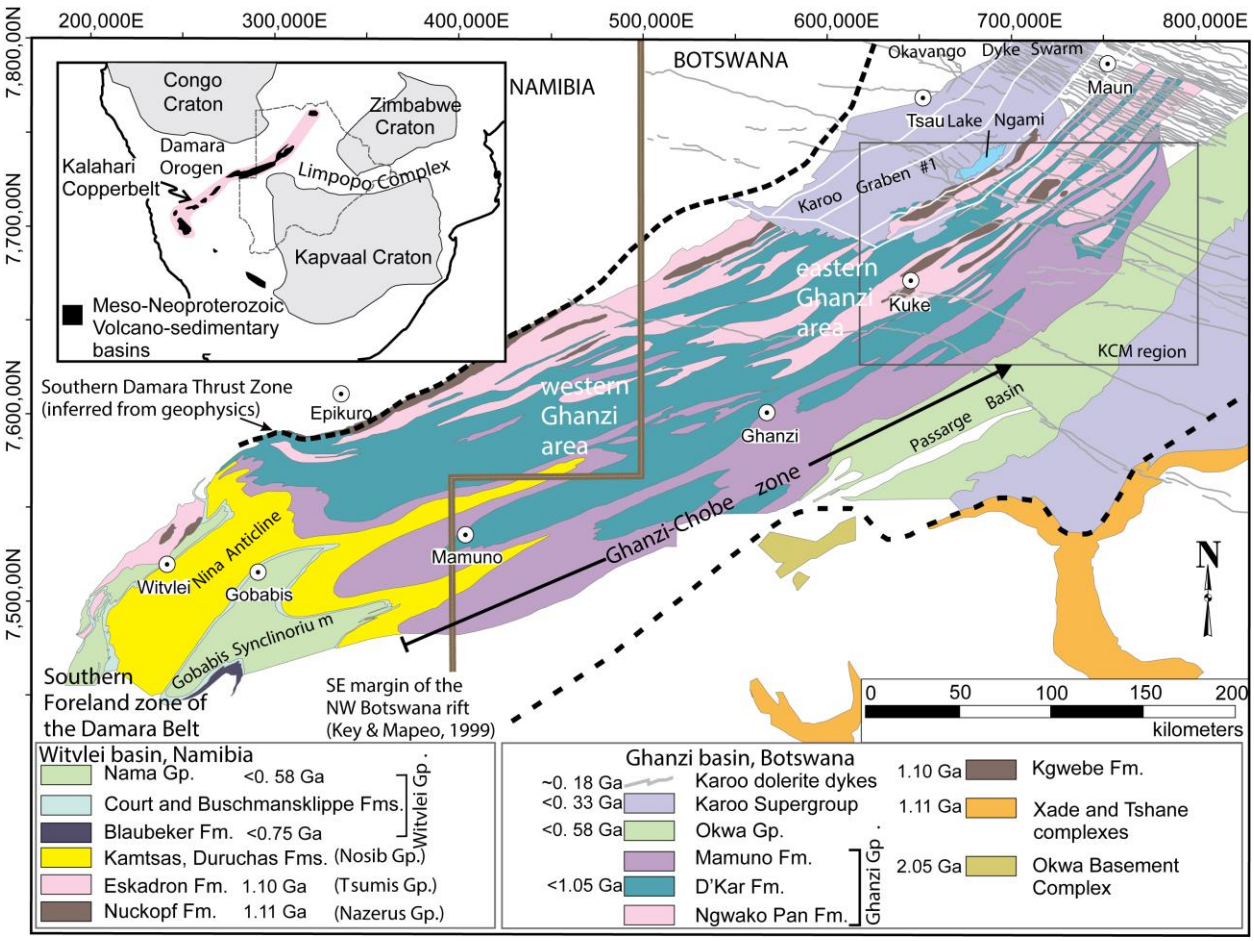

Figure 2.2 Geologic setting and generalized map of the Kalahari Copperbelt, showing the geology of the Ghanzi basin in Botswana and geology of the Witvlei basin in Namibia. Adapted after Lehmann et al. (2015). Basement rocks proximal to the Ghanzi basin are also shown.

2.2.1 Stratigraphy and basin growth

The 7- to 10-km thick GCZ (Lehmann et al., 2015; Hall et al., 2018b; Fig. 2.3) comprises a basal rift-related bimodal volcanic suite (the Kgwebe Formation), which is unconformably

overlain by a thick (>5 km), rift-related succession of continental to marine metasedimentary rocks (the Ghanzi Group; Modie, 1996). In Botswana, this sequence is largely obscured by tens of meters of Cenozoic to recent Kalahari Sands. The tectonic evolution of the GCZ can be divided into two broad phases: the first phase is linked to extensional tectonics and intracratonic rifting in conjunction with bimodal magmatism (deposition of basal Kgwebe Formation) and associated lacustrine to fluvial systems (Modie, 1996, 2000; Fig. 2.3). The Ghanzi Group is assigned to the second phase of basin evolution and is responsible for continued rifting (basin enlargement) which led to deposition of a siliciclastic sedimentary and carbonate packages, culminating in a marine transgression (Modie, 1996).

The Kgwebe Formation has been defined as a prominent 250-km long structural anticlinorium within the central section of the GCZ (Schwartz et al., 1996; Fig. 2.2). The volcanic rocks of this formation consist of within-plate, low Ti-P continental tholeiite and post-orogenic within-plate, high-K rhyolite (Kampunzu et al., 1998; Hall et. al., 2018a), which are intercalated with a metasedimentary package (e.g. Lehmann et al., 2015). As for the geochronology of this formation, the Mabeleapodi Hills porphyritic rhyolite yielded a U-Pb zircon (ID-TIMS) crystallization age of 1106 ± 2 Ma (Schwartz et al.,1995) and rhyolite from Goha Hills produced a Rb-Sr (whole-rock isochron) age of 981 ± 43 Ma (Key and Ruddle, 1981) and a U-Pb (ID-TIMS) age of 1106.2 ± 3.6 Ma (Key and Ayres, 2000). Recently Hall et al. (2018a) reported a U-Pb zircon (LA-ICPMS) age of 1085.5 ± 4.5 Ma for the Makgabana Hills porhyritic rhyolite, thus providing the new maximum depositional age for the overlying Ghanzi Group.

The Ghanzi Group is formally subdivided into four formations, in ascending order: the Kuke, Ngwako, D'kar, and Mamuno Formations, (Modie, 1998). The Kuke Formation is composed of

cross-bedded quartz arenite and conglomerate containing reworked clasts from the disconformably underlying Kgwebe Formation rhyolite (Modie, 2000). The overlying Ngwako Pan Formation varies in thickness between 2 and 4 km and consists of basal grey wacke followed by hematite-bearing red sandstone and arkose that are locally interbedded with pebbly layers, granule conglomerate and red shale (Schwartz et al., 1995; Modie, 2000; Lehmann et al., 2015).

The cupriferous D'Kar Formation is a marine siliciclastic and carbonate sequence with approximate thickness of 1500 m (Schwartz et al., 1996). Basal rocks of the D'Kar Formation are primarily reduced-facies, parallel-laminated grey-green siltstone, carbonaceous-rich siltstone, mudstone, and sandstone with subordinate marlstone/limestone layers (Schwartz et al., 1995; Modie, 1996; Hall, 2013). The upper portion of the D'Kar Formation is composed of oxidized cross-bedded sandstone overlain by chemically-reduced mudstone and siltstone (Schwartz et al., 1995; Hall, 2013).

The Mamuno Formation which lies conformably on the D'Kar Formation has thickness of between 4 and 6 km and is made up of purple, fine-to medium-grained arkosic sandstone interbedded with siltstone, mudstone, and limestone (Litherland, 1982; Modie, 1996). The stratigraphy culminates with syn-tectonic Damaran age (578 ± 12 Ma; Ramokate et al., 2000, Fig. 2.3) molasse sediments of the Okwa Group which unconformably overlie the Mamuno Formation.

Provenance of the detritus for the Ghanzi Group metasediments remain a long-standing question. The Ghanzi Group (middle to upper) records a maximum depositional $^{207}Pb/^{206}Pb$ age

of 1060-1050 Ma and minimum depositional age of ~981 Ma (derived from sulfide Re-Os ages; Hall et al., 2018a, 2021). These metasediments also preserve minor zircon populations of Paleoproterozoic and Archean age (Schwartz et al., 1995; Kampunzu et al., 2000; Hall et al., 2018a).

2.2.3 Mineralization in the Kalahari Copperbelt

In Botswana the base of the D'Kar Formation is known to be intermittently mineralized with Cu sulfides over 220 Km along the Ghanzi ridge (Schwartz et al., 1995). The Cu-Ag deposits of the GCZ have been described as structurally-controlled, stratabound, and mineralogically zoned deposits by numerous researchers (e.g. Schwartz et al., 1996; Gorman, 2013; Shephard, 2014; Walsh et al., 2014; Lehmann et al., 2015; Hall et al., 2018b, 2021; Kelepile et al., 2017, 2020). In addition to the Cu-Ag deposits of the KCB (Kampunzu et al., 1998; Sillitoe et al., 2010), Piestrzynki et al. (2015) identified the potential of the Neoproterozoic Ghanzi Group of the GCZ for hosting precious metals (PGMs) mineralization. The orebodies in the GCZ are typically stratiform to stratabound and broadly structurally controlled, in many cases possessing kilometre-scale strike lengths (Schwartz et al., 1996; Hall et al., 2018b). Most of the metal deposits are hosted by the lowermost carbonate-siltstone package of the D'Kar Formation which unconformably overlies the hematite-bearing red sandstone of the Ngwako Pan Formation (Fig. 2.3).

Within the GCZ, Cu-Ag mineralization in the Khoemacau metallogenic district is present in a variety of styles, including: i) dissemination, ii) as aggregates or lenses along bedding/foliation planes, iii) comparatively coarser sulfides in quartz-carbonate veins, and iv) cleavage-controlled

mineralization. The better understood deposits are characterized by a vertical mineral zonation and an ore body thickness of 10 to 20 m (Hall et al., 2018b). There may be subtle differences in the stratigraphic position of the ores and associated sedimentary facies. Through exploration drilling, Hall et al. (2018b) recognized regional- to deposit-scale variations in sedimentary facies and stacking patterns for the lowermost D'Kar Formation which hosts the majority of the Cu-Ag mineralization. For example, stacked orebodies were discovered over the fold closure of a plunging anticline within the Ngwako Pan Formation at the Northeast Fold deposit of the Banana Zone (Hall, 2017).

Two likely source of metals in the deposits of the Khoemacau district and the KCB have been proposed: a) the red bed sandstone of the Ngwako Pan Formation, which forms the footwall of the mineralization in the Boseto area and contains an average of 41 ppm Cu (Schwartz et al., 1995), and b) basaltic rocks within the Kgwebe Formation and/or mafic to ultramafic units of the Umkondo Igneous Province that occurs to the south of the KCB (Hall et al., 2018a).

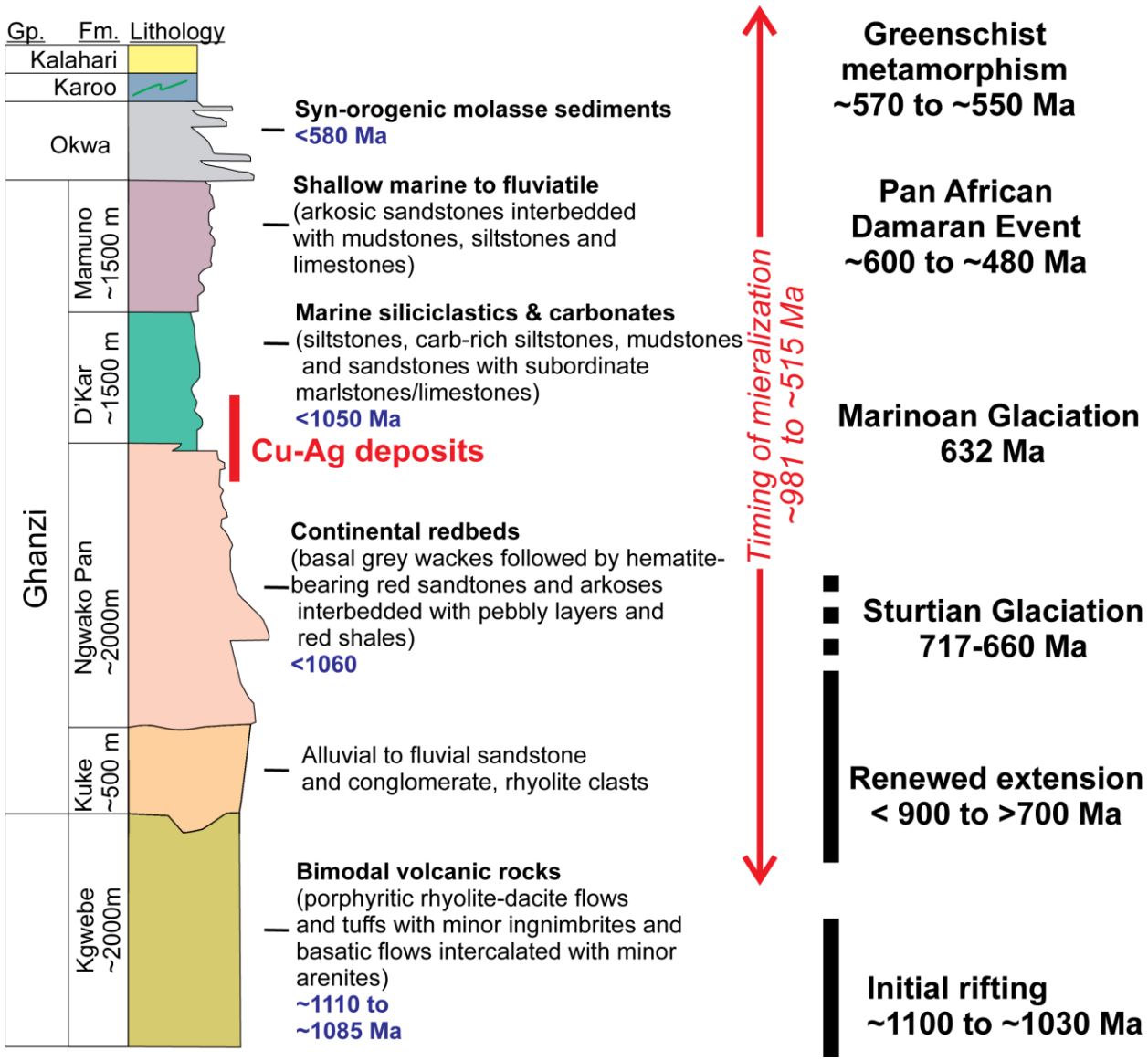

Figure 2.3 Generalized stratigraphy of the Ghanzi Ridge area and corresponding geochronology from literature depicting the tectonic evolution and mineralization events within the KCB in Botswana. Hall et al. (2021) provides recent mineralization age data (~981 to ~515 Ma) in the KCB. The rocks record complex history of extension prior to inversion and regional metamorphism. Major glaciation events (Hitzman et al., 2010) linked to salt diapirism are also shown for correlation with available geochronological data.

Akita University

Chapter 3

GEOLOGY AND MINERALIZATION OF THE ZONE 5 Cu-Ag DEPOSIT

3.1 Introduction

The Zone 5 deposit is located 35 km SE of the Boseto Cu Mine (Fig. 3.1) and contains a measured and indicated resource of 100 Mt at 2% Cu and 21 g/t of Ag. Zone 5 is the third Cu mine in the Kalahari Copperbelt after the Klein Aub Mine, Namibia (exploited until 1987; Ruxton, 1986; Borg and Maiden, 1989) and the Boseto Cu Mine, Botswana (2012-2015; Discover Metals Limited, 2012). The deposit was discovered in 2012 from a soil anomaly and it is found beneath ~40m of Kalahari Sands cover (Fig. 3.2, 3.3) on a limb of a regional scale anticline. Zn and Pb form anomalous halos around high Cu grade orebodies and have been identified as a practical exploration tool (Fig. 3.4).

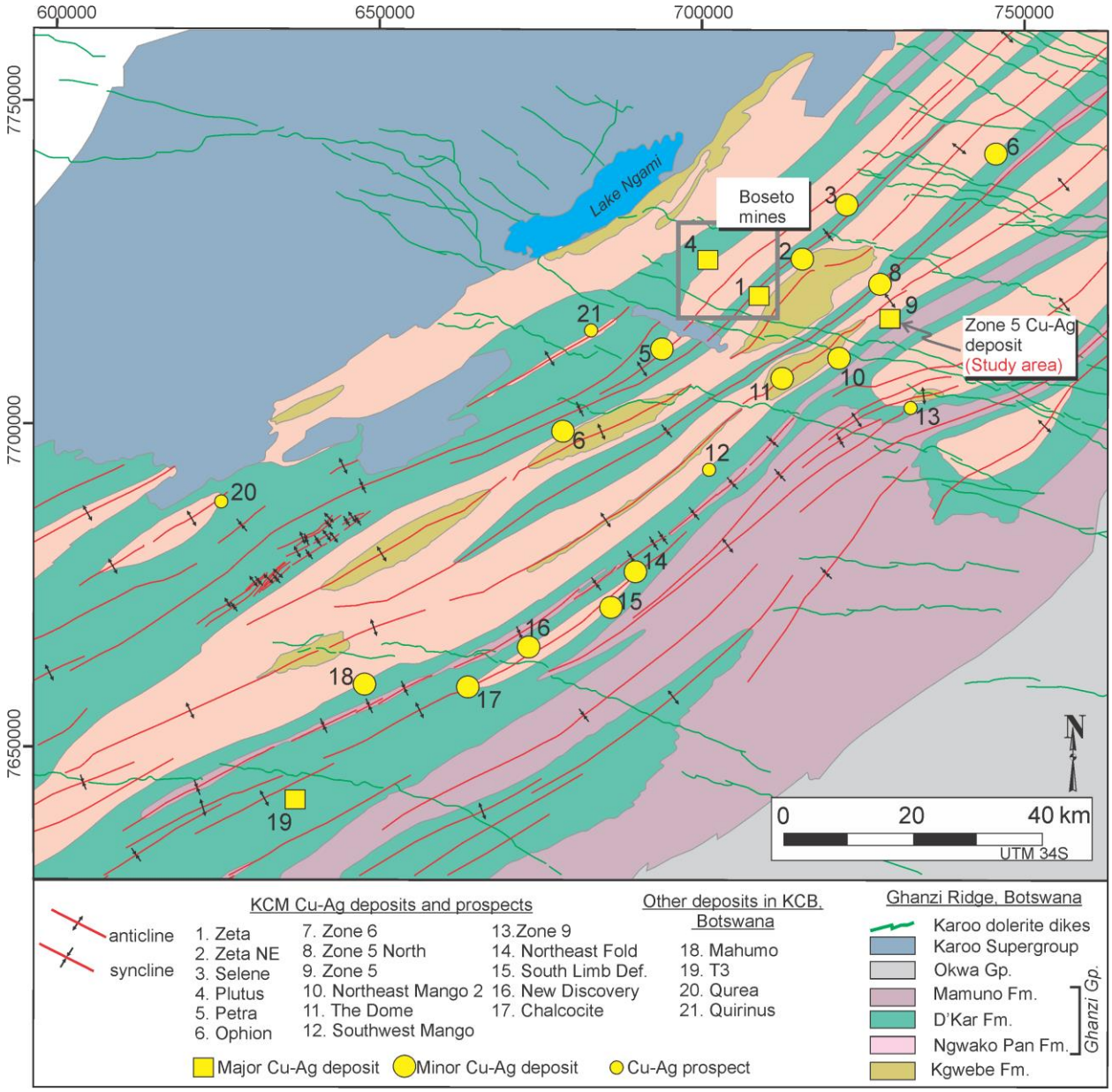

Figure 3.1 Generalized geologic map and Cu-Ag deposits of the Ghanzi Ridge, Kalahari Copperbelt in Botswana (modified from Lehmann et al., 2015; Hall et al., 2018b). Geology is inferred from known geology and geophysics. Folds typically plunge gently NE and SW, are usually upright and open to tight. They have wavelengths of 5 to 12 km and amplitudes of few km. SFZ=Southern Foreland Zone, GCZ= Ghanzi Chobe Zone.

3.2 Methods

During field trips in 2018 (2 weeks in August) and 2019 (February to April), a total of 16 representative drill cores were examined for lithology and mineralogy prior to sampling representative quarter-core samples. For the purpose of this study drill core examination and sampling was mostly focused on ore intervals (ore zone). The assay data provided by the company was used to guide sampling, particularly high-grade intervals. Samples collected are presented as original field notes in Appendix A. A portion of high-grade samples (samples potentially containing Ag) were subjected for micro-X-ray fluorescence (µXRF) analyses at the University of Texas at El Paso, for elemental mapping and quantitative analysis.

3.3 Host lithologies and associated structure

From bottom to top, the stratigraphic sequence studied at Zone 5 can be classified into six units: i) footwall hematite-bearing red-bed sandstone, ii) lower marl, iii) limestone, iv) alternating sequence of carbonate rocks and siltstone, v) carbonaceous siltstone, and vi) hanging-wall massive marker sandstone (Fig. 3.3, 3.4). The boundary between the red-bed sandstone at the footwall and the overlying carbonate units (lower marl and limestone) represents abrupt facies change that defines a transition from oxidizing to reducing conditions. The alternating sequence and carbonaceous siltstone units are chemically-reduced metasedimentary rocks that are composed of siltstone, carbonaceous siltstone, and mudstone. Ore grade mineralization is preferentially hosted by the chemically reduced metasedimentary sequence comprising siltstone, black mudstone, and subordinate carbonate rocks of the lower D'Kar Formation (Fig. 3.4).

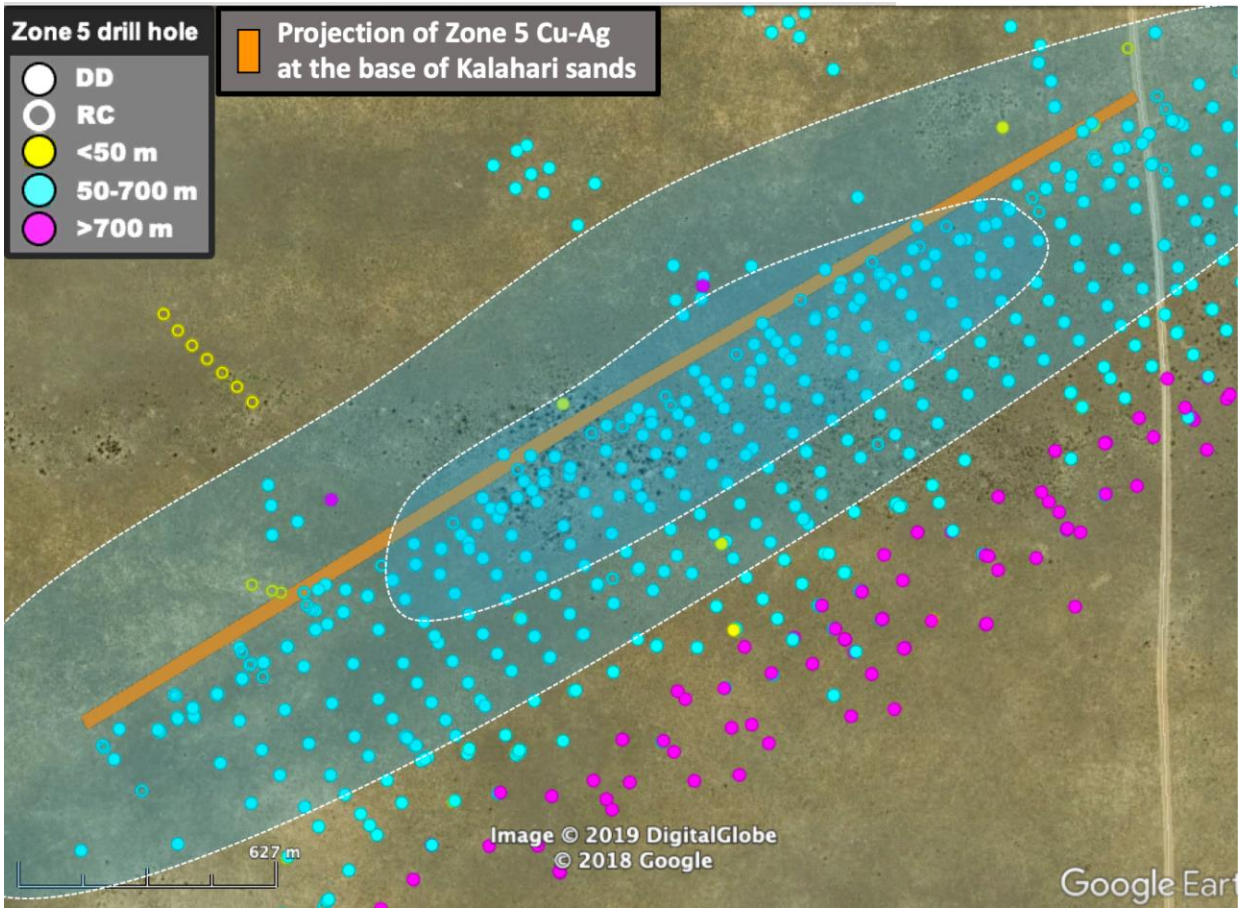

Figure 3.2 Google earth map showing the spread of drill holes at Zone 5. 16 drill holes (elaborated in Appendix A) were selected, some along the fences while some were selected randomly based on Cu and Ag grades. The google earth image show the large coverage by aeolian sands of the Kalahari Group, rendering the Zone 5 a blind deposit.

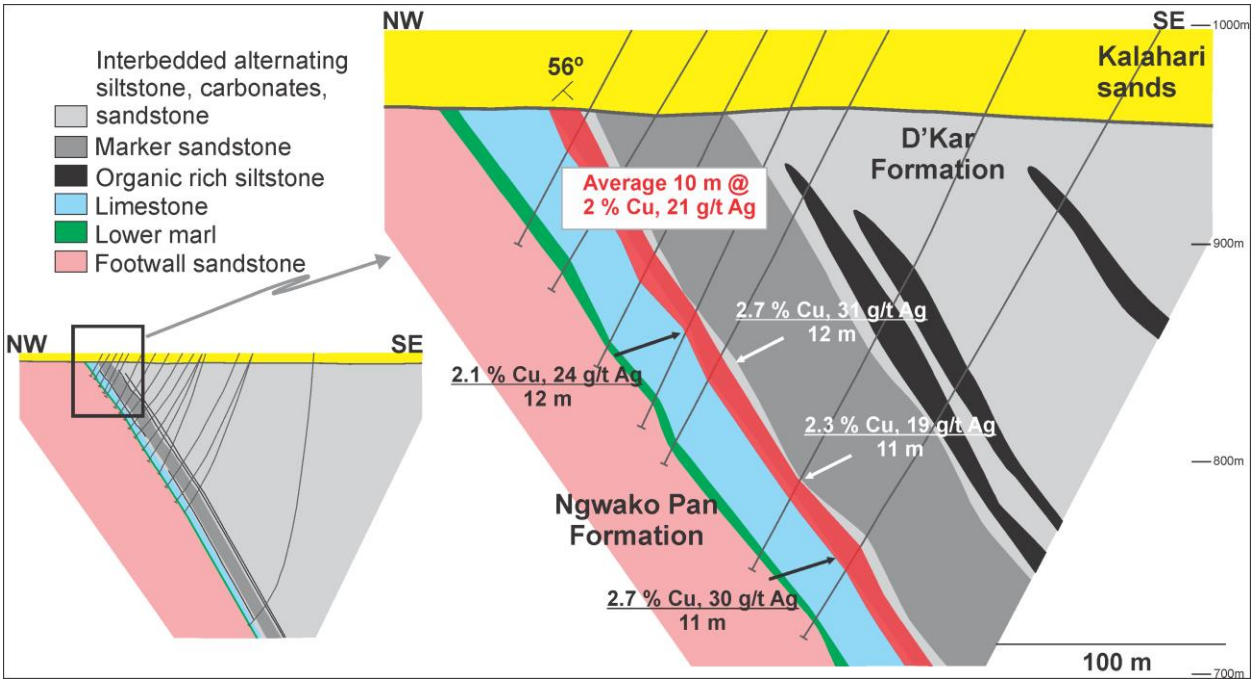

Figure 3.3 A schematic cross-section (representative) of the Zone 5 deposit. The orebody (mineralogically zoned) with an average thickness of 9-10 m, located between the red-beds and carbonate-siliciclastic package is generally dipping ~55° SE. and is sitting beneath ~40 m thick of the Kalahari Sands. Adapted from Knight et al. 2016.

3.4 Mineralization styles (ore textures)

In drill core, metallic mineralization is characterized by a redox-buffered sulfide zonation, which is defined by a change, with increasing stratigraphic height, from specular hematite to chalcocite to bornite to chalcopyrite to a broad halo of pyrite-galena-sphalerite. Locally, the majority of the sulphides, together with accompanying silver mineralization, are concentrated within quartz-carbonate veins and structural fabric, such as foliation, crenulation cleavage, and shear zones. The correlation of assay data with drill core examination indicates that high Cu

grades coincide with vein-hosted and cleavage-hosted ore (Fig. 3.3). Assay data establish a positive correlation between Cu and Ag (Fig. 3.3).

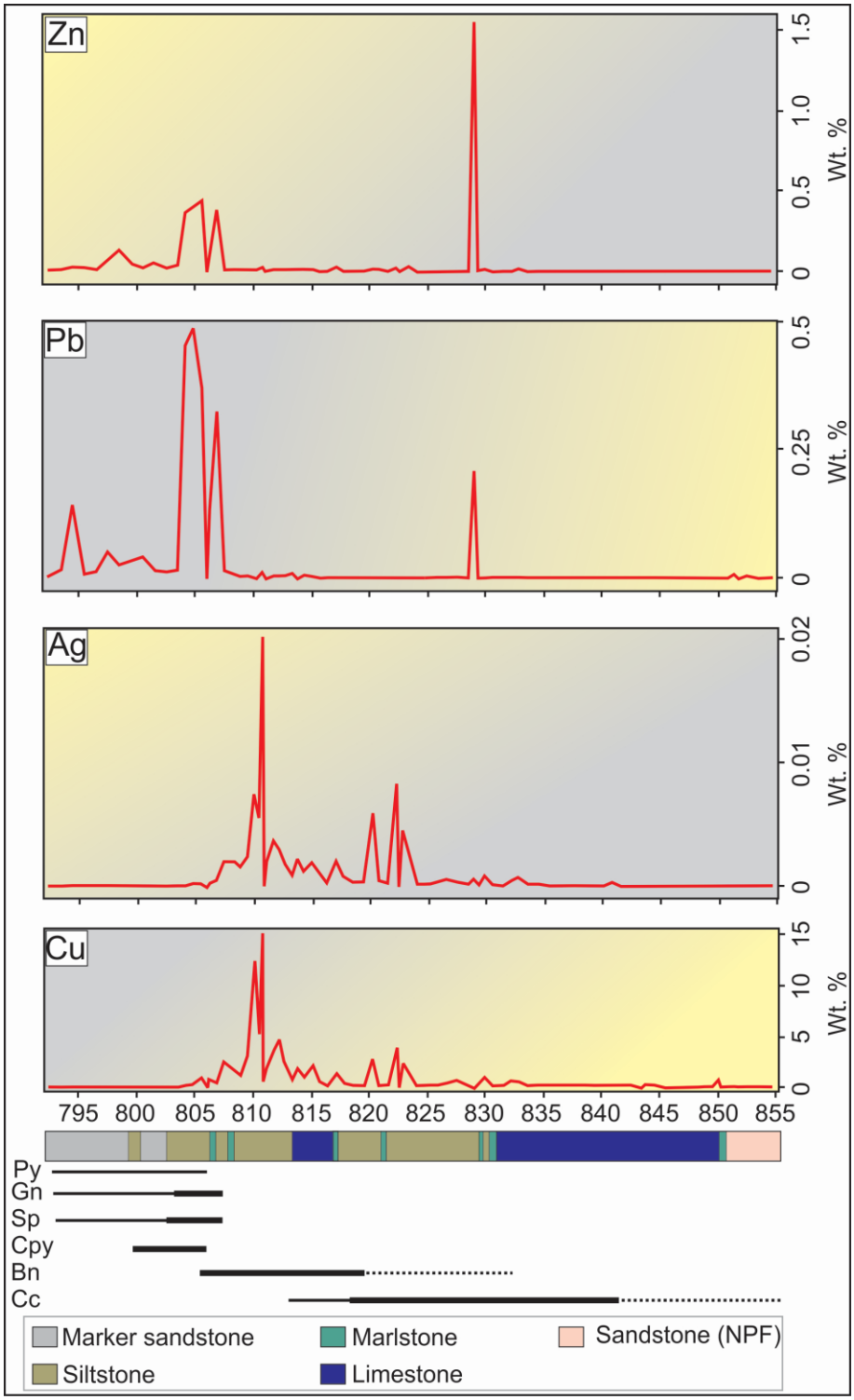

Figure 3.4 The typical stratigraphic column at the ore interval (ore zone) at the Zone 5 deposit, showing prominent host lithologies and corresponding assay data, as well as mineral abundances from the drill core section used in this study. Abbreviations: Gn=galena, Sp=sphalerite, Cpy=chalcopyrite, Bn=bornite, Cc=chalcocite

3.4.1 Bedding- and foliation-parallel mineralization

Drill core examination shows that bedding-parallel mineralization occurs as aggregates, blebs and lenses of pyrite, galena, sphalerite, arsenopyrite, chalcopyrite, bornite, and chalcocite deposited along bedding or foliation planes (Fig. 3.5). This style of mineralization may or may not be associated with quartz-calcite veining or cleavage formation. In the lower marl and in the alternating sequence, bornite and chalcocite are the predominant disseminated ore minerals parallel to bedding. Chalcopyrite and pyrite are more noticeable within organic-rich siltstone and the hanging wall marker sandstone. Ubiquitous layer-parallel ore is commonly boudinaged, suggestive of a strong low-angle ductile shearing.

3.4.2 Mineralization in metamorphic cleavage

Cleavage fabric is preserved in two main geometries: penetrative cleavage, sub-parallel to bedding, and less penetrative crenulation cleavage at an angle to bedding (Fig. 3.6). Commonly, the lenticles of Cu ore observed along crenulation cleavage are silty/sandy layers of the host rock, indicating that mineralization is effectively controlled by porosity and permeability of the host lithology (Fig. 3.6A). Drill core examination reveals that cleavage fabric

Figure 3.5 A drill-core photograph showing typical bedding-parallel mineralization. Chalcopyrite is focused along bedding in an organic-rich siltstone, also spatially associated with bedding-parallel calcite-dominant veinlets.

predominantly develops in siltstone, lower marl and limestone, and far less common in the footwall sandstone. Axial foliation planes are oblique to lithological layering and commonly closely spaced (Fig. 3.6). This style of mineralization is characterized by occurrences of sphalerite, chalcopyrite, bornite, and chalcocite. A chalcocite-bornite association is most prominent in foliation-parallel mineralization within the lower marl and the limestone and siltstone of the alternating sequence, suggesting that ductile shearing was more pronounced within the lower-most horizon of the D'Kar Formation. The mineralization in crenulation cleavage indicates contemporaneity with fold-related shearing and that the mineralizing fluid may have been derived from the veins parallel to cleavage fabric (Fig. 3.6).

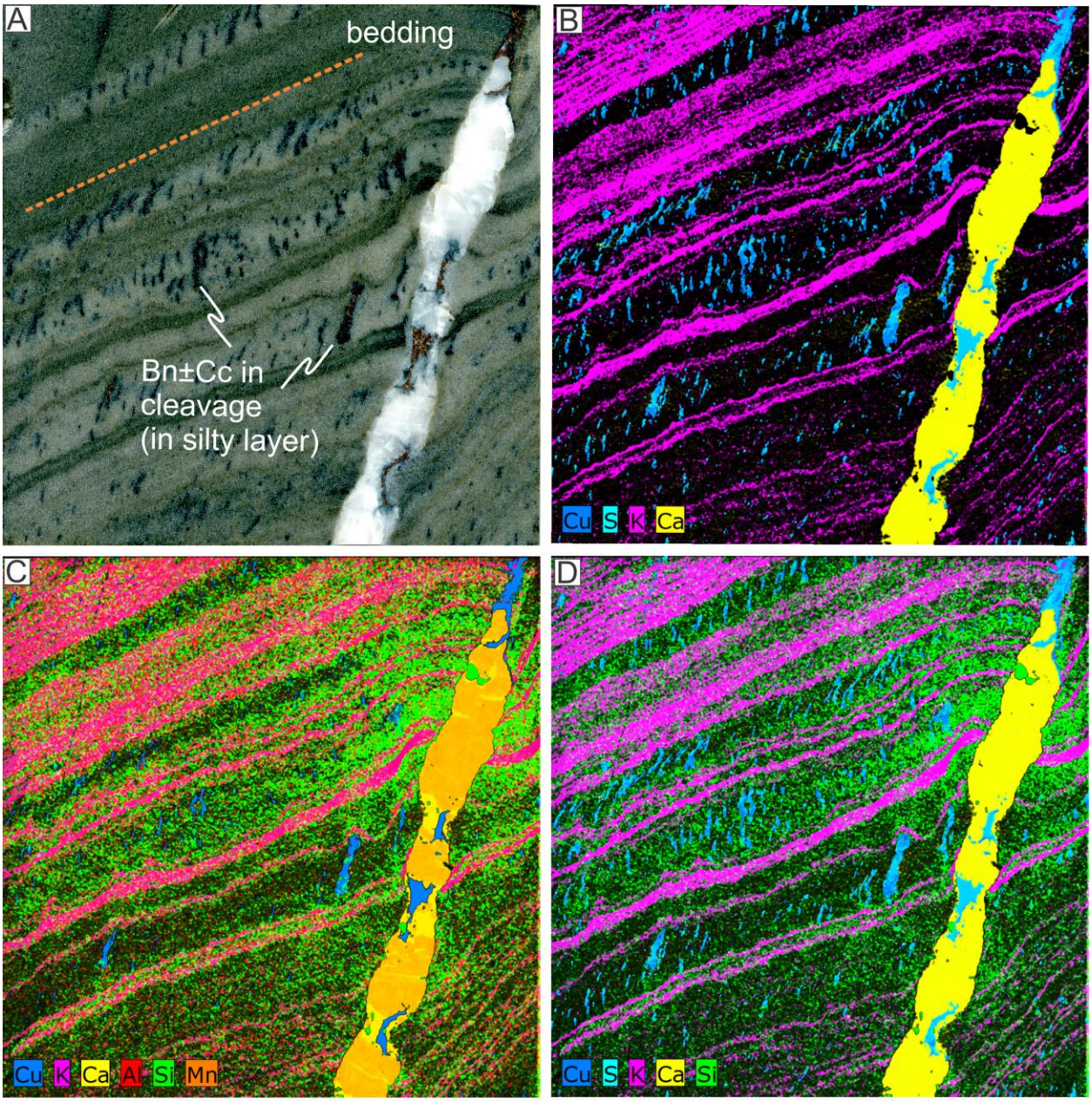

Figure 3.6 Representative drill-core photograph showing metamorphic cleavage-controlled mineralization. **A)** Drill photograph showing the bornite-chalcocite ore in silty (porous) layers and along the vein. **B)** to **D)** Micro-X-ray fluorescence (µXRF) elemental maps of (A) showing the spatial distribution of different important elements in the host rock and the vein, that include

Cu, Fe, Ca, Al Si, Mn, S, and K. (µXRF analyses and images by Hannah Buamono, the University of Texas at El Paso).

3.4.3 Vein-type mineralization

Quartz-calcite veins are the main host of high-grade Cu mineralization. Although quartz-calcite veins occur throughout the stratigraphic succession, mineralized centimetre- to meter-scale veins occur preferentially in finely laminated and deformed metasedimentary rocks (Figs. 3.7, 3.8). Vein-hosted ore minerals are pyrite, galena, arsenopyrite, sphalerite, chalcopyrite, bornite and chalcocite, with quartz and calcite as gangue. Quartz-calcite-chalcopyrite veins are less abundant compared to veins associated with bornite and chalcocite. Mineralized veins are predominantly parallel to the bedding and foliation planes and display evidence of ductile to brittle deformational overprinting, ranging from non-deformed to highly deformed (Fig. 3.7A, D). Layer-parallel sulfide-bearing veins are occasionally laminated (Fig. 3.7B), likely a consequence of post-depositional deformation. Quartz-calcite-sulfide veins also act as feeder zones to contiguous bedding-parallel mineralization (Fig. 3.7E). Another potential generation of veins is subparallel to mineralization emplaced along crenulation cleavage (Fig. 3.7C).

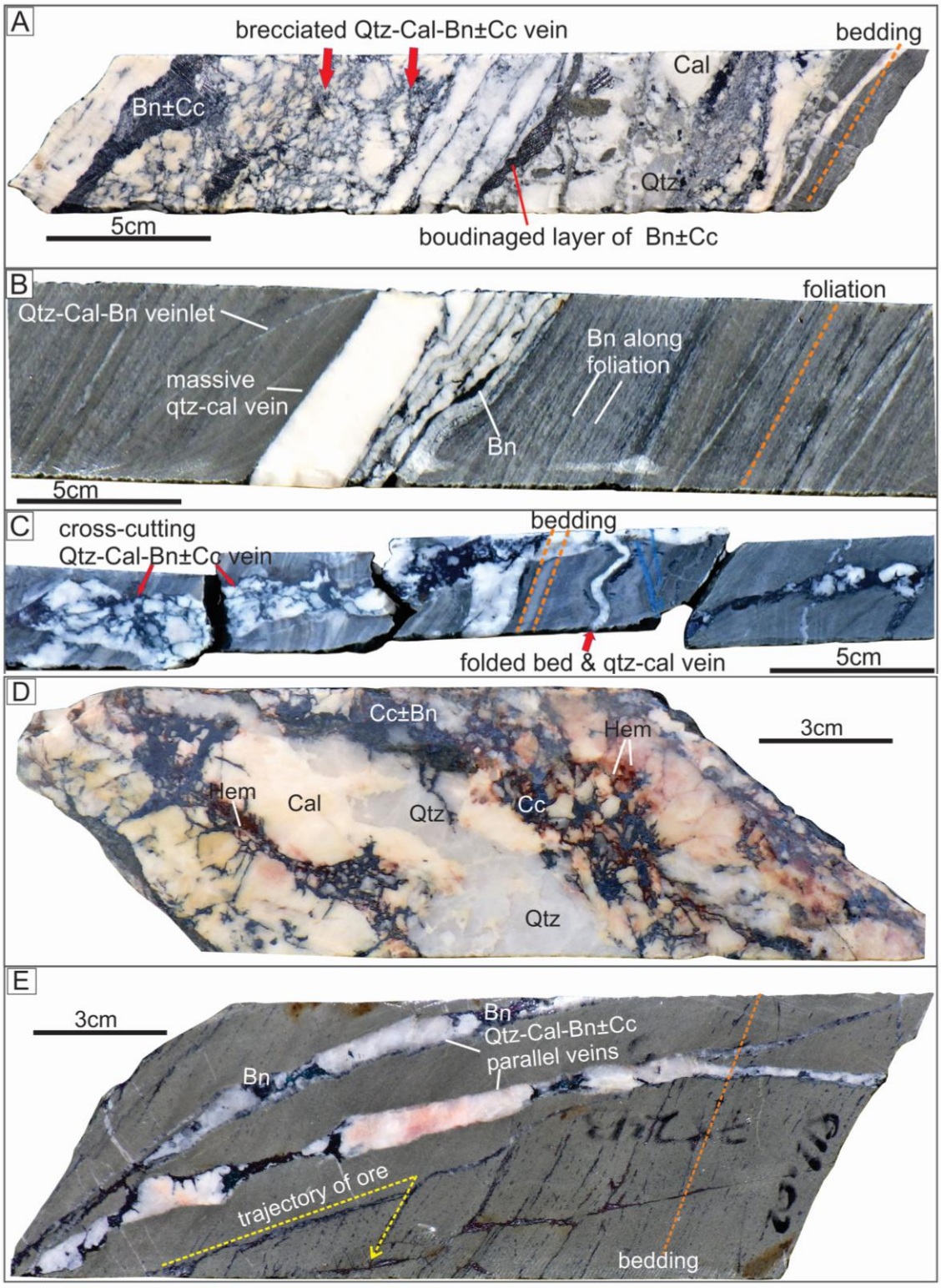

Figure 3.7 Representative photographs of drill-core for vein-type Cu-Ag mineralization, showing examples of bedding-parallel and cross-cutting vein-type ores. A) Hydrothermal breccia

indicating that ore was potentially introduced through hydrofracturing. Some sulfide-bearing veins are boudinaged along bedding indicating bedding-parallel shearing. B) Bornite ore in a laminated quartz-calcite vein hosted by a strongly-foliated calcareous siltstone. C) High angle, cross-cutting quartz-calcite-bornite ± chalcocite vein. The vein impregnates the ore along the bedding and later folded together with soft rheology. D) Quartz-calcite-chalcocite-hematite vein with no signs of shearing. Hematite occurs around chalcocite corroding its grain margins. E) Cross-cutting mineralized quartz-calcite parallel veins associated with ore along the bedding and foliation planes indicating an association between vein-hosted and disseminated ore.

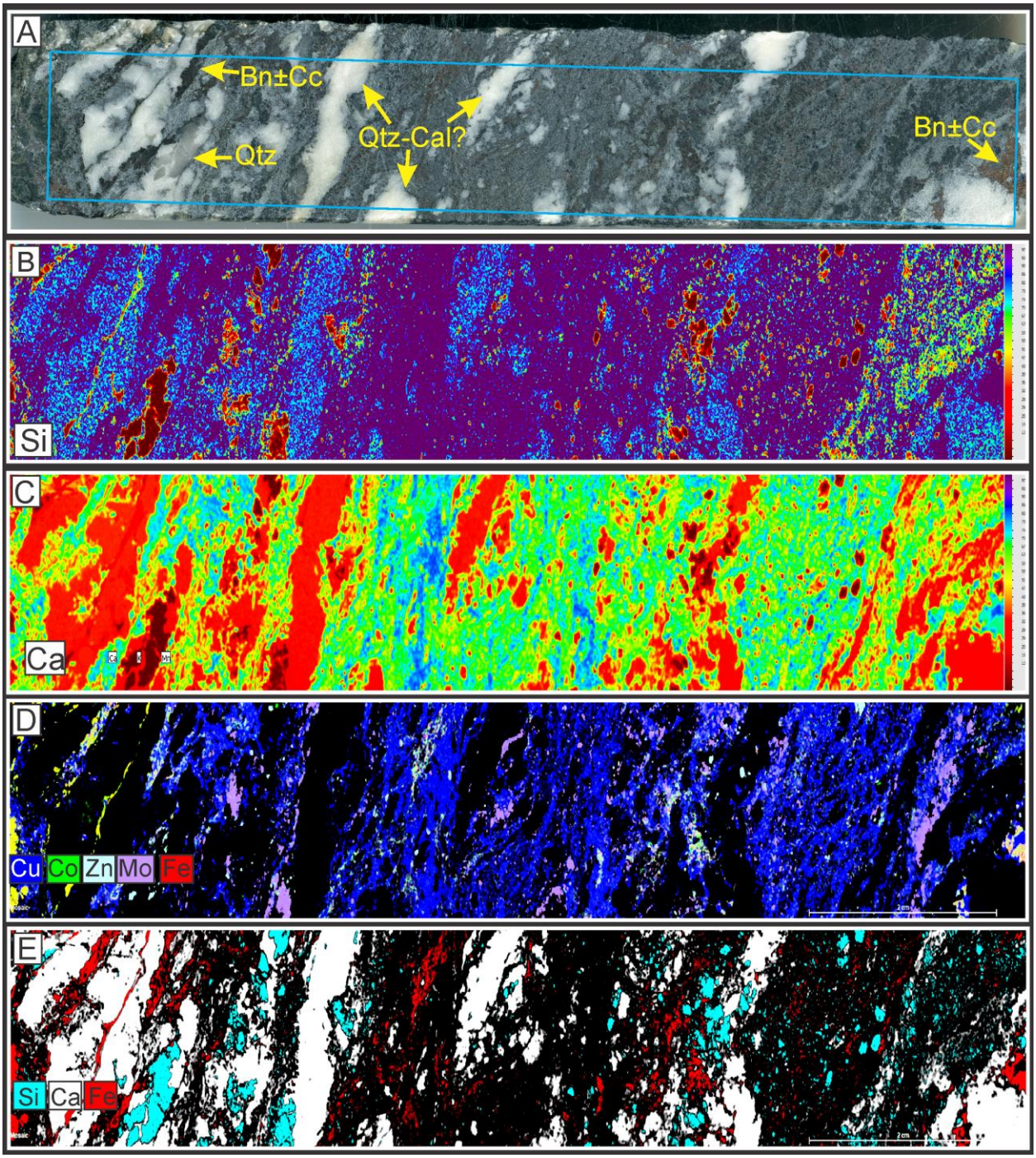

Figure 3.8 A) Drill core sample showing high-grade boudinaged and deformed quartz-calcite-sulfide vein. A section scanned with micro-X-ray fluorescence (µXRF) is shown by a blue rectangle. **B)** µXRF semi-quantitative single element (Si) intensity map showing the relative abundance of quartz in the sample. **C)** µXRF semi-quantitative single element (Ca) showing the relative abundance of calcite in the sample. **D)** µXRF image showing five-element (Cu, Co, Zn,

Mo, and Fe) map. Copper and Mo are the two standout elements and also close together indicating that the Cu-(Fe)-sulfide may contain some quantities of Mo. **E)** µXRF image showing a three-element map that includes Si, Ca, and Fe. Calcite is the dominant gangue mineral in the boudinaged veins.

Akita University

Chapter 4

PETROGRAPHIC AND MINERAL CHEMICAL CHARACTERISTICS

4.1 Methods

The paragenetic relationships of sulfides and other ore minerals were evaluated under polarizing microscope using both transmitted and reflected light as well as JEOL JSM-6610LV scanning electron microscope with an Oxford Instruments INCA X-act energy-dispersive detector (SEM-EDS) at Akita University. The concentrations of Cu, Fe, S, As, Ag, Co, Ni, Zn, Pb, Sb, and Bi were measured using a JEOL JXA-8230 (20 kV, acc. voltage, 20nA beam current, 5 µm spot size) X-ray electron microprobe at Akita University. The standard materials (from Astimex Standards Ltd.) used were natural minerals and pure metals (pyrite, Co-metal, pentlandite, chalcopyrite, arsenopyrite, stibnite, Ag-metal, galena, and guanajuatite). The detection limit for Cu, Fe, S, As, Ag, Co, Ni, Zn, Pb, Sb, and Bi were 152 ppm, 111 ppm, 47 ppm, 346 ppm, 76 ppm, 87 ppm, 101 ppm, 195 ppm, 189 ppm, 157 ppm, 230 ppm, respectively.

4.2 Petrography and paragenesis

Based on detailed petrographic study, two distinct mineralizing events were identified in Zone 5. The overall paragenesis of the ore-stage sulfides at Zone 5 described in this study (Fig. 4.1) is broadly consistent with descriptions made by previous researchers (e.g. Schwartz et al., 1996; Hall, 2013, 2017, 2021; Gorman, 2013; Shephard, 2014; Walsh et al., 2014; Kelepile et al.,

2020). In the following sections, individual stages are described in terms of relative timing of sulfide precipitation.

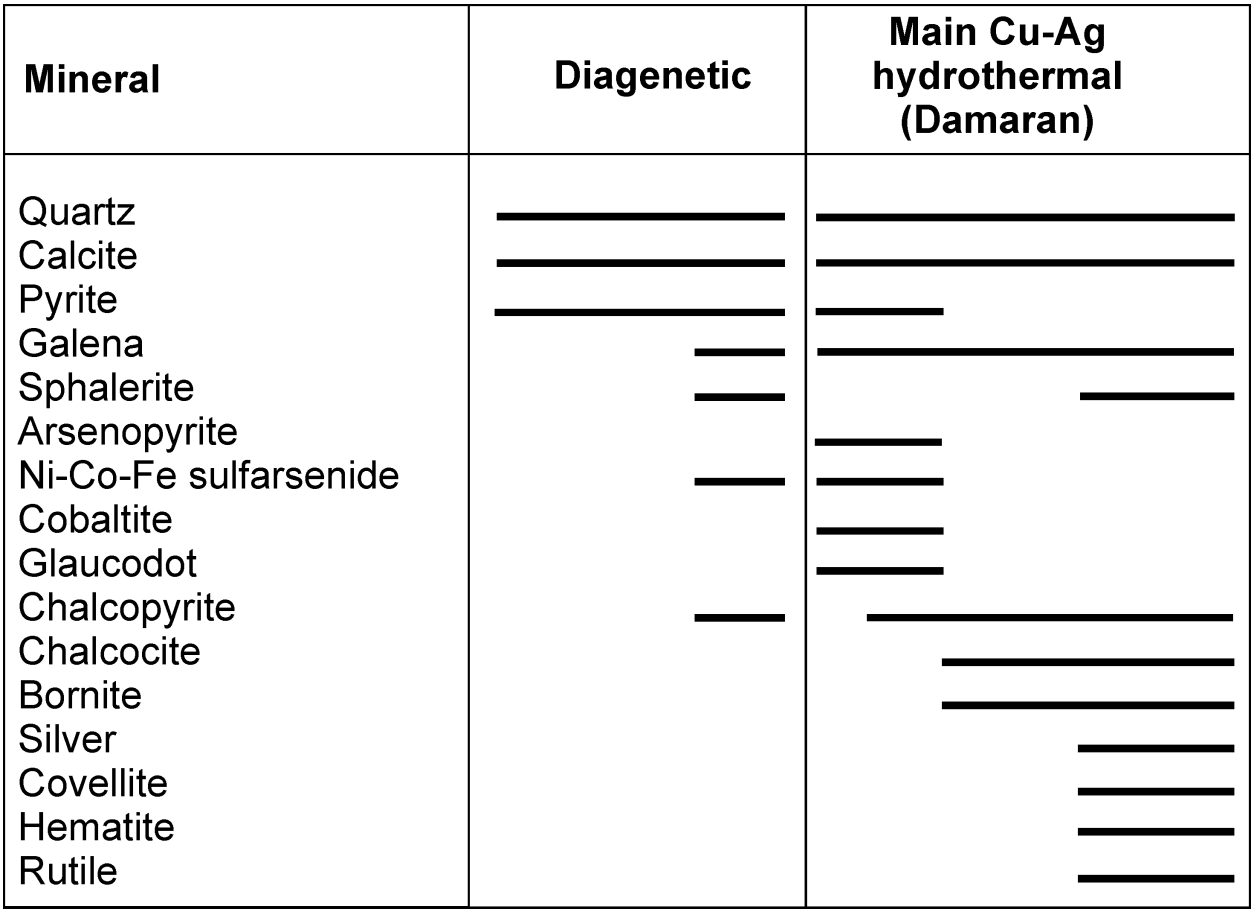

Figure 4.1 The paragenetic sequence observed at Zone 5 Cu-Ag deposit in selected samples from the ore interval (within 70 meters above the footwal).

4.2.1 Diagenetic Cu-Pb-Zn mineralization

Very fine-grained pyrite (<5µm) is observed concentrated along laminations (Fig. 4.2A), while medium-grained (>5 µm) subhedral to euhedral pyrite overgrows lithologic layering. Very fine-grained pyrite commonly intergrown with host rock mineral assemblages and spread along

laminations or bedding planes is reminiscent of diagenetic pyrite. The >5 µm pyrite commonly occurs either as clusters of recrystallized framboidal pyrite or non-framboidal subhedral to euhedral crystals (Fig. 4.2B to F). Recrystallized framboidal pyrite shows a distinctive morphological evolution (Py-1 to Py-2; Fig. 4.2C) and is often restricted to calcite-dominant portions in the host rock. Py-1 and Py-2 also preserve lenticular to ovoid nodular shape with their long axes parallel to bedding (Fig. 4.2D). Skeletal subhedral to euhedral pyrite may also form in former calcite nodules (Fig. 4.2G, H).

Petrographic examination revealed that pyrite is intergrown with sphalerite, galena, (Co, Ni, Fe) sulfarsenide, and minor chalcopyrite (Figs. 4.2B, C, E, F, I). SEM-EDS observations also revealed that subhedral pyrite and galena are associated with REE-aluminosilicate and apatite. Sphalerite and galena are intergrown with authigenic quartz (mostly recrystallized) and calcite (Figs. 4.3A), indicating post-precipitation deformational and metamorphic overprinting. Disseminated coarse-grained anhedral sphalerite crystals are distributed within coarser grained laminations, preferentially parallel to bedding. Coarse-grained anhedral sphalerite, often flanked by calcite and quartz, hosts inclusions of cubic euhedral pyrite and is partially rimmed by late-precipitating anhedral galena (Fig. 4.3B). In this mineralization style, pyrite precipitation was followed by calcite and sphalerite which were then enclosed by authigenic quartz. Coarse-grained sphalerite, which is often intergrown with galena, usually contains bleb-like inclusions of chalcopyrite (Fig. 4.4C), characteristic of chalcopyrite disease.

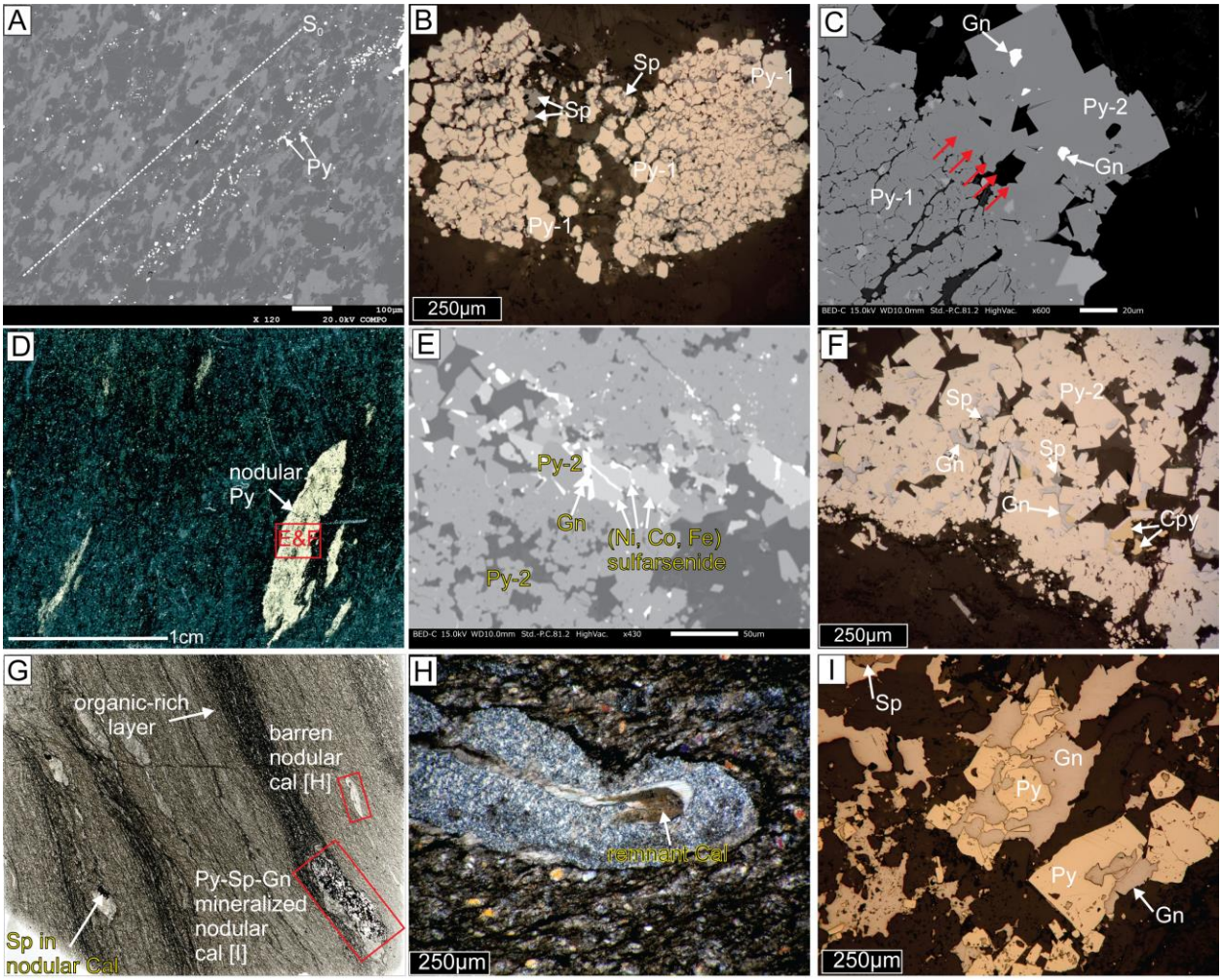

Figure 4.2 Photomicrographs of diagenetic pyrite and associated sulfide minerals. A) Backscattered electron (BSE) image of fine-grained spheroidal-subhedral pyrite concentrated along laminations. B) Py-1 framboidal pyrite overgrown (coated) by sphalerite. C) Morphological transition (shown by red arrows) defined by subhedral Py-1 framboidal pyrite recrystallized to cubic, euhedral Py-2 pyrite. D) A hand specimen photograph of nodular pyrite (presumably diagenetic) showing areas of E and F. E) BSE images showing the intergrowth of recrystallized framboidal pyrite, and Ni-Co-Fe sulfarsenide. F) Reflected light image showing overgrowth of cubic euhedral pyrite by sphalerite, galena, and chalcopyrite. G) Thin section photograph showing authigenic calcite nodules, mostly restricted to organic-rich layers. Some

nodules are barren while some are mineralized primarily with pyrite, galena and sphalerite. Areas for H and I are shown in red rectangles. H) Polarized light image showing calcite remnant in a heavily altered calcite nodule. I) intergrowth of skeletal subhedral to euhedral pyrite with galena.

4.2.2 Main Cu-Ag hydrothermal mineralization

High-grade Cu-Ag mineralization occurs in multi-stage quartz-calcite veins, along bedding, foliation and crenulation cleavage planes, and within shear zones (Figs. 3, 4). Petrographic observations indicate that this stage is characterized by precipitation of bornite, chalcocite chalcopyrite, pyrite, arsenopyrite, sphalerite, galena, covellite, cobaltite, glaucodot, (Ni, Fe, Co) sulfarsenide, silver, hematite, and rutile. Secondary minerals formed by supergene oxidation, which are described in other parts of the KCB (e.g. Piestrýnski et al., 2015), are rare at Zone 5. Fine-grained cubic euhedral pyrite, (Ni, Co, Fe) sulfarsenide, cobaltite (Fig. 4.3C), glaucodot, and arsenopyrite formed during the earliest stages of hydrothermal mineralization, giving way to subsequent precipitation of Cu sulfides and accompanying Ag.

Arsenopyrite occurs as prismatic crystals elongated along the direction of foliation/bedding, often rimmed by recrystallized fibrous quartz which encloses both calcite and chalcocite (Fig. 4.3D, E), suggesting that arsenopyrite and calcite precipitated first and were later followed by chalcocite. Individual arsenopyrite crystals display fibrous quartz-calcite or quartz-only pressure shadows that grew perpendicular to crystal faces (Fig. 4.3D, E), indicating pre-metamorphism precipitation. Undulose extinction and weakly rotated pressure shadows

indicate deformational overprinting on arsenopyrite crystals. Large prismatic crystals of arsenopyrite oriented subparallel to lithological layering decompose into bornite and chalcocite (Fig. 4.3F). Pyrite, and sulfarsenide mainly occur as inclusions or are often encased by bornite, indicating earlier formation. Minor occurrences of euhedral glaucodot crystals were observed, often as inclusions within bornite.

In increasing order of abundance, chalcopyrite, chalcocite, and bornite are the main copper sulfides which form in quartz-calcite domains. Sulfide bearing quartz-calcite veins are characterized by coarse-grained anhedral to irregular-shaped Cu sulfides, often exploiting high porous zones (freely growing in between and around grains). Chalcopyrite, bornite, and chalcocite are commonly intergrown (Fig. 4.4A), with the bornite-chalcocite coexistence (Fig. 4.4B) being the most common. The grain boundaries between chalcocite and bornite vary between gently curved-to highly irregular, and bornite occurs as both islands and envelope in and around chalcocite grain margins (Fig. 4.4B).

Petrographic analysis also indicates that originally-disseminated foliation-parallel bornite-chalcocite intergrowths are stretched and transposed (remobilized) into axial cleavage subsequent to ductile shearing. Chalcopyrite-only and chalcopyrite-bornite-chalcocite intergrowths are also subjected to similar deformational overprinting. Although assay data indicate a positive correlation between Cu and Ag (averaging 22 g/t Ag for the deposit), Ag minerals are not common at Zone 5. However, micro-X-ray fluorescence and SEM-EDS analysis revealed the occurrence of rare native silver around chalcocite grain boundaries (Fig. 4.4D), suggesting later precipitation.

Hematite appears in, but not exclusively, chalcocite-rich portions, corroding chalcocite along the rims. Hematite also forms a veinlet network within coarse-grained chalcocite micro cracks, suggestive of its alteration nature (Fig. 4.4E). Covellite is very minor, and its occurrence postdates that of other Cu sulfides.

The fine-grained nature of the host rocks together with deformational and metamorphic overprinting, makes it difficult to identify hydrothermal alteration minerals. Nonetheless, muscovite, chlorite, sericite, and rutile have been identified as hydrothermal alteration minerals associated with Cu mineralization. Authigenic rutile is a common accessory hydrothermal mineral that occurs as acicular randomly oriented crystals within chalcocite and bornite grains (Fig. 4.4F). SEM-EDS analysis also reveals the subtle overprinting/alteration on calcite and quartz by iron-rich (Fe-Mg±Ca) aluminosilicates.

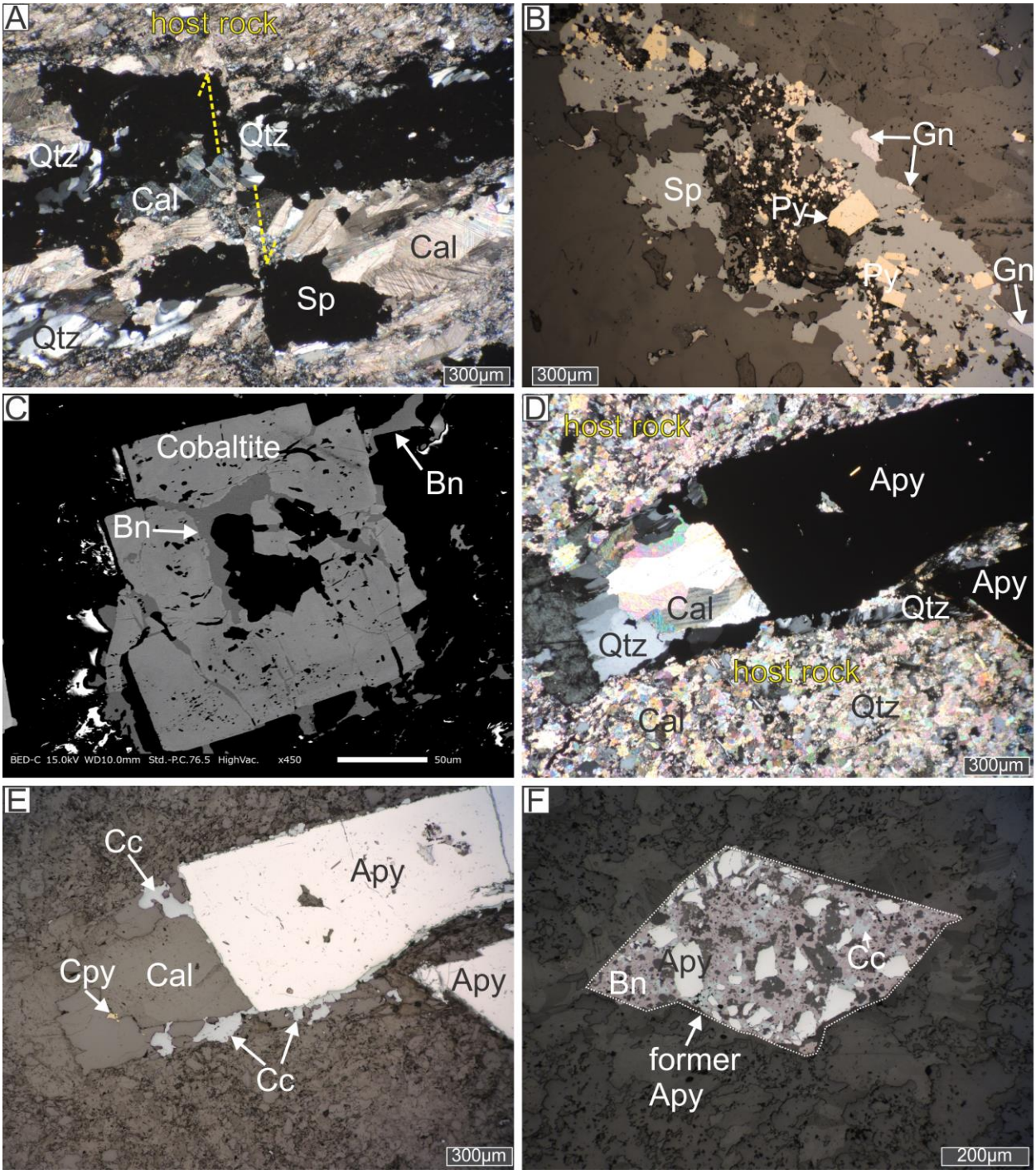

Figure 4.3 Microphotographs displaying textural relations between pyrite, sphalerite, galena, cobaltite as well as arsenopyrite textural, morphology, and mineralogical relations with Cu-(Fe) sulfides. A) Polarized light image displaying micro-faulted sphalerite intergrown with quartz and

calcite, indicating postcrytallization deformation. Fibrous quartz partially encloses both sphalerite and calcite, indicating its paragenetically late. B) Reflected light image of sphalerite hosting inclusions of cubic euhedral pyrite. Sphalerite is partially rimmed galena, suggestive of late precipitation. C) BSE image displaying cobaltite being replaced by bornite. D) and E) Polarized and reflected microphotographs of coarse-grained prismatic arsenopyrite consisting of rims of recrystallized quartz infilled by calcite and chalcocite. Chalcocite preferentially precipitates along the rims of arsenopyrite. F) Reflected light image showing replacement of brecciated arsenopyrite by bornite-chalcocite intergrowth.

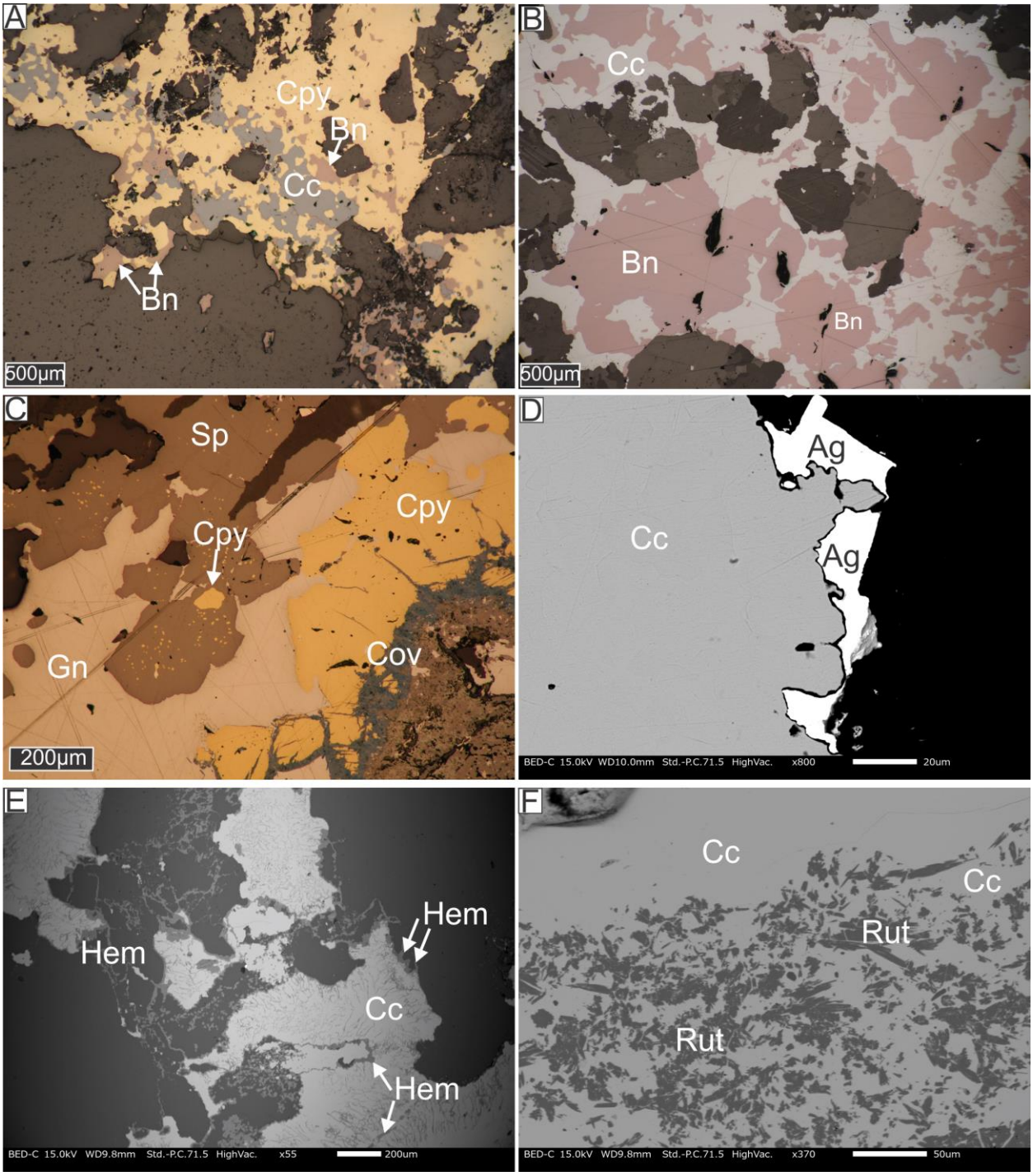

Figure 4.4 Microphotographs of vein-type and cleavage-controlled ores. This stage is enriched with Cu and Ag. **A)** A reflected light image showing intergrowth texture between coarse-grained chalcopyrite, bornite, and chalcocite. **B)** Reflected light image of typical coarse-grained bornite-

chalcocite intergrowth texture. Bornite mainly occurs as islands in chalcocite. **C)** Reflected light image showing chalcopyrite-sphalerite-galena-covellite intergrowth. Covellite is the latest mineral to precipitate, largely replacing chalcopyrite. **D)** BSE image displaying native silver occurring around chalcocite, suggestive of late precipitation. **E)** BSE image showing coarse-grained chalcocite being enclosed by hematite alteration. Hematite also form veinlet network within chalcocite micro-cracks. **F)** BSE image displaying acicular rutile grains, grown with chalcocite.

4.3 Sulfide trace element compositions

The trace element data of sulfide minerals collected using electron microprobe (EPMA) in this study is presented in Appendix B and Fig. 4.5. Pyrite, galena, (Ni, Co, Fe) sulfarsenide, sphalerite, arsenopyrite, chalcopyrite, bornite, chalcocite, and covellite were analyzed for Fe, Cu, Zn, As, Co, Ni, S, Pb, Bi, Ag, and Sb concentrations.

Recrystallized framboidal pyrite is both Cu (up to 0.25 wt.%) and Ag (up to 106 ppm) poor (Fig. 4.5). However, EPMA analyses also revealed that Py-1 is enriched in Fe, Co, Sb compared to Py-2, which records relatively high Ni, As, and Ag concentrations. (Ni, Co, Fe) sulfarsenide which occurs as inclusions in hydrothermal Cu sulfides (particularly in bornite) yielded very low Bi, Zn, Sb, and Ag (< 76 ppm) concentrations. Sulfarsenide hosts significant Cu between 2.8 and 3.1 wt.% while Pb ranges between 180 ppm and 260 ppm (Fig. 4.5).

Elemental analysis indicated that galena from both stages of mineralization is generally poor in Ag. However, galena hosts comparably elevated concentrations of Bi (0.1 to 0.15 wt.%)

and As (24.7 to 26.7 wt.%; Fig. 9) and up to 0.4 wt.% Cu. Sphalerite hosts measurable quantities of Cu (up to 2.24 wt.%), Fe (1.08 to 5.79 wt.), Bi (< 230 ppm), and Sb (< 157 ppm). In contrast, sphalerite has very low concentrations of Ni, Co, As, Pb, and Ag (except for one sample with 259 ppm Ag) (Fig. 4.5). The average Fe concentration for sphalerite is 3 wt.%.

Arsenopyrite hosts highly variable Cu concentrations (up to 5.2 wt.%) with a mean of 0.52 wt.%. Arsenopyrite also yielded measurable quantities of Bi (up to 290 ppm), Ni (up to 1.8 wt.%), Ag (up to 177 ppm), Co (0.03 to 2.5 wt.%), and Sb (< 157 ppm) (Fig. 4.5).

The copper sulfides host variable concentrations of Bi, Zn, As, Co, Pb, Ni, Ag, and Sb. The EPMA data show that chalcopyrite is generally Ag-poor, with an average Ag concentration of 83.8 ppm . Chalcopyrite also hosts comparatively higher Ni (highly variable) and Co concentrations (Fig. 4.5). Significant quantities of Ag, Bi, Co, Zn, and Sb were measured in bornite with an average concentration of 0.22 wt.% Ag, 50 to 270 ppm Co, and 30 to 690 ppm Zn. Bornite also yielded an average of 19.8 ppm Sb and comparatively high Bi concentrations (up to 1020 ppm; Fig. 4.5).

The concentration of Ag in chalcocite is highly variable (0.02 to 0.49 wt.%), with a relatively lower mean (0.18 wt.%) than bornite. EPMA data also indicate that chalcocite has measurable concentrations of Co (up to 240 ppm), Sb (up to 210 ppm), Bi (up to 520 ppm), Zn (73 to 830 ppm), Fe (up to1.8 wt.%), and As (up to 1.4 wt.%), with negligible Ni and Pb contents.

Compositional data reveal that covellite, which postdates other Cu sulfides, is also a preferential host for Ag, with an average Ag concentration of 0.1 wt.%. Covellite contains relatively higher concentrations of Zn, Pb, and As, with values averaging 0.1 wt.%, 0.5 wt.% and

0.4 wt.%, respectively. Covellite also yields appreciable Fe contents, averaging 0.6 wt.% and comparatively lower concentration of Co, Bi, and Sb. Covellite that replaces chalcopyrite, galena, and sphalerite contains anomalously high concentrations of Fe (23.4 wt.%), Zn (31.8 wt.%), As (24 wt.%), and Pb (36 wt.%).

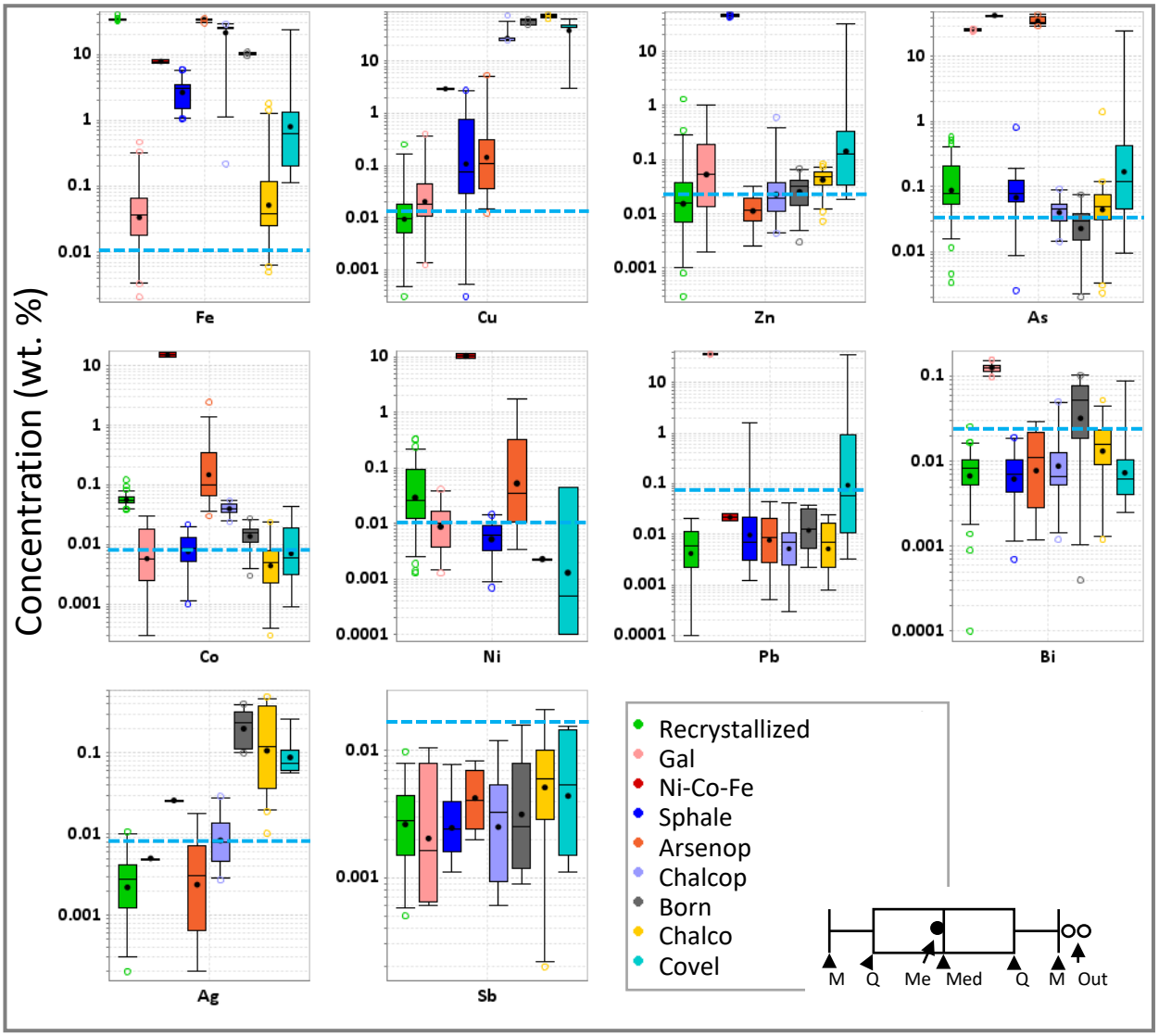

Note: The blue dotted lines represent the detection

Figure 4.5 Box and whisker plots displaying the concentration of Cu, S, Fe, Zn, Pb, As, Ag, Co, Ni, Bi and Sb in recrystallized framboidal pyrite, galena, Ni-Co-Fe sulfarsenide, sphalerite arsenopyrite, chalcopyrite, bornite, chalcocite, and covellite.

Akita University

Chapter 5

FLUID INCLUSIONS

5.1 Introduction

A fluid event is defined as a physical or chemical process such as the healing of a microfracture or the formation of a growth zone in a crystal that occurs in the presence of a fluid phase and results in trapping of fluid inclusions to form a fluid inclusion assemblage (FIA) (Fall and Bodnar, 2018).

Fluid inclusions are classified as either primary, secondary, or pseudosecondary. They may contain liquid, vapor, and/or solid minerals. Primary fluid inclusions are those found along the growth zones of the crystal growth (Roedder, 1979). The most accurate primary fluid inclusion type is a fluid inclusion assemblage (FIA) which is defined as the most finely discriminated petrographically associated group of coeval inclusions (Diamond, 1990; Goldstein and Reynolds, 1994; Bodnar, 2003a). Implicit in the FIAs definition is that they yield consistent temperature-pressure-composition (P-T-X) data.

Secondary inclusions are trapped after crystal growth along micro-fractures, while pseudosecondary fluid inclusions are found along fractures that terminate within the crystals and represent the fluids that were trapped along fractures that formed and healed during crystal growth (Roedder, 1979). Thermometric data obtained from fluid inclusions is a standard tool for constraining the pressure-temperature-composition (P-T-X) history of fluids associated

with geologic processes spanning the sedimentary to metamorphic to igneous environments (Roedder, 1984).

5.2 Methods

Doubly polished sections (200 to 100 µm thick) of quartz and calcite from sulfide-bearing veins were initially studied by optical microscopy in transmitted light using a Nikon Eclipse LV100N POL…. and subsequently subjected to microthermometry using a Linkam THM 10035 heating-freezing stage attached to a Nikon Eclipse LV100N POL polarizing microscope. Microthermometric investigations were performed mainly on primary fluid inclusions hosted by quartz following the procedures given in Goldstein and Reynolds (1994). Microthermotric analysis included the freezing temperature Tf, the ice melting temerature, Tm, and the homogenization temperature of the fluid phase by vapor disappearance Th. Salinity was calculated using the equations of Bodnar (1993): Salinity $=0.00+1.78\theta-0.0442\theta^2+0.000557\,\theta^3$, where θ is the depression of the freezing point in degrees Celsius (Bodnar, 1993). Details on the estimation of analytical errors and calibration materials are as follows: calibration compounds used (melting temperature): liquid CO_2 (-56.6 °C), n-Dodecane (-9.6 °C), n-Tridecane (-5.5 °C), pure water (0 oC), n-tetradecane (5.5 °C), benzanilide (+163 °C), sodium nitrate (+308 °C), potassium dichromate (+398 °C), and cupric chloride (+498 °C). Analytical error is less than ±0.1 °C for T<0 °C and ±1 °C for T> 0 °C.

5.3 Microthermometry

Two types of fluid inclusions are distinguishable in quartz from Cu-bearing quartz-calcite veins; (1) aqueous-dominant two-phase (type-1; L+V; Fig. 5.1), and (2) subordinate pure-liquid single-phase (type-2) fluid inclusions. The fluid inclusions preserve shapes ranging from irregular to equant and exhibit well defined growth zones. Both primary and secondary fluid inclusions range in size between 2 and 20µm. The ratio of the vapour phase ranges between 10 and 15% and the gas phase shrinks during heating and homogenizes to liquid. The type-1 primary fluid inclusions homogenized at 153-178 ^{o}C (Table 5.1) with salinities that range between 19 and 24.6 wt.% NaCl equivalent. There is little to no obvious variations from one drill hole to another in homogenization temperatures or salinities. Fluid inclusions in calcite are very tiny and rare. A pressure correction was performed following the isochore criteria given in Bodnar and Vityk (1994) for NaCl-H_2O systems, to estimate the fluid trapping temperatures. Calculated lithostatic pressures at the base of Ghanzi Group (5.5 km) and the Kgwebe Formation combined with the Ghanzi Group (7.5 km), range between 1.45-1.98 kbar. Using an average lithostatic head of 2700kg/m^3, along with the total average homogenisation temperature value of ~155°C measured for the Zone 5 primary two-phase aqueous inclusions, the corresponding trapping temperatures range between 236 -265°C.

Table 5.1 Fluid inclusion microthermometric results for the Zone 5 deposit. The data are from both this study and previously unpublished datasets

Sample	Location	FI type, host mineral	Number of phases	First $T_{melt\ ice}$ (°C)	$T_{melt\ hydrohalite}$ (°C)	Final $T_{melt\ ice}$ (°C)	Salinity (wt.% NaCl equiv)	$T_{homogenization}$ (°C)	Reference
1123, F-1	Zone 5	(P), quartz	2 (L+V)	-24.2	-	-19.9	21.3	178	This study
1123, F-2	Zone 5	(P), quartz	2 (L+V)	-26	-	-20.7	21.9	153	
1123, F-3	Zone 5	(P), quartz	2 (L+V)	-25.3	-	-23	23.4	164.4	
1123, F-4	Zone 5	(P), quartz	2 (L+V)	-26.6	-	-16.6	19.0	111	
1123, FA-1	Zone 5	(P), quartz	2 (L+V)	-25.8	-	-25	24.6	160	
1123, FA-2	Zone 5	(P), quartz	2 (L+V)	-25.4	-	-23.5	23.7	160.8	
z5-1, K-12	Zone 5	(S), not reported	2 (L+V)	-	-	-5.2	8.1	119.6	K. Morgan (2013) unpub. MGeol thesis
z5-1, K-13	Zone 5	(S), not reported	2 (L+V)	-	-	-7.6	11.2	146.2	
z5-1, K-14	Zone 5	(S), not reported	2 (L+V)	-	-	-6.6	10	136.8	
z5-1, K-15	Zone 5	(S), not reported	2 (L+V)	-	-	-2.4	4	119.8	
z5-1, K-16	Zone 5	(S), not reported	2 (L+V)	-	-	-5.9	9.1	115.1	
592-3, FL-9	Zone 5	(S), not reported	2 (L+V)	-50.52	-18.02	-12.42	16.36	-	G. Shepahard (2014) unpub. MGeol thesis
592-3, FL-10	Zone 5	(S), not reported	2 (L+V)	-50.5	-21	-14.6	18.3	148.3	
592-3, FL-11	Zone 5	(S), not reported	2 (L+V)	-	-	-11.5	15.47	120.2	
592-3, FL-12	Zone 5	(S), not reported	2 (L+V)	-49.5	-15.6	-12.3	16.24	165.1	
592-3, FL-13	Zone 5	(S), not reported	2 (L+V)	-49.5	-20.6	-20.6	18.88	139.4	

$T_{melt\ ice}$ is the melting temperature of ice; $T_{melt\ hydrohalite}$ is the melting temperature of hydrohalite; $T_{homogenization}$ is the temperature at which fluid and fapor homogenize into a single liquid phase
L=liquid; V=vapor; - = no data

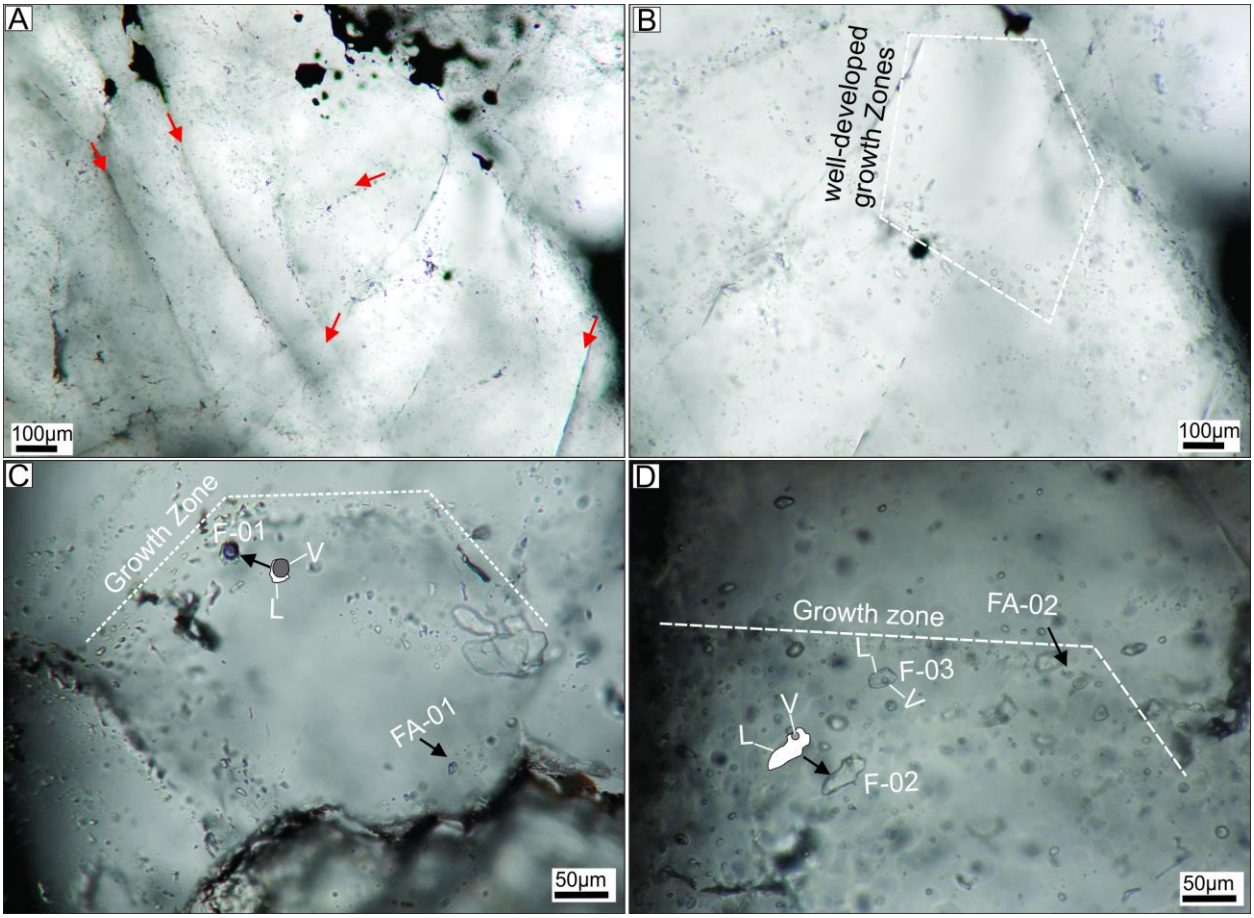

Figure 5.1 Plane light of microphotographs of fluid inclusions hosted in quartz (A-D) from quartz-calcite-sulfide veins. The fluid inclusions are predominantly two phase (L+V) aqueous inclusions. C) and D) show primary fluid inclusions examined by microthermometry. F= fluid inclusion, FA= fluid inclusion assemblage.

Chapter 6

STABLE ISOTOPES

6.1 Methods

Sulfur isotope ratios of seventeen (n=17) greater than 95% pure sulfide (pyrite, chalcopyrite, bornite, and chalcocite) samples, predominantly occurring as vein-hosted and minor disseminated ore were determined conventionally in the stable isotope laboratory at Akita University. The samples were carefully separated by handpicking under binocular microscope and a diamond-tipped microdrill .The $BaSO_4$ obtained from the sulfide minerals was packed with V_2O_5 in tin foil (Yanagisawa and Sakai, 1983). The packed samples were loaded into the automatic sampler attached to a Thermo Fisher Flash 2000 Elemental Analyzer, where the samples were subsequently combusted in a quartz tube at 1,020°C. SO_2 gas was separated by gas chromatography, and isotopic ratios were measured using a Thermo Fisher Scientific Delta V Advantage isotope ratio monitoring mass spectrometer at Akita University. Standards used in the analysis include IAEA NBS-127 ($\delta^{34}S$ CDT = 20.30‰), IAEA SO-6 (–34.10‰), and AEA SO-5 (0.50‰) (Halas and Szaran, 2001). Sulfur isotope values ($\delta^{34}S$) are given (Table 6.1) relative to the $^{34}S/^{32}S$ value of Canyon Diablo troilite (V-CDT) with a reproducibility of ±0.2‰. These analyses were directed at determining the probable source of sulfur for sulfides from high-grade quartz-calcite-sulfide veins as well as from minor disseminated ore.

Quartz and calcite were selected from hydrothermal sulfide-bearing veins to analyze the mineral oxygen and carbon isotopes. Crushed (150-200 mesh) and micro-drilled samples were

handpicked under binocular microscope. ^{18}O values for quartz samples were analyzed on Finnigan MAT Delta, dual inlet, isotope ratio mass spectrometer at Actlabs, Canada. Quartz samples were reacted with BrF_5 at ~650°C in nickel bombs following the procedures described in Clayton and Mayeda (1963). The fluorination reaction converts O in the mineral(s) to O_2 gas, which is subsequently converted to CO_2 gas using a hot C rod. All reaction steps are quantitative. The data are reported in the standard delta notation as per mil deviations from V–SMOW. External reproducibility is ± 0.19‰ (1σ) based on repeat analyses of internal white crystal standard (WCS). The value for NBS 28 is 9.61 ±0.10‰ (1σ). Isotopic ratios for ^{18}O and ^{13}C of calcites were determined on Finningan Mat, DeltaPlus XL IRMS system at Actlabs, Canada. At 50°C, calcite was reacted with phosphoric acid (100%) to release CO_2. The $\delta^{13}C$ and $\delta^{18}O$ values were measured from the CO_2. Two international standards, NBS 18 and NBS 19, and one calibrated internal standard were analyzed under the same conditions as the samples. Results were corrected and reported against Vienna Peedee Belemnite (VPDB) (Coplen, 1996). All standards are corrected to NBS-19 ($\delta^{13}C$ = 1.95‰ and $\delta^{18}O$ = -2.20‰) and NBS-18 ($\delta^{13}C$ = -5.05‰ and $\delta^{18}O$ = 23.1‰).

6.2 Sulfur isotopes

The results from conventional sulfur isotope analyses generated in this study are given in Table 6.1 and Figure 6.1. The sulfide samples (n=17) display a wide range of generally depleted $\delta^{34}S$ values of between +11.4 and -35.8‰. Two recrystallized framboidal pyrite samples yielded +11.4 and -35.8‰ $\delta^{34}S$ values. A hydrothermal pyrite porphyroblast (cubic and rimmed by

bornite) sample shows a $\delta^{34}S$ of -25.5‰. Chalcopyrite and bornite yield a broad range of $\delta^{34}S$ values; between +2.9 and -28.1‰ for chalcopyrite and +0.1 to -22.5‰ for bornite. Chalcocite contains moderately negative $\delta^{34}S$ values ranging from -10.9‰ to -22.1‰. Thus, no clear difference is found among the sulfide species except that recrystallized framboidal pyrite shows the largest range of $\delta^{34}S$ values. Among the Cu sulfides, relatively high values (3.0 to -5.4‰) are obtained only from bornite and chalcopyrite, whereas chalcocite shows relatively low values (-10.9 to -22.1‰) together with bornite (-20.3 and -22.4‰) and chalcopyrite (-23.9 and -28.0‰).

A chart of S isotopic data versus distance from the footwall redbed sequence of the Ngwako Pan Formation suggests that $\delta^{34}S$ values generally increase with increasing height within the stratigraphic column (Fig. 6.1). When the $\delta^{34}S$ values plotted as a function of host lithology (Fig. 6.2), sulfides in carbonate rocks and siltstone display relatively low and high S isotopic values with respect to the distance above the footwall clearly indicating that the source of S was different.

Table 6.1 Sulfur isotopic compositions for ore minerals from the Zone 5 deposit.

Sample	Description	Mineral	$\delta^{34}S$ (‰, V-CDT)
989-2	recrystallized framboidal pyrite	py	11.4
989-9	recrystallized framboidal pyrite	py	-35.8
962-1	pyrite porphyroblast rimmed by bn	py	-25.5
989-4	bedding-parallel qtz-cal-cpy vein	cpy	-23.9
1058-4	bedding-parallel qtz-cal-cpy vein	cpy	-28.0
1007-4	massive qtz-cal-cpy vein	cpy	-4.3
1012-5	cross-cutting coarse-grained qtz-cal-cpy vein	cpy	-5.4
1012-7	desseminated bedding-parallel qtz-cal-cpy vein	cpy	3.0
1020-1	sheared qtz-cal-bn-cc vein	bn	-22.4
952-3	qtz-cal-bn-cc vein	bn	-5.7
1014-2	sheared qtz-cal-bn-cc vein	bn	-20.3
962-3	sheared qtz-cal-bn-cc vein	bn	-4.9
967-2	coarse-grained qtz-cal-bn-cc vein	bn	0.3
1123-1	relative massive qtz-cal-bn-cc vein	bn	-5.2
921-4	randomly cross-cutting qtz-cal-bn-cc veins	cc	-22.0
715-5	coarse-grained qtz-cal-cc-hem-bn vein	cc	-10.8
715-4	strongly mineralized qtz-cal-cc-hem-bn vein	cc	-17.4

Note 1. Standards used: IAEA NBS-127 (δ^{34}SCDT= 20.30 ‰), IAEA SO-6 (-34.10 ‰), and IAEA SO-5 (-34.10 ‰) (Halas and Szaran, 2001).
Note 2. Sulfur isotope values ($\delta^{34}S$) are relative to $^{34}S/^{32}S$ value of Canyon Diablo troilite (V-CDT) with a resproducibility of ±0.2‰).

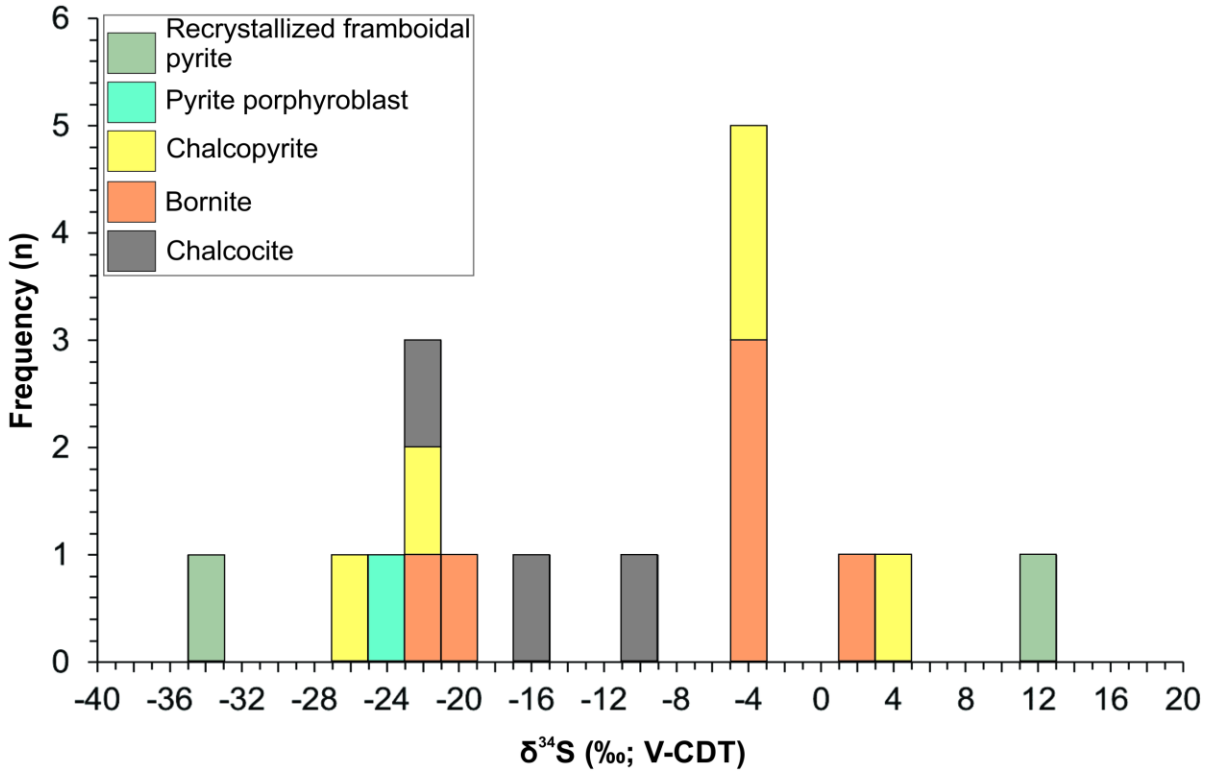

Figure 6.1 Histogram showing the distribution of $\delta^{34}S$ (‰, Vienna-Canyon Diablo Troilite [V-CDT) values of sulfides belonging to diagenetic and epigenetic mineralizing events at Zone 5.

6.3 Oxygen and Carbon isotopes

Carbon and oxygen isotopes were analyzed on a total of fourteen (14) samples, made of six different quartz-calcite mineral pairs and two other individual quartz and calcite mineral grains (Table 6.2). All the samples subjected C-O isotopic analyses were extracted from hydrothermal quartz-calcite sulfide-bearing veins. The results are shown in Table 6.2 and Figure 6.3. Quartz samples (n=7) preserve a narrow range of $\delta^{18}O$ isotopic values of between +13.0 to +17.5‰ V-SMOW. Calcite samples (n=7) yielded oxygen isotopic composition tightly ranging between $\delta^{18}O$ = -14.2 and -12.5‰ and carbon isotopic composition that varies

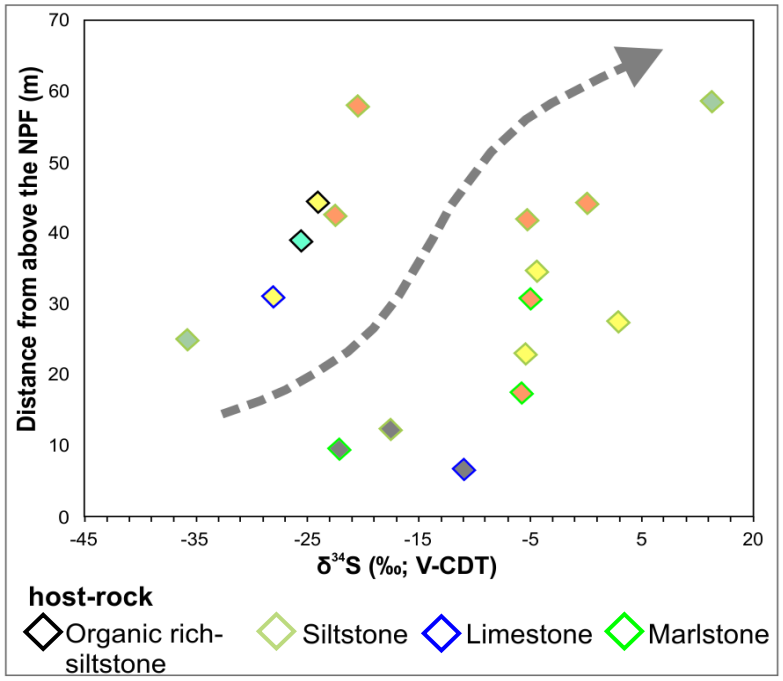

Figure 6.2 A trend illustrated the by $\delta^{34}S$ values against the distance from the footwall, suggesting that the ascending oxidized fluids gets isotopically heavier when interacting with more organic-rich sediments.

between $\delta^{13}C$ = -1.7‰ and +1.2‰. To estimate the temperature of precipitation, the equilibrium fractionation factors (1000lnα) for the oxygen isotopes used in this study were quartz-calcite: 0.38 $10^6/T^2$ (Clayton et al., 1989; for 600-1000) and quartz-calcite: 0.87 $10^6/T^2$ (Sharp and Kirschner 1994; for 100-700). Most quartz-calcite pairs have negative $\delta^{18}O_{qtz}$- $\delta^{18}O_{cal}$ values, suggesting disequilibrium. Likewise, one pair yielded 286 °C (using 0.38 $10^6/T^2$ fraction factor) and 590 °C (using 0.87 $10^6/T^2$ fraction factor).

Table 6.2 Carbon and oxygen isotopic compositions for quartz and calcite from the Zone 5 deposit.

Sample ID	Mineral	$\delta^{13}C_{V\text{-}PDB}$(‰)	$\delta^{18}O_{V\text{-}PDB}$ (‰)	$\delta^{18}O_{V\text{-}SMOW}$ (‰)
715-05b	Quartz			17.4
1049-02b	Quartz			14.9
1050-01b	Quartz			13.0
1123-05b	Quartz			15.9
1126-07b	Quartz			15.8
1170-04b	Quartz			16.4
1123-02	Quartz			17.5
715-05a	Calcite	-1.3	-14.2	16.3
1049-02a	Calcite	0.4	-13.4	17.1
1050-01a	Calcite	-0.6	-12.7	17.8
1123-05a	Calcite	1.2	-13.2	17.3
1126-07a	Calcite	-1.1	-13.7	16.8
1170-04a	Calcite	-1.7	-12.9	17.6
989-07	Calcite	-1.4	-12.5	18.0

Note 1. $\delta^{18}O_{quartz}$ in permil from V-SMOW. External reproducibility = ± 0.19 ‰ (1σ) based on repeat analyses of internal white crystal standard (WCS). NBS 28 = 9.61 ±0.10 ‰ (1σ).
Note 2. Calcite $\delta^{18}O$ and $\delta^{13}C$ reported against Vienna Peedee Belemnite (VPDB) (Coplen, 1996). NBS 18 and NBS 19 and one calibrated internal standard were analyzed under the same conditions as the samples. All standards corrected to NBS-19 ($\delta^{13}C$ = 1.95 ‰ and $\delta^{18}O$ = -2.20 ‰) NBS-18 ($\delta^{13}C$ = -5.05 ‰ and $\delta^{18}O$ = 23.1 ‰).

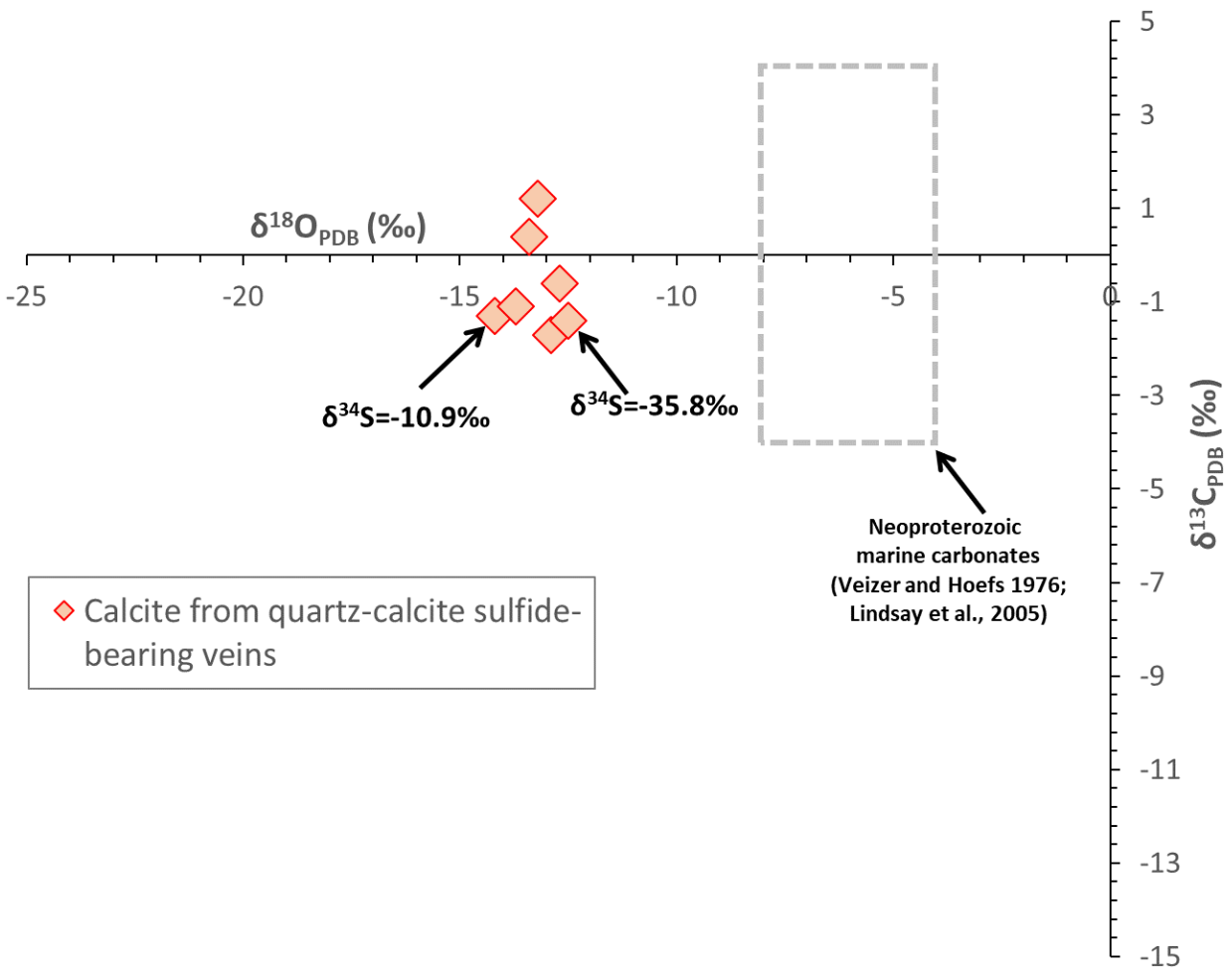

Figure 6.3. Plot of $\delta^{13}C$ and $\delta^{18}O$ of calcites from hydrothermal sulfide-bearing quartz-calcite veins in Zone 5 deposit.

Akita University

Chapter 7

DISCUSSION

7.1 Geologic framework: basin suitability for Cu-Ag mineralization

Although this thesis focuses on deposit-scale characterization, given the available field and geochronological datasets, it is also imperative to assess and identify the stages of basin evolution during which mineralization was permissible. The GCZ is a volcano-sedimentary basin that started accumulating at ~1110 to ~1085 Ma (Schwartz et al., 1996; Singletary et al., 2003; Hall et al., 2018a).

The first phase of tectonic evolution for the GCZ, is assigned to extensional tectonics and intracratonic rifting accompanied by bimodal magmatism (~1110 to ~1085 Ma; deposition of basal Kgwebe Formation; Fig. 2.3) and associated lacustrine to fluvial systems (Modie, 1996, 2000). The Ghanzi Group (~1050 to ~981 Ma; Hall et al., 2018a, 2021) is assigned to the second phase of basin evolution and is responsible for continued rifting (basin enlargement) which led to deposition of a siliciclastic sedimentary and carbonate packages, culminating in a marine transgression (Modie, 1996). The GCZ basin is a product of failed rifting (Modie et al., 1996) since there is no compelling evidence that the basin ever developed beyond an intracontinental rift (e.g. no fragments of ocean crust that would indicate of successful rifting).

The basin was subsequently inverted and metamorphosed during the Pan African Damara orogeny (~600 to 480 Ma), the period during which the basin highs, cored by

rheologically stronger bimodal volcanics, localized strain within mechanically weaker rock types (e.g. host meta-sediments of the Ghanzi Group), leading to the development of locally significant permeability and formation of structural trap sites (Fig. 7.1; Hall et al., 2018b).

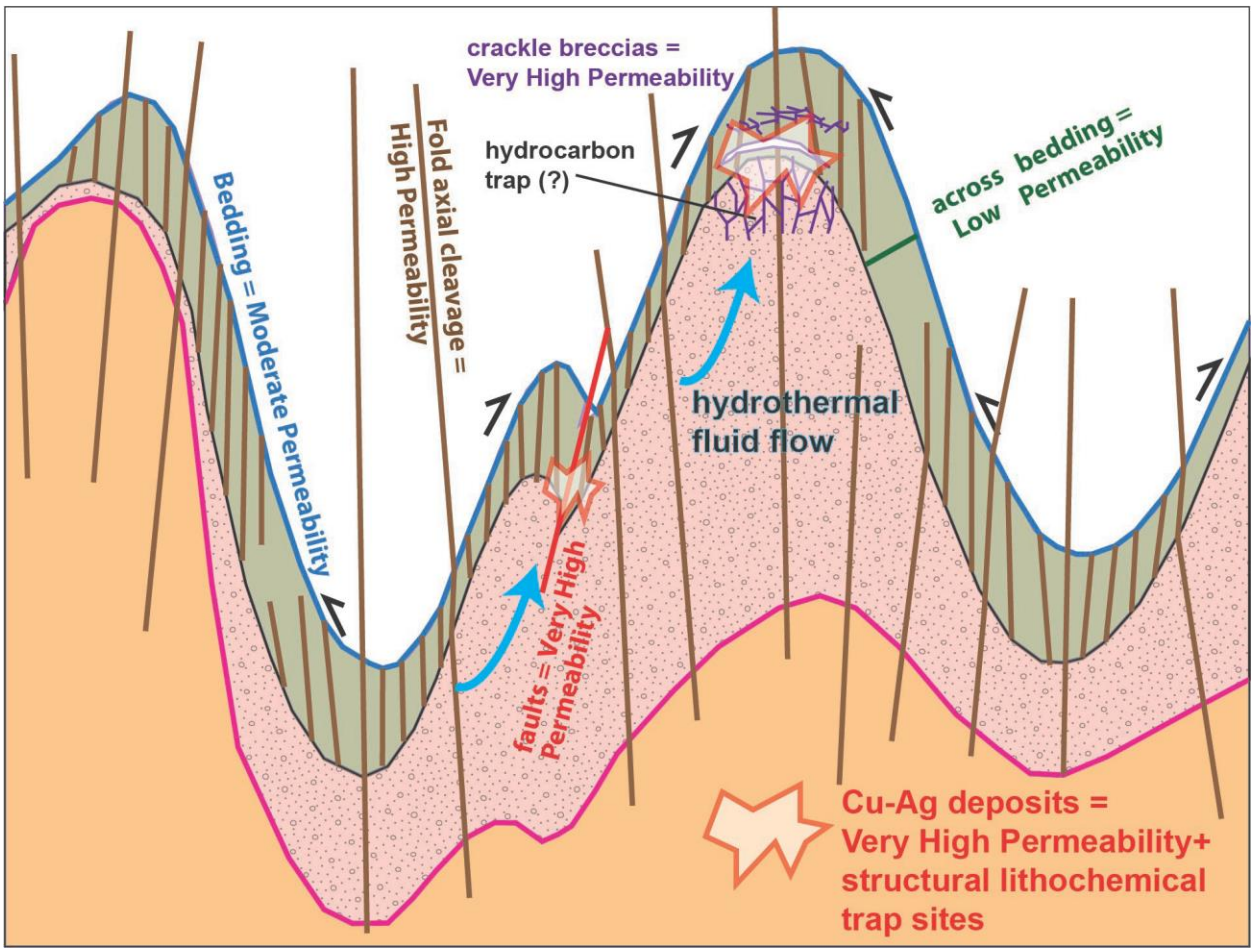

Figure 7. 1 Simple sketch representing a working model for the KCB, emphasizing qualitative differences in permeability within folded stratigraphy. The shortest distance between two layers (e.g. oxidized stratigraphy and reduced stratigraphy) is not necessarily the most likely pathway for fluids, because permeability perpendicular to bedding is typically very low. Discordances (e.g. basement vs basin fill) typically represent pre-existing zones of high

permeability in undeformed basins. During deformation, rheological contrasts across those contacts cause permeability to increase even further. Adapted from Hall et al. (2018b).

7.2 Lithological and structural control

Most of the Cu-Ag deposits in the Khoemacau district occur on the limbs and hinges of major folds (e.g. Hall et al., 2018b; Fig. 7.2). At Zone 5, metallic mineralization is hosted preferentially by the carbonate-siltstone metasedimentary package at the base of the D'Kar Formation, within 70 m of the continental redbeds of the Ngwako Pan Formation in the footwall. Localization of ore within the carbonate-siltstone units suggest that: i) these units possessed sufficient buffering capacity (abundant organic matter) to reduce the ascending oxidized metalliferous fluids and ii) a rheology that facilitated the necessary fluid propagation.

The host metasediments also acted as hydrological seals/barriers to slow down further up-depth migration of metalliferous fluid and, potentially, lead to metallic enrichment to ore grades. Drill core examination demonstrates that ore is distributed along bedding, foliation, crenulation cleavage, and shear zones (Figs. 3.4, 3.5) indicative of a mixture of rheological and chemical controls on mineralization.

The mineralization at Zone 5 is vertically zoned, in ascending order, from hematite to chalcocite to bornite to chalcopyrite to an outer halo of pyrite-galena-sphalerite. Given the localization of the ores at an oxidizing to reducing boundary, this metal zonation may be linked to the transition from oxidizing to reducing conditions and to the availability of reduced sulfur in the host metasediments.

Ubiquitous, overall layer-parallel mineralization is composed of low-grade disseminated ore as well as high-grade veinlet mineralization. Some of the high-grade quartz-calcite-sulfide veins are brecciated and boudinaged parallel to bedding or foliation subsequent to strike-slip movements at deposit scale (e.g. layer-parallel shearing; Fig. 3.5A). These bedding-parallel veins are typical “striped bedding veins” of Koehn and Passchier (2000) and are interpreted to be a result of bedding parallel slip during the early stage of deformation in the Damara Orogen (Maeder et al., 2014). Two other types of mineralized veins observed at Zone 5 are discrete, high-angle cross-cutting quartz-calcite-sulfide veins and randomly crosscutting, interconnected veins, which are indicative of multiple generations of quartz-calcite veining. Steep, discordant veins appear to act as feeder zones to contiguous mineralization along bedding and foliation planes (Fig. 3.4C, E), indicating a close spatial and temporal relation between vein-hosted and disseminated (layer-parallel) metallic mineralization.

A subset of the high-angle sulfide-bearing veins and veinlets is parallel to crenulation cleavage (Fig. 3.4) indicating contemporaneity with deformation. This set of veinlets acted as conduits along which ore fluids propagated to precipitate ores along crenulations preferentially in sandy/silty (porous) layers. In agreement with Maeder et al. (2014), all these mineralization styles can be explained by progressive folding that caused flexural slip along the bedding planes in incompetent layers and fan-shaped fracturing and axial plane cleavages in competent layers centered on the fold hinge plane.

Drill core examination coupled with petrographic observations indicate that mineralized quartz-calcite veins suffered both brittle and ductile deformational overprinting, suggesting that some metallic mineralization was introduced pre-deformation. While it is challenging to

decipher the structural paragenesis and deformational history at Zone 5, our observations suggest that the ore grade, structurally controlled mineralization was a consequence of a regional deformational event. These local structural fabrics represent a fold-limb environment and indicate that flexural slip and crenulation cleavages were the most important mechanism during regional progressive folding (e.g. Maeder et al., 2014; Hall et al., 2018b). Given the rheological contrast that exist at the redox interface, the strain was localized in the mechanically weaker carbonate-siltstone package (e.g. Hall et al., 2018b), producing the necessary structural permeability as the rocks had already solidified at the time of hydrothermal activity.

7.3 Cu-Ag ore stages and paragenesis

Across the Zone 5 deposit, chalcopyrite, bornite, and chalcocite are the principal Cu-(Fe)-sulfide minerals, accompanied by minor pyrite, arsenopyrite, galena, and sphalerite. In our paragenetic analysis (Fig. 4.1) two principal hypogene mineralization stages can be distinguished: (1) A diagenetic stage which is represented mainly by fine-grained pyrite and minor associated ore minerals. (2) A hydrothermal Cu-Ag stage characterized by formation of early to late hydrothermal Cu-Ag sulfides with accompanying hydrothermal alteration. In both mineralizing stages, quartz and calcite are the main host rock and gangue mineral phases. In addition, recent studies have reported some mineral species not identified yet in our study (e.g., Pd-Hg tellurides associated with Cu sulfides at Boseto deposit; Piestrzynski et al., 2015; Fig. 4.1).

7.3.1 Diagenetic ore stage

The diagenetic origin is proposed for an early stage of metallic (mainly fine-grained, commonly framboidal pyrite) mineralization on the basis of the following textural and morphological features (Fig. 4.2): a) the presence of fine-grained pyrite confined to the more organic-rich layers, b) the occurrence of fine-grained intergranular pyrite intergrown with diagenetic host rock minerals (quartz, calcite, plagioclase, k-feldspar, and muscovite) forming pyritic laminations, c) the occurrence of nodular-shaped pyrite and pyrite layers parallel to bedding/lamination, d) the occurrence of framboidal pyrite clusters and recrystallized framboidal pyrite, commonly overgrowing lithological layering, and e) suhedral to euhedral pyrite forming in former Mg-calcite nodules. The interpretation given here for this stage of pyrite is consistent with Schieber (1990) who proposed that fine-grained pyrite concentrated in crumpled lamination can be linked to formation of microbial mats and a diagenetic origin, often unrelated to hydrothermal activity.

Framboidal texture is commonly interpreted as evidence of syngenesis since such texture is indicative of direct precipitation of FeS_2 from solution (Berner, 1964, 1970) or bacterial reduction of seawater sulfate (Annels, 1974; Sweeney et al., 1987). Furthermore, laboratory experiments carried out at a temperature above 60°C indicate that the iron mono-sulfides produced by bacterial sulfate reduction during sedimentation would subsequently be transformed to framboidal pyrite by reaction with excess hydrogen sulfide (Butler and Rickard, 2000). Petrographic analyses revealed an intergrowth of diagenetic pyrite with galena, sphalerite, chalcopyrite, (Ni, Co, Fe) sulfarsenide, apatite, and REE-aluminosilicate (Figs. 4.2). These textural relations suggest that the non-pyrite sulfides observed with diagenetic pyrite are

likely late diagenetic in origin. This interpretation is supported by Hall et al. (2021), who suggested that the deposition of organic-rich mudstone in the KCB may have been accompanied by a diagenetic (disseminated to veinlet) metallic mineralization event.

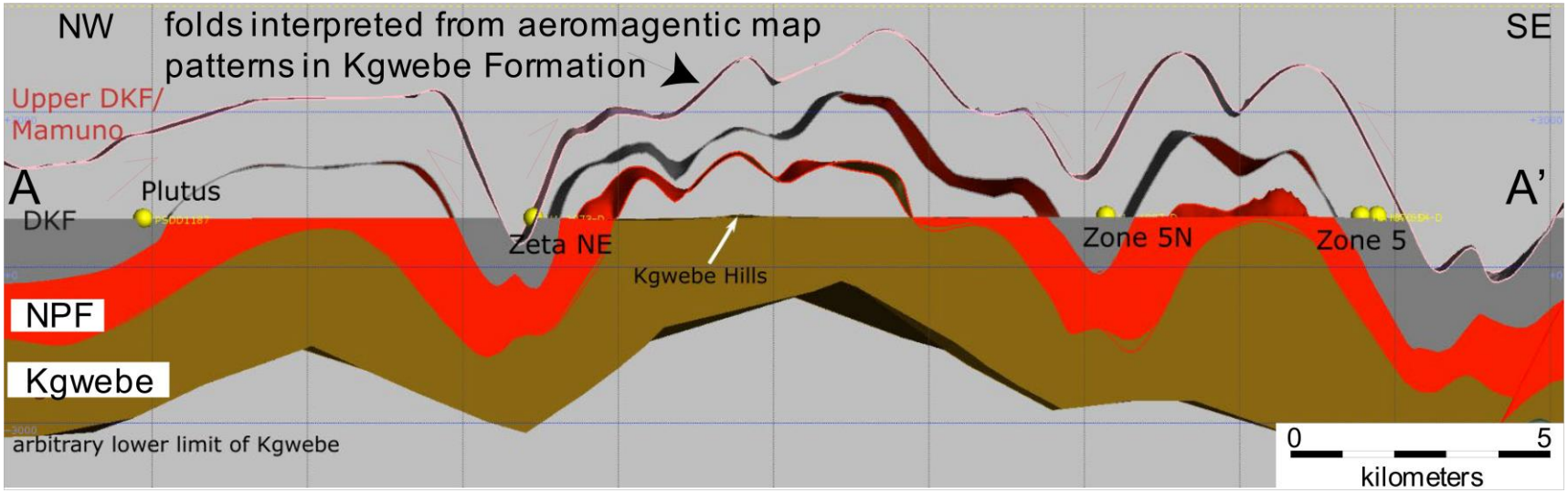

Figure 7.2 NW-SE cross-section shown in Figure 3.1 through a regional 3D model that was produced for exploration purposes. It shows the general shape of regional-scale folds (as well as the position of major thrusts) and variations in thickness of key formations with the area. The bottom limit of the Kgwebe Formation is arbitrary because there is no data available for the true thickness of this basal unit comprised of mafics. Nearly all the deposits sit at or just above the contact of oxidized Ngwako Pan Formation (red beds) and reduced base of the D'Kar Formation. The Zone 5 deposit is situated on a SE limb of an antiform that can be traced for at least 100 km through much of the GCZ. Adapted from Hall et al. (2018b)

Recently, Hall et al. (2021) reported a ~981 Ma Re-Os molybdenite age to correspond with the diagenetic-early hydrothermal mineralizing event in the KCB. Although our EPMA data offers little diagnostic evidence due to high detection limits, the available trace elemental results allow a distinction between this diagenetic-early hydrothermal stage and the main-stage Cu-Ag hydrothermal stage (see below; Fig. 4.5 or Appendix B). The major constituents (pyrite, galena, sphalerite) during the diagenetic-early hydrothermal stage, are generally Cu and Ag poor compared to the overprinting Cu-(Fe) sulfides. However, trace element trends indicate that the early stage was comparably enriched in Ni, Co, Fe, As, Zn, and Pb.

7.3.2 Main Cu-Ag hydrothermal ore stage

An epigenetic hydrothermal Cu-Ag mineralization stage accounts for the existence of the Zone 5 deposit and the formation of other Cu-Ag deposits in the Khoemacau district and the KCB. This ore stage is dominated by Cu mineralization and is syn-orogenic and multi-stage, likely the result of a complex, prolonged history. Mineralization is characterized by a simple suite of Cu sulfides (chalcopyrite-bornite-chalcocite) which display a variety of intimate intergrowth textures, indicating their co-crystallization. Just like the stratiform disseminated pyrite of the diagenetic stage, sulfides at this stage also form dissemination within the host rock. However, the Cu sulfides are distinctively coarse-grained and preferentially grow along structural fabric, such as foliation, veins, crenulation cleavage, and shear zones, indicating a syn-orogenic origin. Minor sulfidic phases such as galena, pyrite, arsenopyrite, cobaltite, glaucodot, and (Ni, Co, Fe) sulfarsenide appear to precede Cu mineralization (Fig.4.1), as they occur either as inclusions or

are replaced by Cu sulfides. Although assay data indicate a strong positive correlation between Cu and Ag, Ag minerals are not common at Zone 5 effectively suggesting that Ag is largely refractory within the Cu sulfide crystal lattice. However, micro-XRF and SEM-EDS analyses reveal the occurrence of minor native Ag around chalcocite crystal margins, indicating that some Ag mineralization may have been part of a late ore fluid.

The current likely timing for folding and thermal events in the KCB is constrained from $^{40}Ar/^{39}Ar$ white-mica crystallization ages of ~568 ± 3 to 553 ± 3 Ma (Gray et al., 2006) and K-Ar white mica crystallization ages of ~530 to ~480 (Ahrendt et al., 1978; Gray et al., 2006) from the Damara belt in Namibia. Furthermore, Hall et al. (2021) reported precise U-Th-Pb xenotime (~538 Ma) and chalcocite Re-Os (~515 Ma) ages for epigenetic mineralization in the KCB. Combining the geochronological data and the integrated evidence presented here, we propose that the main stage of Cu-Ag mineralization at Zone 5 is associated with a prolonged episode of hydrothermal activity which is overall synchronous with regional deformation and metamorphism.

The primary objective of our EPMA trace element study was to constrain Ag deportment in the ore. The probe data indicate that bornite, chalcocite, and covellite are the preferential hosts for Ag, while chalcopyrite is comparably Ag-poor (Fig. 4.5). Silver enrichment in the overprinting covellite indicate that late hydrothermal processes also contributed to increased Ag budget in the ore. Kelepile et al. (2020) found similar trends when comparing Ag concentrations between Cu-(Fe)-sulfide minerals in the KCB and attributed such trends to the tendency of Ag to partition preferentially into Cu-rich phases. Bornite generally has a higher mean (0.22 wt. %) for Ag than chalcocite (0.18 wt. %).,

On the basis of entrapment pressure-corrected fluid inclusion temperatures, the fluids responsible for the hydrothermal Cu-Ag mineralization were hot (~236-265°C) with relatively high salinity (~19-24.6 wt. % NaCl equiv.). These values are consistent with previously reported entrapment temperatures (250-300 °C) and salinities from 4 to 25 wt. % NaCl-($CaCl_2$) equivalent for the KCM (Hall et al., 2018b). An ascending fluid flow model was investigated by Hall et al. (2018b) which revealed Zn and Pb haloes overlying high Cu grades. The mineralizing fluids propagated through brittle structures and along lithological layering. The widespread contiguous bedding-parallel mineralization provides evidence that ore fluids which initially propagated through structural permeable zones were later redirected to follow lithological layering due to limitations in permeability across strata.

7.3.3 Origin of sulfur

The results of the S isotopic analyses shed light on the origin of S in both the diagenetic and epigenetic hydrothermal metallic mineralization stages as well as on the redox state of the Zone 5 deposit. Figure 6.1 shows $\delta^{34}S$ values plotted against the distance of the studied sample above the footwall Ngwako Pan Formation. The data show a general trend towards positive values with increasing distance away from the footwall unit. This trend indicates a transition from oxidizing to more reducing conditions, generally reflecting heavier S isotopic compositions as a result of interaction with more reduced host rocks. The $\delta^{34}S$ values obtained for Zone 5 Cu-Ag deposit sulfides display a wide range of -35.4 to 11.8 ‰ and a large number of light S isotopic compositions. This highly negatively-skewed variation is reminiscent of isotopic

disequilibrium requiring multiple sources of S in the hydrothermal fluids. Two variably recrystallized framboidal pyrite samples yielded values (+11.4‰ and -35.8‰) that fall on either side of the total S isotopic spread for Zone 5, and which are consistent with bacteriogenic derivation of S. Thus, the formation of diagenetic (framboidal) pyrite appears to be linked to H_2S generated by bacterial sulfate reduction and reactive iron (Raiswell and Berner, 1985).

Main stage hydrothermal sulfides in quartz-calcite-sulfide veins display a wide total range of $\delta^{34}S$ values (-28.1 to 3.0‰); however, a large number of measurements occur within a narrower range of comparatively heavier isotopic values (-5.7 to +3.0‰) that averages close to zero ‰. The remaining values are depleted in ^{34}S and range between -28.1 and -10.8 permil, overlapping a $\delta^{34}S$ value of -25.6‰ measured in an ore-stage pyrite porphyroblast rimmed by bornite. The narrower range of comparatively heavier isotopic values may imply a magmatic-hydrothermal input of S, while the strongly negative and wide range isotopic composition is linked to an origin from extreme fractionation of sedimentary sulfate by bacterial sulfate reduction (Ohmoto & Goldhaber, 1997). The overlap between pyrite (both diagenetic or early-hydrothermal) and main stage Cu sulfides indicate that S was in part derived from earlier formed sulfides. The intimate intergrowth and textures indicative of replacement between early pyrite and main stage Cu sulfides support the existence of S inheritance. This is consistent with the conclusion in previous studies (e.g. Ruxton, 1981; Hall et al., 2018b, 2021) that strong negative S isotopic anomalies and large $^{34}S/^{32}S$ ranges in the KCB, suggest that S may have been derived in-situ from organic matter within the host meta-sediments and/or sourced via remobilization of bacteriogenic pyrite.

A comparison of the $\delta^{34}S$ results obtained in this study against other studies of Cu mineralization in the KCM (Hall, 2013; Shepard, 2014; Hall et al., 2021) shows a strong overlap. Consistently with these previous studies, no evidence was found for a direct evaporitic source of S. The available estimated mean $\delta^{34}S$ value suggested for Neoproterozoic seawater is +17 ± 3 permil for the Roan Group of the Central African Copperbelt (El Desouky et al., 2010 and references therein). The $\delta^{34}S$ values obtained for the Zone 5 show a considerable offset of ~6 to -53 permil (δSO_4-sulfide) compared to the Neoproterozoic seawater (Fig. 7.3). This large range of isotopic fractionation is consistent with fractionations for bacterial sulfate reduction (15‰ to 60‰; Ohmoto 1986; Machel et al., 1995).

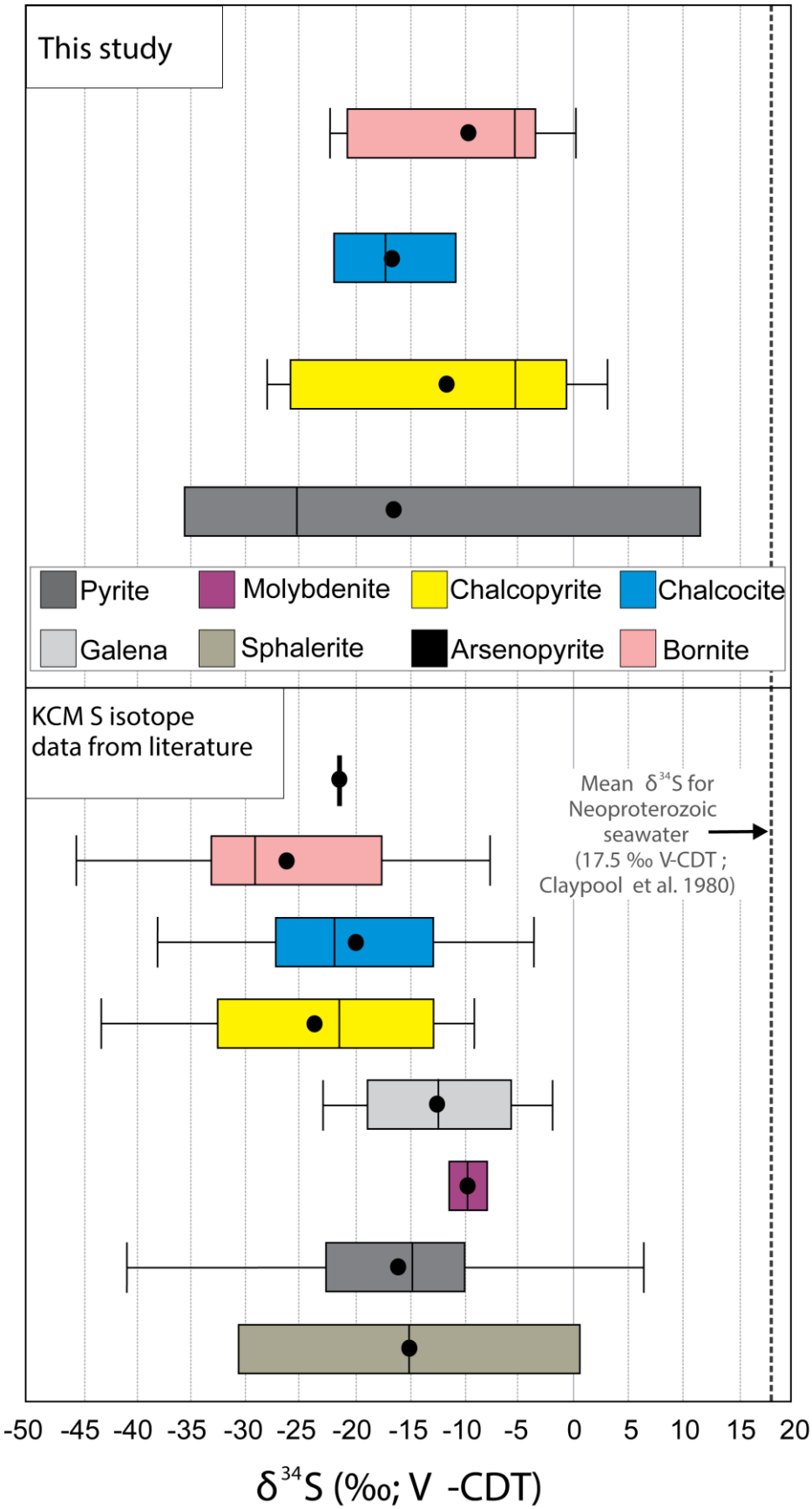
This study
Pyrite
Molybdenite
Chalcopyrite
Chalcocite
Galena
Sphalerite
Arsenopyrite
Bornite
KCM S isotope data from literature
Mean δ34S for Neoproterozoic seawater (17.5 ‰ V-CDT ; Claypool et al. 1980)
-50 -45 -40 -35 -30 -25 -20 -15 -10 -5 0 5 10 15 20
δ34S (‰; V -CDT)

224

Figure 7.3 Box and whisker plots showing $\delta^{34}S$ (‰, V-CDT) values for the Zone 5 plotted against previously reported $\delta^{34}S$ values for the Kalahari Copperbelt (KCB) in Botswana. Data from other deposits include the Boseto deposit (Hall, 2013), Zone 5 (Shephard, 2014), Zone 6 (Shephard, 2014; Hall et al., 2021), Northeast Fold (Hall et al., 2021), Northeast Mango Two (Hall et al., 2021). These values are compared with the available mean $\delta^{34}S$ for Neoproterozoic seawater sulfate (17.5‰; Claypool et al., 1980).

7.3.4 Carbon and oxygen isotopes

Carbon and O isotopic data offer insights into the redox state of mineralizing fluids. At Zone 5, calcite from Cu-bearing quartz-calcite veins preserve lighter stable isotopic signatures, in particular lighter $\delta^{18}O$ values. The ranges proposed in the literature for $\delta^{18}O$ and $\delta^{13}C$ values for Neoproterozoic marine carbonates are -8 to -4 ‰ for $\delta^{18}O$ and -4 to +4 ‰ for $\delta^{13}C$ (Veizer and Hoefs, 1976; Lindsay et al., 2005). The $\delta^{18}O$ values measured at Zone 5 (-14.2 to -12.5‰) display a significant shift from the range proposed for Neoproterozoic marine carbonates (depleted by 6.2 to 8.7‰; Fig. 6.2), while the $\delta^{13}C$ isotopic values (-1.7 to 1.2‰) fall within the proposed range.

The significant offset displayed by $\delta^{18}O$ isotopic values is likely attributable to recrystallization during Cu-Ag mineralization stages (El Desouky et al., 2009c). This explanation is consistent with our petrographic evidence that indicates recrystallization of quartz and calcite. Muchez et al. (2010) alternatively suggested that these negative shifts could be related to high mineralization temperature. The oxygen isotope system is less stable than the carbon isotope system, which does not show significant reequilibration up to greenschist facies conditions (Holser et al., 1988; Schidlowski, 1988). On the other hand, $\delta^{13}C$ isotopic

composition for calcite may likely not have been affected by metamorphism or syn-orogenic hydrothermal activities. In the Central African Copperbelt, some deposits preserve significant variation in the carbon isotope values (Selley et al., 2005; El Desouky et al., 2010).

This scenario is explained by the interaction between the oxidized metal-bearing brines and reduced organic-rich metasediments which would have caused oxidation of organic matter (Selley et al., 2005; El Desouky et al., 2010). At Zone 5, however, the extent to which organic matter was oxidized is uncertain. Previous C-O isotopic studies (Hall, 2013; Morgan et al., 2013, Shephard et al., 2013; Morgan et al., 2014) within KCM yielded in the $\delta^{13}C$ and $\delta^{18}O$ values which are too comparable with values obtained in this study.

Akita University

Chapter 8

CONCLUSIONS

8.1 Conclusions

Through a combination of drill core examination, petrographic, trace elemental, stable isotopic, and fluid inclusion microthermometric analyses, this research has demonstrated that the oxidation-reduction boundary between the continental red beds and overlying marine siliciclastic and carbonate units was the first-order control on the Cu-Ag mineralization in the Zone 5 deposit. The rheological contrast at the redox interface was equally critical in facilitating ore fluid propagation and subsequent precipitation.

A variety of mineralization styles are present in the Zone 5 deposit: lower-grade, disseminated ore along bedding of foliation planes indicates a significant lithological control, while higher-grade Cu-Ag mineralization occurs in structural sites, including hydrothermal breccia, crenulation cleavage, and shear zones.

Petrographic and mineral chemical evidence allows for distinction between two mineralizing events at Zone 5. A diagenetic stage mineralization formed soon after deposition of the organic-rich sediments at ~981 Ma (Hall et al., 2021) producing stratabound fine-grained framboidal pyrite together with minor amounts of a variety of metals (Cu, Zn, Pb, Ni, Co, Fe, As, Bi, Sb). On the other hand, the main stage of economic Cu-Ag mineralization was linked to a Damaran age (~515-549 Ma; Hall et al., 2021) hydrothermal system. Excluding Co and Ni, the Cu-Ag mineralization was accompanied by similar metal assemblage of Cu, Ag, Ti, Fe, Pb, Zn, As, Bi, and Sb. Given the more than 400 m.y. hiatus (Hall et al., 2021) between the two events, the

similar metal assemblages can be explained in part by remobilization of earlier formed ore minerals. Textural overprinting by the main stage Cu-(Fe)-sulfides on diagenetic-early hydrothermal sulfides support this explanation.

Although there is a partial overlap in trace metal concentrations, diagenetic stage sulfides are Cu and Ag poor, while the Cu-(Fe)-sulfide (bornite, chalcocite, and bornite) system of the epigenetic hydrothermal stage is the main carrier of Ag. Fluid inclusion microthermometric data indicates that quartz from cupriferous quartz-calcite veins precipitated from ascending hot (236-265°C) and highly saline (19-24.6 wt.% NaCl equiv.) ore fluids.

Sulfur isotopic data points towards multiple sources of reduced S. Consistent with metallic remobilization, textural overprinting of diagenetic sulfides by hydrothermal stage cupriferous sulfides suggests that the highly depleted and variable $\delta^{34}S$ values were in part inherited from earlier formed bacterially reduced sulfides.

The $\delta^{13}C$ and $\delta^{18}O$ isotopic for calcites derived from sulfide-bearing veins are broadly consistent with reported isotopic values by previous authors in the KCB and other Neoproterozoic sediment-hosted Cu-Ag deposits. The $\delta^{18}O$ isotopic composition shift from established range of Neoproterozoic marine carbonates, is indicative of syn-orogenic origin of mineralization and also imply the role played by metamorphic fluids.

Chapter 9

REFERENCES

9.1 References

Ahrendt, H., Hunziker, J.C., and Weber, K. (1978) Age and degree of metamorphism and time of nappe emplacement along the southern margin of the Damara orogen/Namibia (SW-Africa). Geologische Rundschau, 67, 719-742.

Annels, A.E. (1974) Some aspects of the stratiform ore deposits of the Zambian Copperbelt and their genetic significance. In: Bartholomé, P. (Ed.), Gisements stratiformes et provinces cuprifères. Centenaire Société Géologique de Belgique, Liége, pp. 235-254.

Berner, R.A. (1964) Iron sulfides formed from aqueous solution at low temperatures and atmospheric pressure. Journal Geology 72, 293-306.

Berner, R.A. (1970) Sedimentary pyrite formation. American Journal of Science 268, 1-23.

Brown, A. C. (2009) A process-based approach to estimating the copper derived from red beds in the sediment-hosted stratiform copper deposit model. Economic Geology, 104, 857-868.

Butler, I.B., and Rickard, D. (2000) Framboidal pyrite formation via the oxidation of iron (II) monosulfide by hydrogen sulphide: Geochimica et Cosmochimica Acta, 64, 2665-2672.

Carney, J.N., Aldiss, D.T., and Lock, N.P. (1994) The geology of Botswana. Botswana Geological Survey Bulletin 37, pp. 113.

Claypool G.E., Holser W.T., Kaplan I.R., Sakai H., and Zak I. (1980) The age curves of sulphur and oxygen isotopes in marine sulphate and their mutual interpretation. Chemical Geology, 28, 99-260.

Clayton, R.N., and Mayeda, T.K. (1963) The use of bromine pentafluoride in the extraction of oxygen from oxides and silicates for isotopic analysis. *Geochimica et Cosmochimica Acta*, 27, 47-52.

Clayton, R.N., Goldsmith, J.R., and Mayeda, T.K. (1989) Oxygen isotope fractionation in quartz, albite, anorthite and calcite. *Geochimica et Cosmochimica Acta*, 53, 725-733.

Coplen, T. B. (1996) New guidelines for the reporting of stable hydrogen, carbon and oxygen isotope ratio data. *Geochimica et Cosmochimica Acta*, 60, 3359-3360.

El Desouky, H., Muchez, P., Boyce, A.J, Schneider, J., Cailteux, J.L.H., Dewaele, S., and von Quadt, A. (2010) Genesis of sediment-hosted stratiform copper-cobalt mineralization at Luiswishi and Kamoto, Katanga Copperbelt (Democratic Republic of Congo). Mineral Deposita,45, 735-763.

El Desouky, H.A., Muchez, P., and Cailteux, J. (2009) Two Cu-Co sulfide phases and contrasting fluid systems in the Katanga Copperbelt, Democratic Republic of Congo. Ore Geology Reviews, 36, 315-332.

Fall, A., Bodnar, R. J. (2018) How precisely can the temperature of a fluid event be constrained ` using fluid inclusions? Economic Geology, 113, 1817-1843.

Goldstein, R.H., and Reynolds, T.J., 1994, Systematics of fluid inclusions in diagenetic minerals: SEPM Society for Sedimentary Geology Short Course Manual, v. 31, 199 p.

Gorman, A., Jenkin, G., Catterall, D., and Holwell, D. (2013) Constraining a genetic model for copper-silver mineralization in the Kalahari Copperbelt, Botswana: mineralogy, geochemistry and structure. MGeol. Thesis, University of Leicester, Leicester, United Kingdom.

Halas, S., and Szaran, J. (2001) Improved thermal decomposition of sulfates to SO_2 and mass spectrometric determination of $\delta^{34}S$ of IAEA SO-5, IAEA SO-6, and NBS-127 sulfate standards: *Rapid Communications in Mass Spectrometry*, 15, 1618-1620.

Hall, W. S. (2013) Geology and paragenesis of the Boseto copper deposits, Kalahari Copperbelt, northwest Botswana: M.Sc. thesis, Golden, Colorado, Colorado School of Mines, 146 p.

Hall, W. S. (2017) Geochronology, magnetic lithostratigraphy, and the tectonostratigraphic evolution of the late Meso- to Neoproterozoic Ghanzi basin in Botswana and Namibia, and implications for copper-silver mineralization in the Kalahari Copperbelt. Ph.D. dissertation, Golden, Colorado, Colorado School of Mines, 62 p.

Hall, W. S., Stein, H. J., Kylander-Clark, A. R. C., Hitzman, M. W., Kuiper, Y, D., Knight, C., and Enders, M. S. (2021) Diagenetic and Epigenetic mineralizing events in the Kalahari Copperbelt, Botswana: Evidence from Re-Os sulfide dating and U-Th-Pb xenotime geochronology, Economic Geology, 116, 863-881.

Hall, W.S., Hitzman, M.W., Kuiper, Y.D., Kylander-Clark, A.R.C., Holm Denoma, C.S., Moscati, R.J., Plink-Bjorklund, P., and Enders, M.S., (2018a) Igneous and detrital zircon U-Pb and Lu-Hf geochronology of the late Meso- to Neoproterozoic northwest Botswana rift: Maximum depositional age and provenance of the Ghanzi Group, Kalahari Copperbelt, Botswana, and Namibia: Precambrian Research, 318, 133-155.

Hall, W.S., Knight, C., Catterall, D.J., Augenstein, C., Davies, B.M., Deane, J., Muyoba, B., Disang, O., Emsbo, P., Li, Y., Enders, M.S., and Hitzman, M.W. (2018b) Regional-to Deposit-Scale Geologic Controls on Copper-Silver Mineralization in the Kalahari Copperbelt, Botswana. *Society of Economic Geologists Special Publication*, 21, 207-236.

Hitzman, M.W, Selley, D., and Bull, S. (2010) Formation of sedimentary rock hosted stratiform copper deposits through Earth history. Economic Geology, 105, 627-639

Kelepile, T., Betsi, T.B., and Shemang, E. (2020) Metal sources and mineralizing fluids characteristics and evolution of the Khoemacau sediment-hosted Cu-Ag deposits, in the

Ghanzi-Chobe belt portion of the Kalahari Copper Belt. Ore Geology Reviews, 122, 103559.

Kelepile, T., Bineli Betsi, T., Franchi, F., Shemang, E., and Suh, C. E. (2017) Provenance and tectonic setting of the Neoproterozoic clastic rocks hosting the Banana Zone Cu-Ag mineralisation, northwest Botswana. Journal of African Earth Sciences, 129, 853-869.

Key, R.M., and Rundle, C.C. (1981) The regional significance of new isotopic ages from Precambrian windows through the “Kalahari Beds” in north-western Botswana. Transactions of the Geological Society of South Africa, 84, 51-66.

Koehn, D. and Passchier, C.W. (2000) Shear sense indicators in striped bedding veins. Journal of Structural Geology, 22, 1141-1151.

Large, R., Mukherjee, I., Gregory, D.D., Steadman, J.A., Maslennikov, V.V. & Meffre, S. 2017. Ocean and Atmosphere Geochemical Proxies Derived from Trace Elements in Marine Pyrite: Implications for Ore Genesis in Sedimentary Basins. Economic Geology, 112, 423-450.

Lehmann, J., Master, S., Rankin, W., Milani, L., Kinnaird, J.A., Nydenov, K.A., Saalman, K., and Kumar, M. (2015) Regional aeromagnetic and stratigraphic correlations of the Kalahari Copperbelt in Namibia and Botswana: *Ore Geology Reviews*, 71, 169-190.

Machel, H.G., Krouse, H.R., Sassen, R. (1995) Products and distinguishing criteria of bacterial and thermochemical sulphate reduction. Applied Geochemistry, 10, 393-389.

Maeder, X., Passchier, C.W., and Trouw, R.A. J. (2014) Complex vein systems as a data source in tectonics: An example from the Ugab Valley, NW Namibia. Journal of Structural Geology, 62, 125-140.

Maiden, K.J., and Borg, G. (2011) The Kalahari Copperbelt in central Namibia: Controls on copper mineralization: *Society of Economic Geologists Newsletter*, 87, 14-19.

Modie, B.N. (1996) Depositional environments of the Meso- to Neoproterozoic Ghanzi-Chobe zone, northwest Botswana. Journal of African Earth Sciences, 22, 255-268.

Modie, B.N. (2000) Geology and mineralization in the Meso- to Neoproterozoic Ghanzi-Chobe zone, northwest Botswana. Journal of Africa Earth Sciences, 30, 467-474.

Morgan, K.L., Jenkin, G.R.T, Catterall, D., Boyce, A.J., Gorman, A.R. (2013) Developing genetic models for copper-silver mineralization in the Kalahari Copperbelt, Botswana: Source and evolution of fluids. MGeol. Thesis, University of Leicester, Leicester, United Kingdom.

Ohmoto H. (1986) Stable isotope geochemistry of ore deposits. In: Valley JW, Taylor HP, O' Neil JR (eds) Stable isotopes in high temperature geological processes. Reviews in mineralogy. Mineralogical Society of America, 16, 491-559.

Ohmoto, H., Goldhaber, M.B. (1997) Sulfur and carbon isotopes. Geochemistry of hydrothermal ore deposits, 3, 517-611.

Piestrzynski, A., Wendorff, M., Letsholo, M., and Mackay, W. (2015) Platinum-group minerals in the Neoproterozoic stratabound copper-silver mineralization, the Kalahari Copperbelt, northwestern Botswana. South African Journal of Geology, 118, 275-284.

Raiswell, R., and Berner, R. A. (1985) Pyrite formation in euxinic and semi-euxinic sediments. American Journal of Science, 285, 710-724.

Ramokate, L.V., Mapeo, R.M.M., Corfu, F., and Kampunzu, A.B. (2000) Proterozoic geology and regional correlation of the Ghanzi-Makunda area, western Botswana. Journal of African Earth Science, 30, 453–466.

Ruxton, P.A. (1986) Sedimentology, isotopic signature and ore genesis of the Klein Aub copper mine, South West Africa/Namibia, in: Anhaeusser, C.A., and Maske, S., (Eds.), Mineral deposits of Southern Africa. Geological Society of South Africa, 2, 1725-1738.

Ruxton, P.A., and Clemmey, H. (1986) Late Proterozoic stratabound red bed-copper deposits of the Witvlei area, South West Africa/Namibia, in Anhaeusser C.A., and Maske, S., eds., Mineral deposits of southern Africa. Geological Society of South Africa, 2, 1739-1754.

Schieber, J. (1989) Pyrite mineralization in microbial mats from the mid-Proterozoic Newland Formation, Belt Supergroup, Montana, U.S.A. Sedimenatry Geology, 64,79-90.

Schwartz, M.O., Akanyang, P., Trippler, K., and Ngwisanyi, T.H. (1995) The Sediment hosted Ngwako Pan Copper Deposit, Botswana. Economic Geology, 90, 1118-1147.

Schwartz, M.O., Kwok, Y.Y., Davis, D.W., and Akanyang, P. (1996) Geology, geochronology, and regional correlations of the Ghanzi Ridge, Botswana: *South African Journal of Geology*, 99, 245-250.

Selley, D., Scott, R., Emsbo, P., Koziy, L., Hitzman, M.W., Bull, S., Duffett, M., Sebagenzi, S., Halpin, J., and Broughton, D., 2018, Structural configuration of the Central African Copperbelt: Roles of evaporites in structural evolution, basin hydrology, and ore location, in Arribas R., A.M., and Mauk, J.L., eds., Metals, Minerals, and Society: Society of Economic Geologists Special Publication 21, p. 115–156.

Sharp, Z. D., and Kirscher, D. L. (1994) Quartz-calcite oxygen isotope thermometry: A calibration based on natural isotopic variations. Geochimica et Cosmochimica Acta, 58, 4491-4501

Shephard, G., Jenkin, G., and Catterall, D. (2014) Origin and fluid sources of Kalahari Copperbelt mineralization, Botswana: an in-depth study of Zone 5 and 6 of the Khoemacau copper-silver exploration project. Unpublished MGeol. Thesis, University of Leicester, Leicester, United Kingdom.

Sillitoe, R.H. 2010. Porphyry Copper Systems. Economic Geology, 105, 3-41.

Sillitoe, R.H., Perello, J., and Garcia, A (2010) Sulphide-bearing veinlets throughout the stratiform mineralisation of the Central African Copperbelt: temporal and genetic implications. *Economic Geology*, 105, 1361-1368.

Singer, D.A. 2017. Future copper resources. Ore Geology Reviews, 86, 271-279.

Sweeney, M.A. (1987) The use of fluid inclusion geochemistry in determining the origin of veins, examples from the Zambian Copper-belt. Journal of Geological Society of Zambia 1, 18–28.

U.S. Steel. (1972-1978) Monthly and quarterly reports on prospecting activities in the Zeta and Theta concessions, southern Ngamiland: Lobatse, Botswana Geological Survey, Unpublished report.

Van der Heever, D., Arengi, J., and van Rensberg, J. (2009) Technical report, Ghanzi copper-silver project, Ghanzi District, Botswana. GeoLogix Technical Report for Hana Mining Ltd.

Walsh, A.M., Jenkin, G.R.T., Catterall, D., and Boyce, A.J. (2014) Origin and fluid sources of Kalahari Copperbelt mineralisation, Botswana: Regional variations in mineralogy, isotopic signatures and fluid characteristics at the Khoemacau Cu-Ag Project. Unpublished MGeol. Thesis, University of Leicester, Leicester, United Kingdom.

Wilkinson, J.J., Chang, Z., Cooke, D.R., Baker, M.J., Wilkinson, C.C., Inglis, S., Chen, H. & Bruce Gemmell, J. (2015) The chlorite proximitor: A new tool for detecting porphyry ore deposits. Journal of Geochemical Exploration, 152, 10-26

Yanagisawa, F., and Sakai, H. (1983) Thermal decomposition of barium sulfate-vanadium-pentoxide-silica glass mixtures for preparation of sulfur dioxide in sulfur isotope ratio measurements. *Analytical Chemistry*, 55, 985–987.

Akita University

Location of the Zone 5 copper deposit/Mine

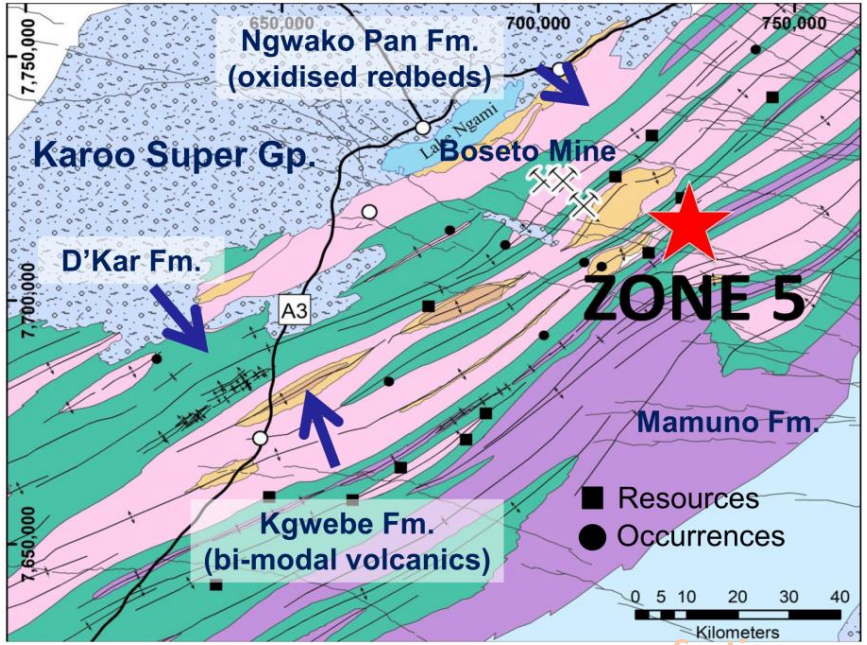

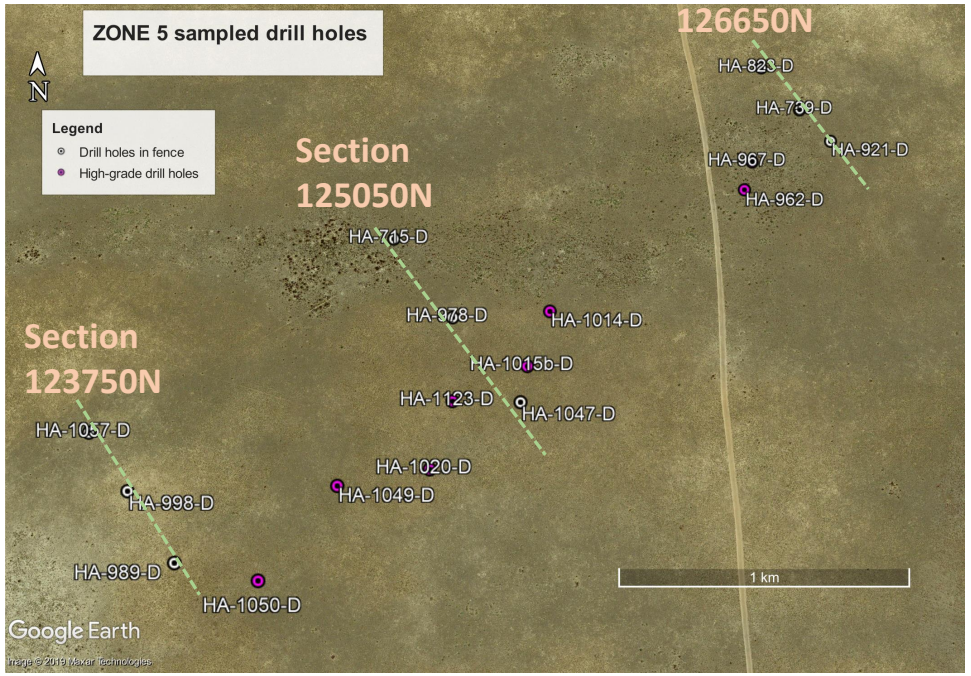

APPENDIX A

Mpho's field notes 2019/February-April

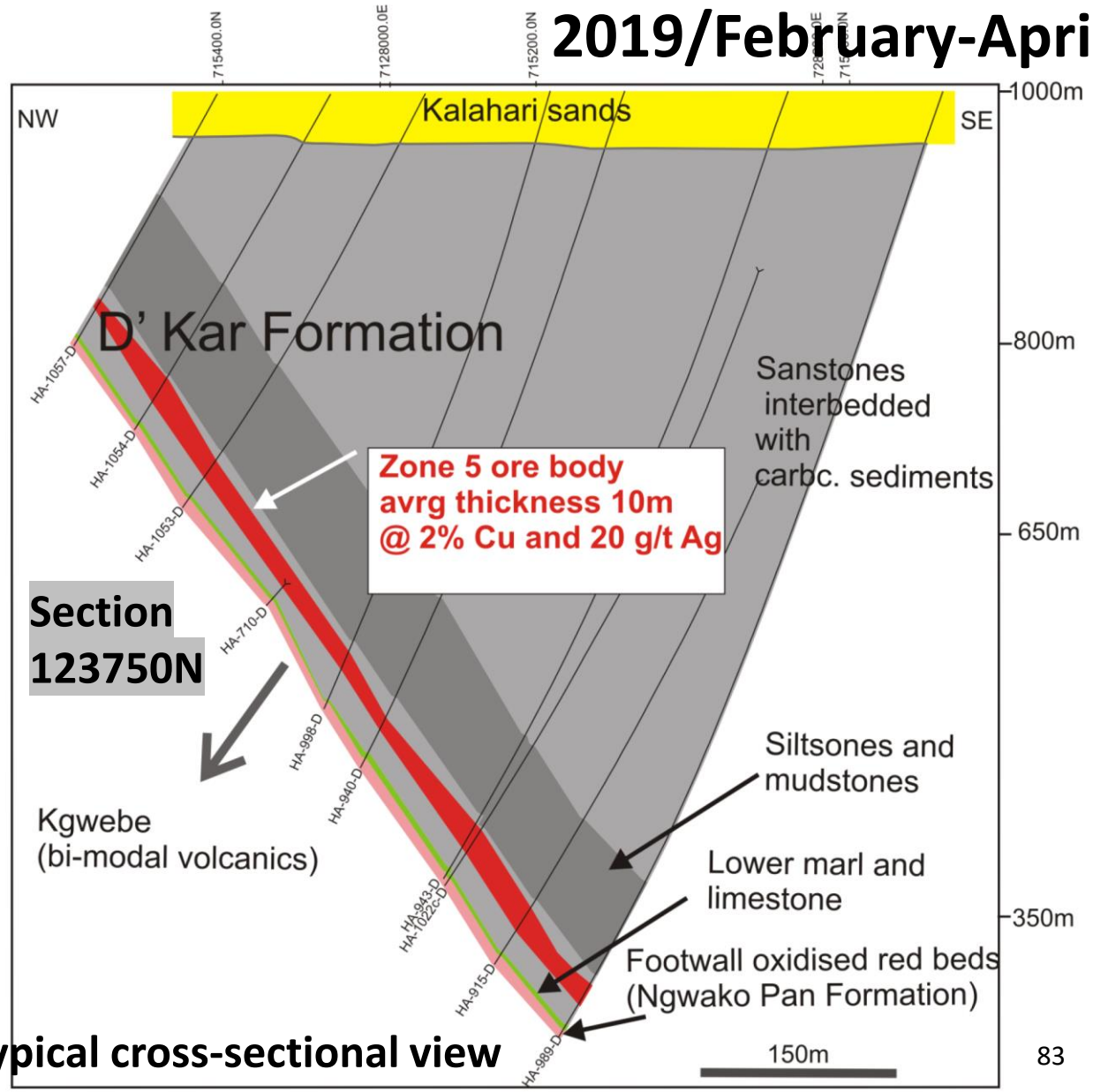

Typical cross-sectional view

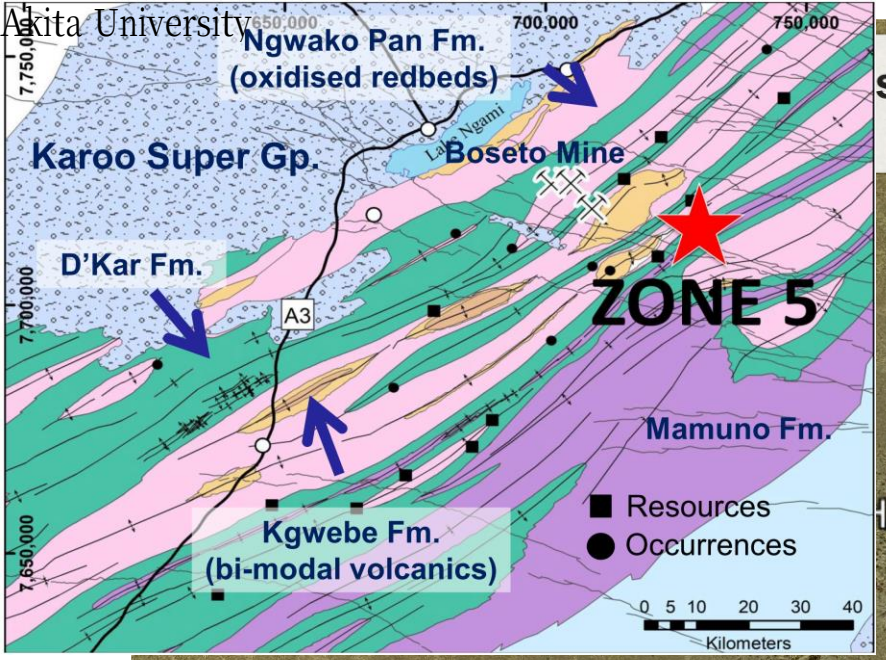

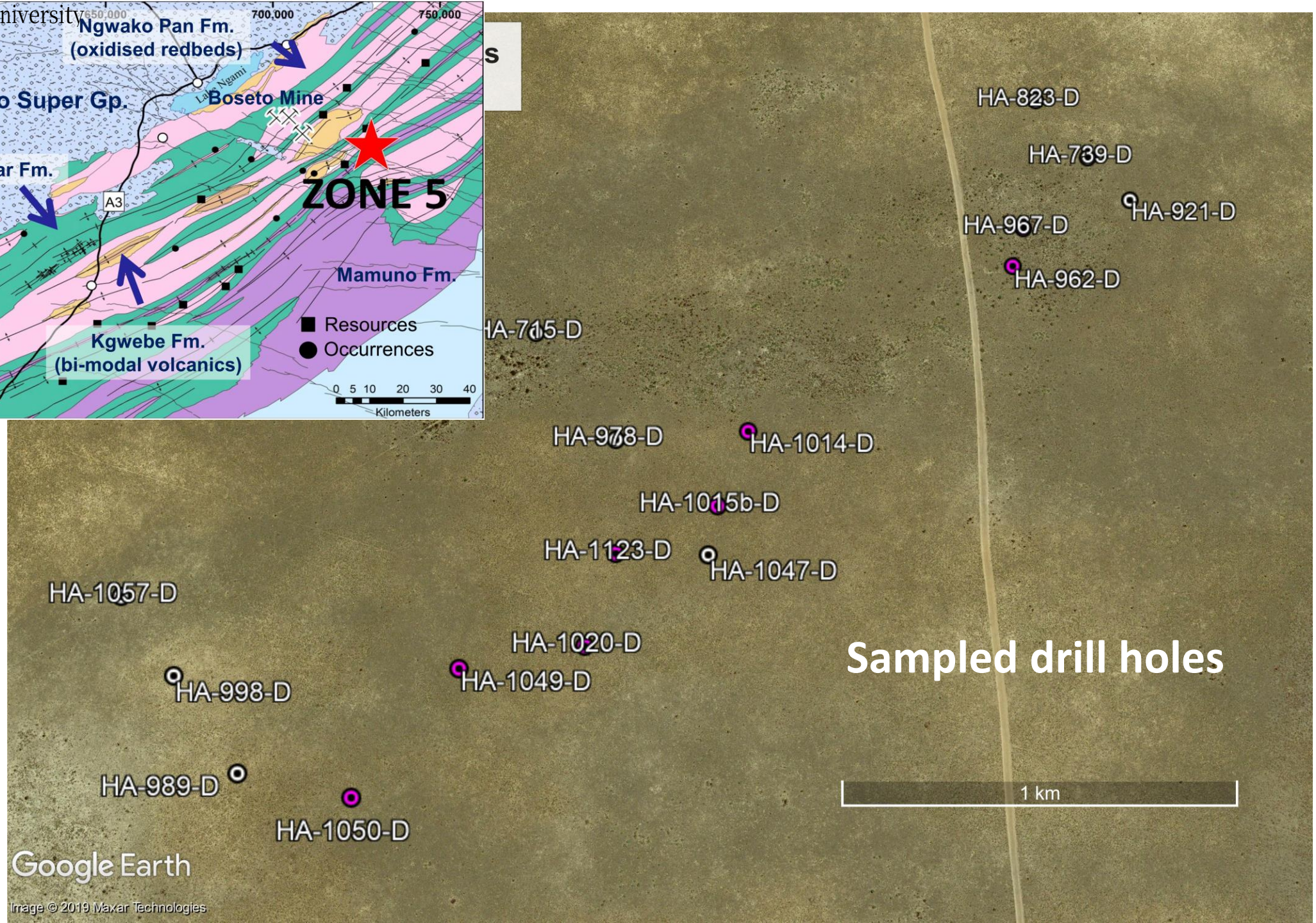

Sampled drill holes

Zone 5	HA-1123-D	808.00	808.68	19.3	4.9	2.2	2.0	37	0.0	109
Zone 5	HA-1123-D	808.68	809.00	16.1	16.6	1.0	1.2	5	0.0	66
Zone 5	HA-1123-D	809.00	809.92	23.9	8.0	1.0	3.1	133	0.0	108
Zone 5	HA-1123-D	809.92	810.27	73.8	23.1	1.0	12.4	1237	0.0	173
Zone 5	HA-1123-D	810.27	810.60	54.9	2.9	1.5	5.2	27	0.0	155
Zone 5	HA-1123-D	810.60	810.92	201.4	7.7	1.0	15.1	14	0.0	241
Zone 5	HA-1123-D	810.92	810.92	0.6	0.4	1.0	0.6	5	0.0	27
Zone 5	HA-1123-D	810.92	811.42	19.9	3.3	2.5	1.8	36	0.0	124
Zone 5	HA-1123-D	811.42	812.02	35.6	1.9	2.1	3.6	53	0.0	129
Zone 5	HA-1123-D	812.02	812.36	30.0	6.6	1.0	4.5	21	0.0	133

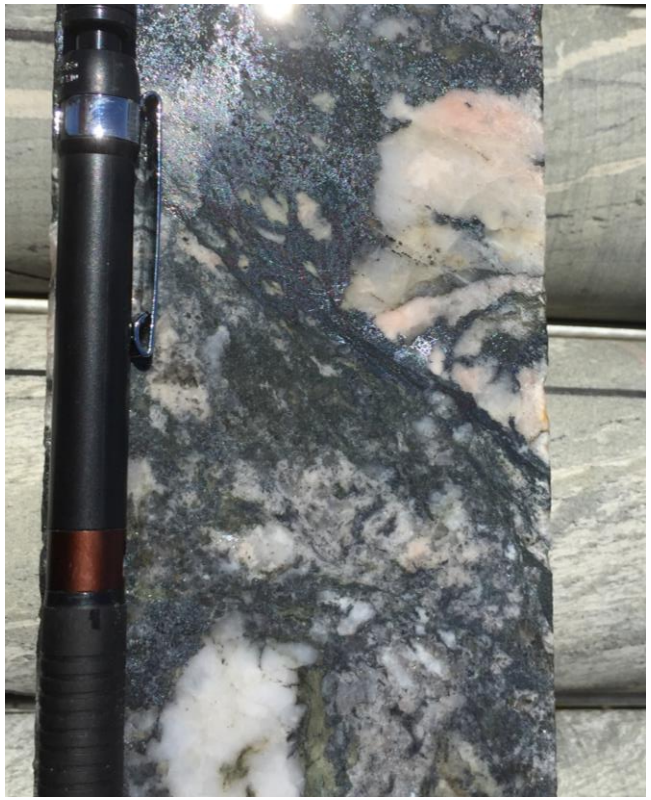

HA-1123-D,
810.6 -810.9; 15.1% Cu, 201.4ppm Ag
Quartz-calcite-bornite-chalcocite vein

HA-1123-D, 809.92-810.27; 12.4% Cu, 73.8ppm Ag
Quartz-calcite-bornite-chalcocite vein

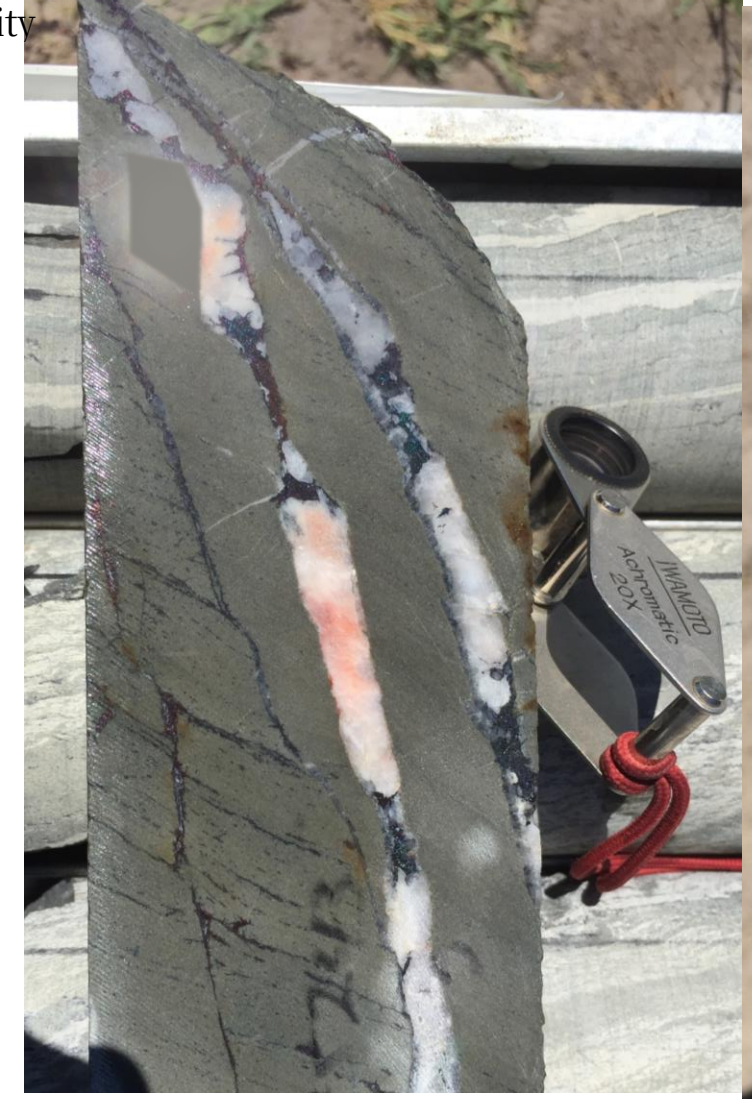

Zone 5	HA-1123-D	810.27	810.60	54.9	2.9	1.5	5.2	27	0.0	155
Zone 5	HA-1123-D	810.60	810.92	201.4	7.7	1.0	15.1	14	0.0	241
Zone 5	HA-1123-D	810.92	810.92	0.6	0.4	1.0	0.6	5	0.0	27
Zone 5	HA-1123-D	810.92	811.42	19.9	3.3	2.5	1.8	36	0.0	124
Zone 5	HA-1123-D	811.42	812.02	35.6	1.9	2.1	3.6		0.0	129
Zone 5	HA-1123-D	812.02	812.36	30.0	6.6	1.0	4.5	21	0.0	133

HA-1123-D, 811.42 -812.02; 3.6% Cu, 35.6ppm Ag

Calcite-quartz-bornite-chalcocite vein

Also copper ore impregnating the rock along bedding and foliation planes

HA-1123-D,
Folded calcite-quartz-bornite-chalcocite vein

Hole_ID	From_	To_	Ag_ppm	Ca_pct	Cd_ppm	Cu %	Mo_ppm	Pb %	Zn_ppm
HA-1129-D	853.00	854.00	0.3	0.9	1.0	0.0	2	0.0	208
HA-1129-D	854.00	854.66	0.3	0.9	1.0	0.0	1	0.0	62
HA-1129-D	854.66	855.16	2.9	20.8	10.9	1.0	4	0.4	1998
HA-1129-D	854.66	855.16	2.8	21.5	9.5	1.1	3	0.4	1967
HA-1129-D	855.16	855.52	1.3	19.3	5.8	0.0	3	0.3	1394
HA-1129-D	855.52	856.30	0.3	4.4	7.6	0.0	6	0.1	1696
HA-1129-D	856.30	857.06	0.3	3.2	7.9	0.0	3	0.1	1578

Hole_ID	From_	To_	Ag_ppm	Ca_pct	Cd_ppm	Cu %	Mo_ppm
HA-1129-D	873.55	874.28	4.7	28.1	2.2	0.4	3
HA-1129-D	874.28	874.62	52.9	18.2	2.5	7.1	293
HA-1129-D	874.62	875.39	8.0	22.6	2.0	0.6	2
HA-1129-D	875.39	876.05	20.2	17.2	2.7	1.7	1
HA-1129-D	876.05	876.70	94.4	23.4	2.2	6.9	1
HA-1129-D	876.70	877.32	7.4	9.4	2.5	0.6	2
HA-1129-D	877.32	877.84	3.0	24.6	2.0	0.3	1

HA-1129-D, 854.66-855.16; 1.1% Cu, 2.8ppm Ag
Calcite-quartz-chalcopyrite vein

HA-1129-D, 876.05-876.7; 6.9% Cu, 94.4ppm Ag
Calcite-quartz-bornite vein

HA-967-D	61308/D	545.58	546.23		7.233	68
HA-967-D	61309/D	546.23	547		3.511	23.33
HA-967-D	61310/D	547	547		0.039	5.48

Late vein

HA-967-D; 545.58-546.23; 7.2% Cu, 68 ppm Ag
Primarily foliation parallel vein hosted bn ±cc. Intensely sheared and mineralization is concentrated along porous zones. Late quatz-calcite vien oblique to main fabric.

HA-967-D	61311/D	547	548		2.744	20.19
HA-967-D	61312/D	548	548.78		2.549	17.59
HA-967-D	61313/D	548.78	549.55		7.111	44.6

HA-967-D; 548.78-549.55; 7.1 % Cu, 44.6 ppm Ag
Discordant quartz-calcite vein with interstitial bn ± cc mineralization

HA-967-D	61320/D	554	554.3		2.948	20.79
HA-967-D	61321/D	554.3	555		2.753	25.57
HA-967-D	61322/D	555	556		3.341	40.83

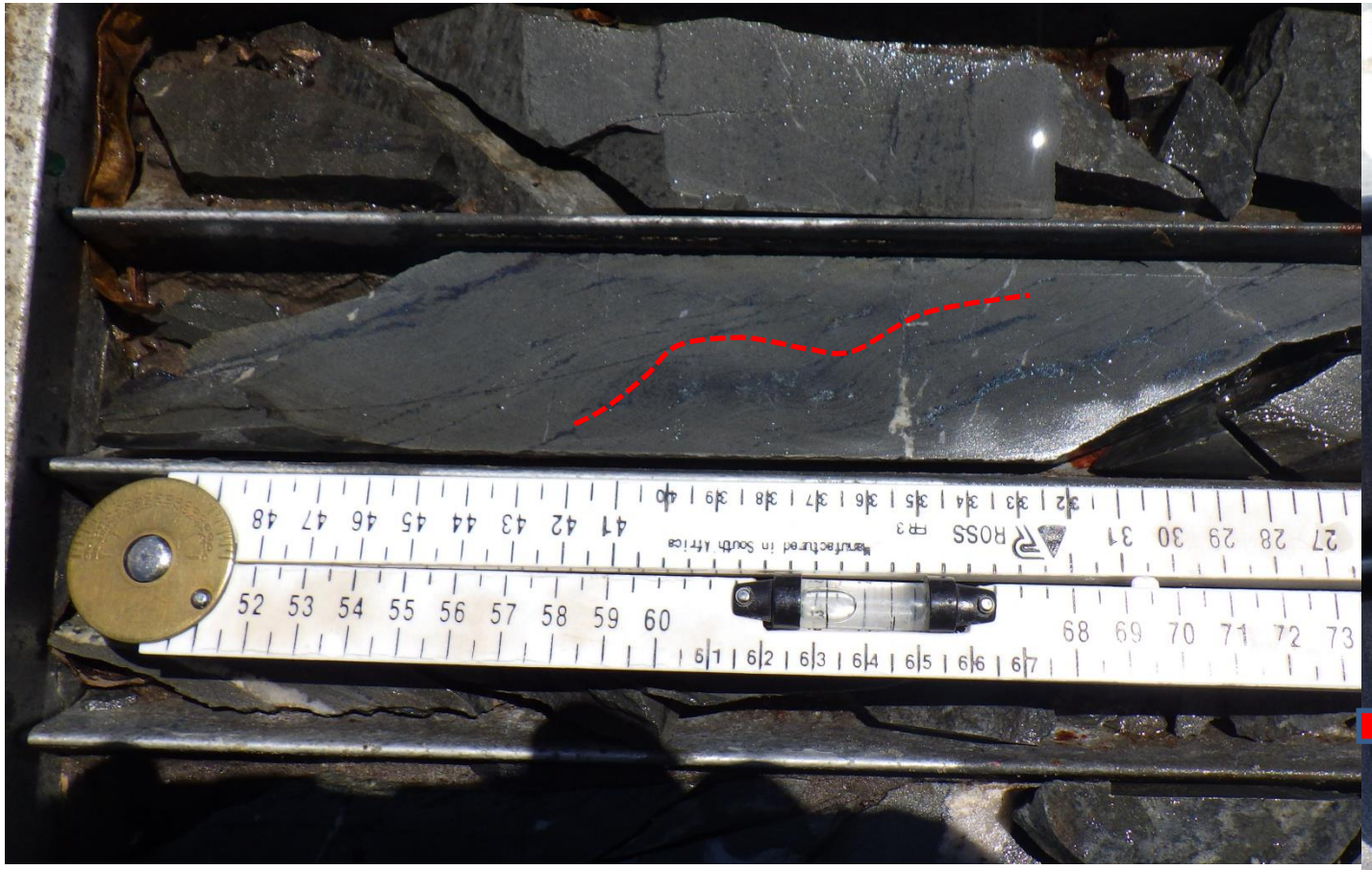

HA-967-D; 555-556; 3% Cu, 40.83 ppm Ag
Fine cleavage hosted bn ± cc mineralization which is also rotated. Cu ore from the vein is impregnating the rock along the cleavage planes

HA-967-D	61324/D	556.77	557.17		2.366	22.76
HA-967-D	61325/D	557.17	558.04		2.467	30.04
HA-967-D	61326/D	558.04	559		2.462	31.23
HA-967-D	61327/D	559	559.66		2.709	35.46

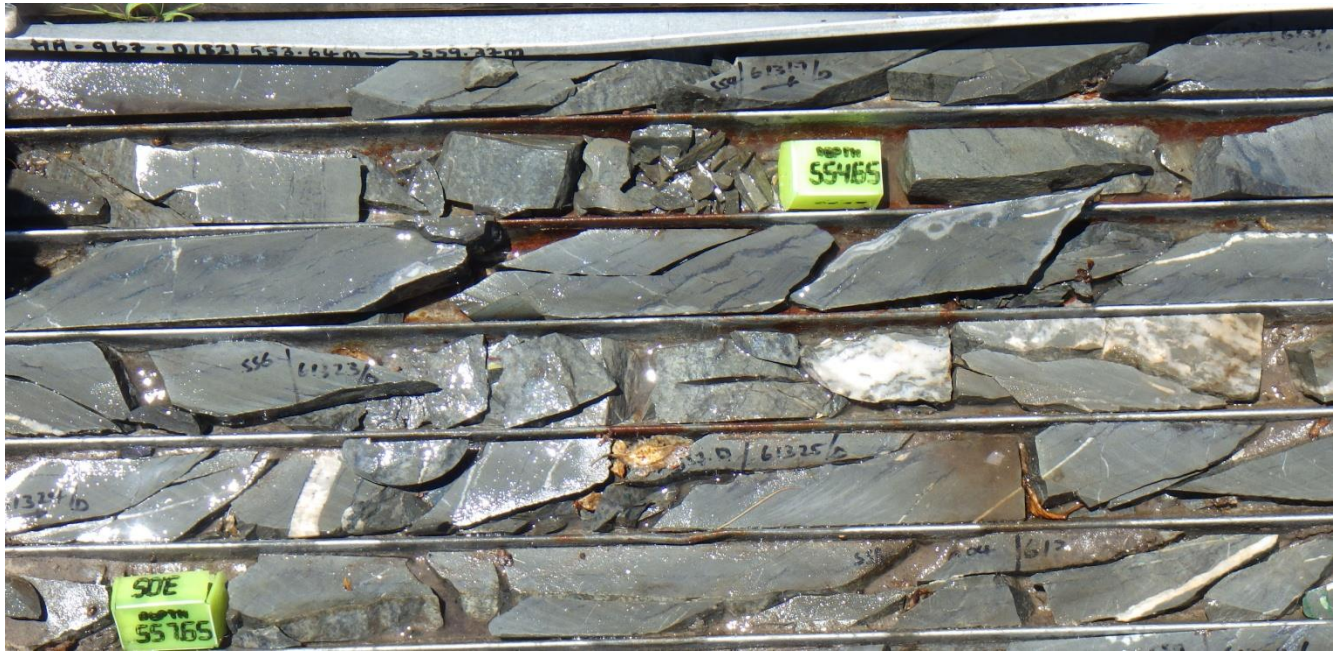

HA-967-D; 557.17-5598.04; 2.5% Cu, 30ppm Ag
Vein-hosted fine bn mineralization, prominent is the crackle breccia pattern with veins filled by bn

HA-1050-[	67417/D	1134.34	1135.23		1.809	24.2
HA-1050-[	67418/D	1135.23	1135.64		4.79	53.1
HA-1050-[	67419/D	1135.64	1136.29		1.227	14.5
HA-1050-[	67420/D	1136.29	1136.29		0.639	63.3

HA-1050-D; 1134.34-1135.23; 1.8% Cu, 24.2 ppm Ag
Vein-hosted bn mineralization, noticeable is the slight rotation of the veins together with mineralization-foliation parallel

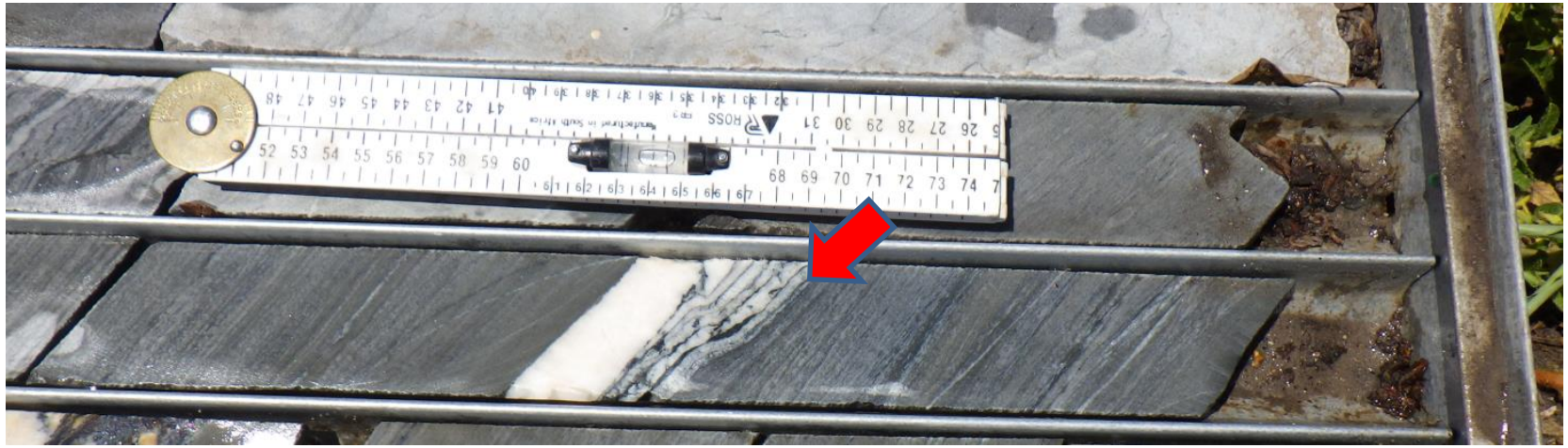

HA-1050-D	67417/D	1134.34	1135.23		1.809	24.2
HA-1050-D	67418/D	1135.23	1135.64		4.79	53.1
HA-1050-D	67419/D	1135.64	1136.29		1.227	14.5
HA-1050-D	67420/D	1136.29	1136.29		0.639	63.3

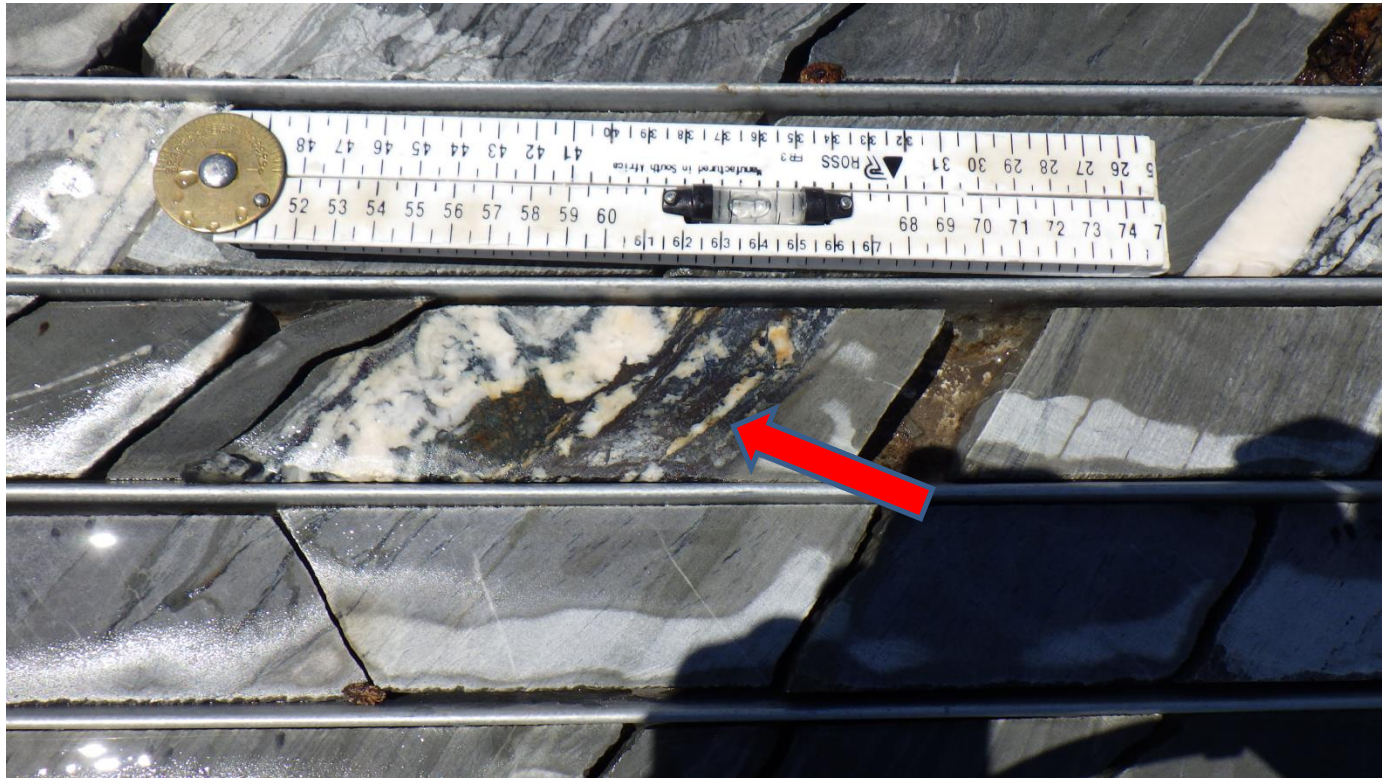

HA-1050-D, 1135.23-1135.64; 4.75% Cu, 53.1ppm Ag
Qtz-cal- bn ± cc vein parallel to cleavage

HA-1050-D	67429/D	1142.29	1142.63		5.846	164.1
HA-1050-D	67430/D	1142.29	1142.63		5.872	147
HA-1050-D	67431/D	1142.63	1143.55		0.715	11.3
HA-1050-D	67432/D	1143.55	1144		0.918	20.2
HA-1050-D	67433/D	1144	1145		2.732	35.6
HA-1050-D	67434/D	1145	1145.95		2.173	31.1
HA-1050-D	67435/D	1145.95	1146.82		2.891	36.5

HA-1050-D, 1142.29-1142.63; 5.8% Cu, 164.1ppm Ag
Sheared vein-hosted bn ± cc (along planes of weakness and porous zones) mineralization and veining if foliation parallel

HA-1050-[	67429/D	1142.29	1142.63		5.846	164.1
HA-1050-[	67430/D	1142.29	1142.63		5.872	147
HA-1050-[	67431/D	1142.63	1143.55		0.715	11.3
HA-1050-[	67432/D	1143.55	1144		0.918	20.2
HA-1050-[	67433/D	1144	1145		2.732	35.6
HA-1050-[	67434/D	1145	1145.95		2.173	31.1
HA-1050-[	67435/D	1145.95	1146.82		2.891	36.5

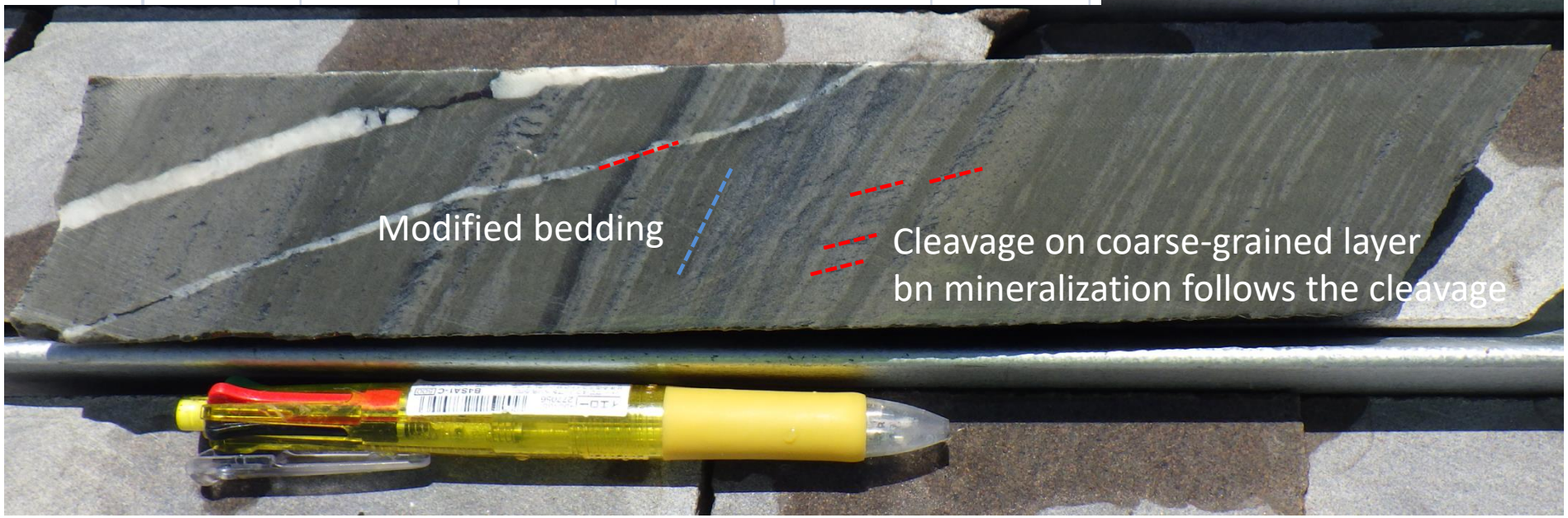

HA-1050-D; 1144-1145; 2.7% Cu, 35.6ppm Ag
Both vein-hosted and cleavage (S2)-hosted bn mineralization
Example of incipient bedding/foliation oblique shearing accompanied by veining

HA-962-D	61125/D	596.84	597.48		4.043	31.04
HA-962-D	61126/D	597.48	597.83		4.393	36.46
HA-962-D	61127/D	597.83	598.31		7.051	52.35
HA-962-D	61128/D	598.31	599		3.966	29.88

HA-962-D, 596.84-597.48; 4% Cu, 31ppm Ag
Mineralization in the fabric and cleavage, deformed by last calcite dominate veins
Bn around py grains

HA-962-D	61144/D	610.24	610.74		10.958	97.35
HA-962-D	61145/D	610.74	611.31		3.712	37.13
HA-962-D	61146/D	611.31	612		3.862	41.22
HA-962-D	61147/D	612	613		3.994	41.56
HA-962-D	61148/D	613	614		3.691	37.38

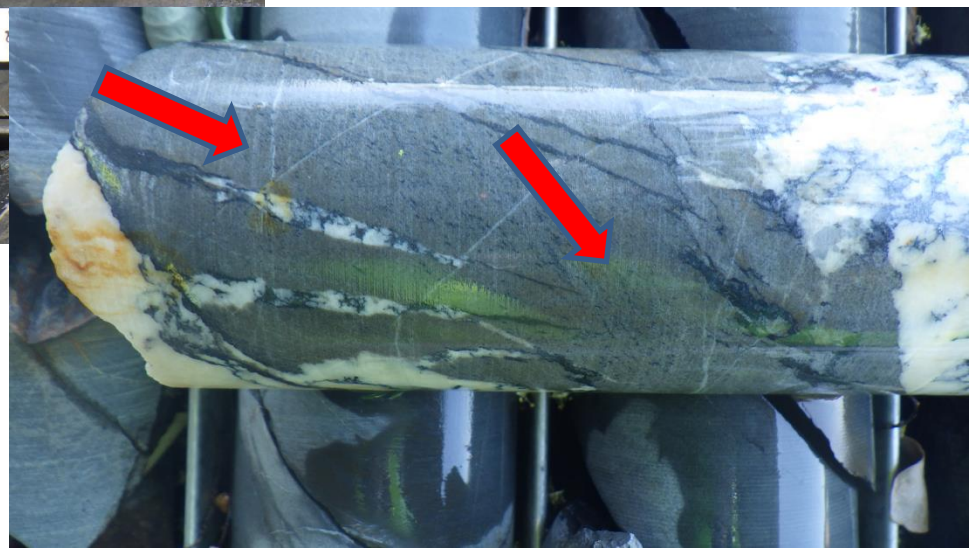

HA-962-D, 610.24-610.74; 11% Cu, 97ppm Ag
Mineralization in numerous veins and vein shears distributed through fabric and cleavage
Mineralization re-mobilized during deformation

HA-962-D	61144/D	610.24	610.74		10.958	97.35
HA-962-D	61145/D	610.74	611.31		3.712	37.13
HA-962-D	61146/D	611.31	612		3.862	41.22
HA-962-D	61147/D	612	613		3.994	41.56
HA-962-D	61148/D	613	614		3.691	37.38

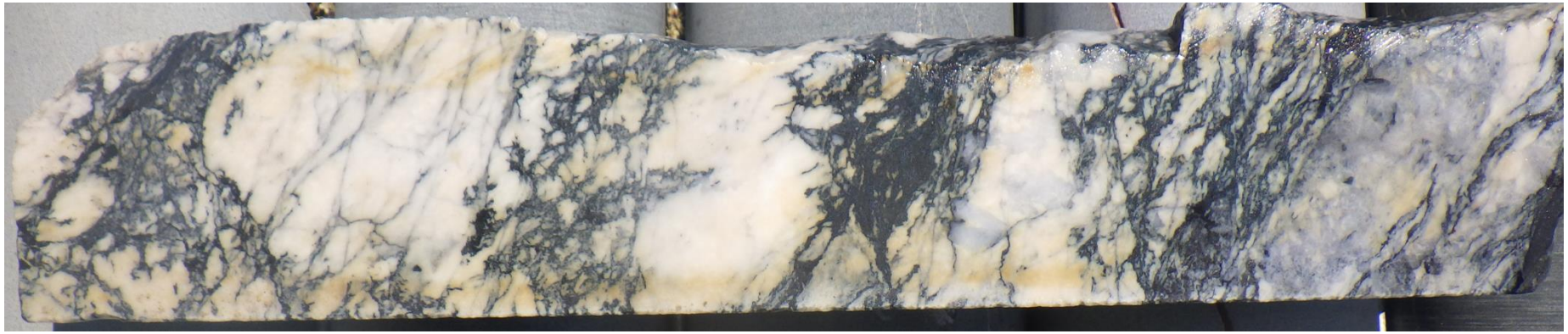

HA-962-D, 611.31-612; 4% Cu, 41.2ppm Ag
Mineralization in numerous veins and vein shears distributed through fabric and cleavage-bn occurs interstitially within porous domains

HA-1015b-D	66064/D	845.06	845.79		1.461	11.34
HA-1015b-D	66065/D	845.79	846.69		1.601	15.22
HA-1015b-D	66066/D	846.69	847.39		1.53	15.19
HA-1015b-D	66067/D	847.39	848.38		1.736	17.18
HA-1015b-D	66068/D	848.38	849.33		3.557	33.29
HA-1015b-D	66069/D	849.33	849.94		2.44	24.11

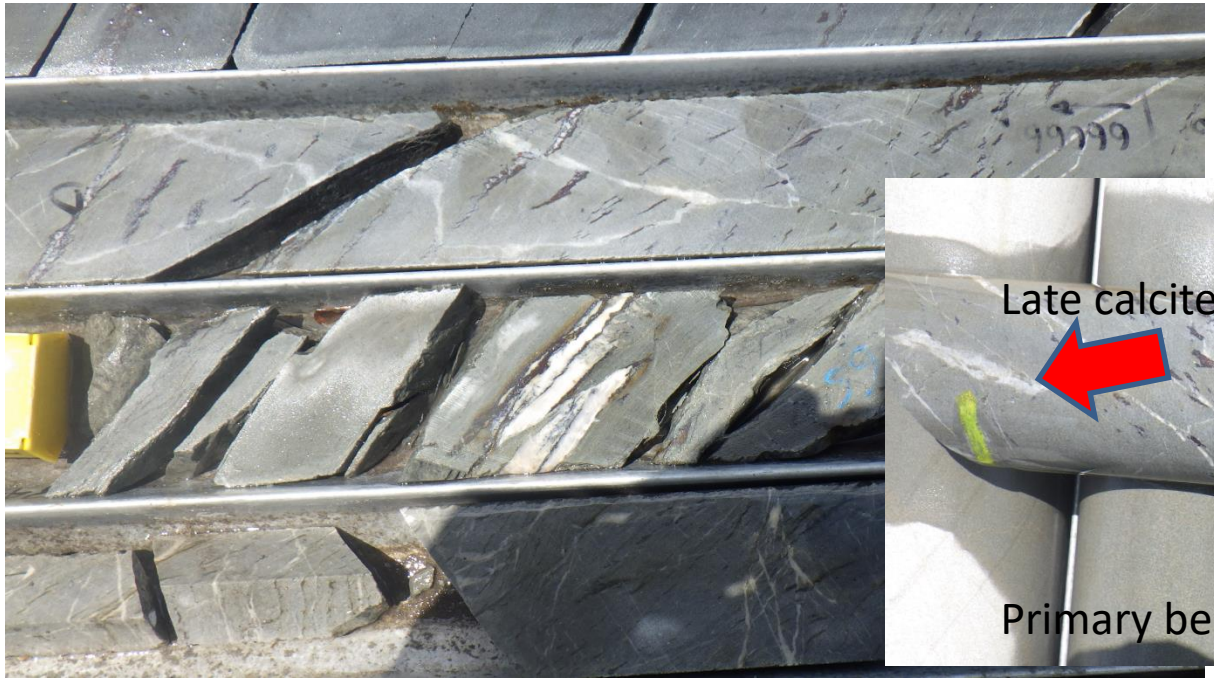

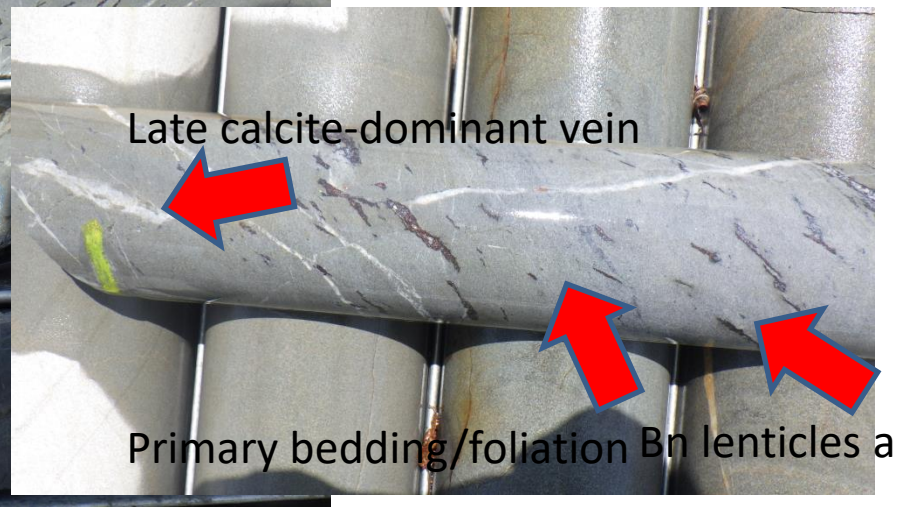

HA-1015b-D, 846.69-847.39; 1.53% Cu, 15.19ppm Ag
Cleavage controlled bn mineralization. It appears the mineralization was
Re-mobilized during shearing and follows subsequent cleavage planes

HA-1015b-D	66075/D	852.48	853.1		0.885	8.38
HA-1015b-D	66076/D	853.1	853.69		9.212	85.9
HA-1015b-D	66077/D	853.69	854.64		0.978	10.09
HA-1015b-D	66078/D	854.64	855.46		1.213	14.51

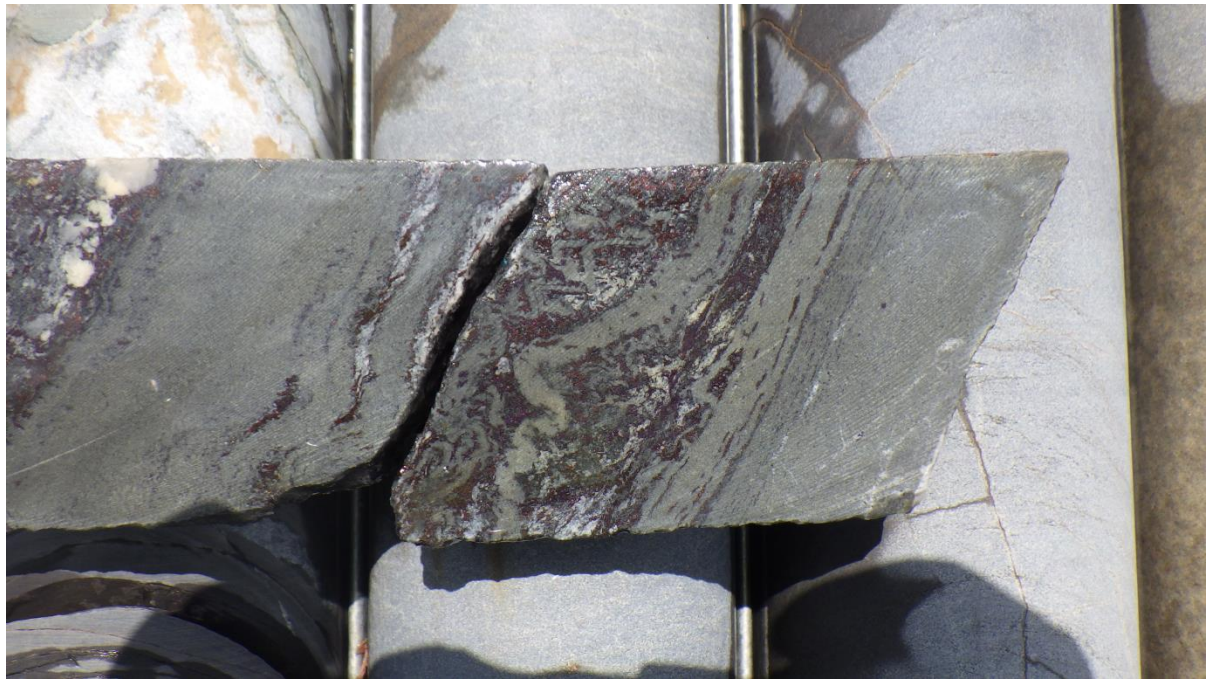

HA-1015b-D, 853.1-853.69; 9.2% Cu, 86ppm Ag
Foliation parallel bn mineralization. Noticeable is the subsequent folding of the fine silty layer

HA-1015b-D	66084/D	858.76	859.62		0.71	7.76
HA-1015b-D	66085/D	859.62	860.27		0.966	13.18
HA-1015b-D	66086/D	860.27	860.67		15.06	249.17
HA-1015b-D	66087/D	860.67	861.13		0.834	12.21

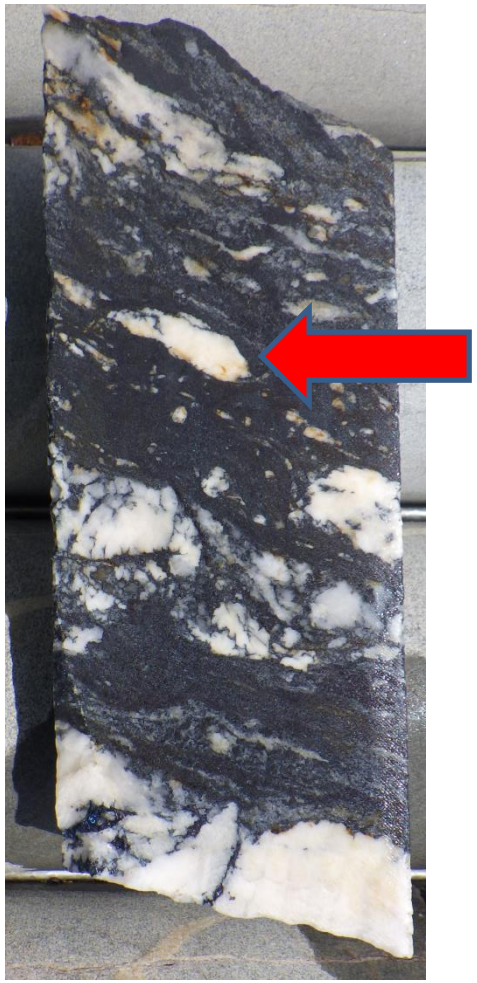

HA-1015b-D, 860.27-860.67; 15% Cu, 249ppm Ag
Shear quartz-calcite –bn/cc viens adjacent to laminated dirty limestone with noticeable boudinage and rotations as a result of shearing

HA-1014-D	64990/D	746.47	746.47		0.646	61.7
HA-1014-D	64991/D	746.47	746.88		8.974	103.22
HA-1014-D	64992/D	746.88	747.87		2.272	23.11
HA-1014-D	64993/D	747.87	748.25		1.841	19.71

HA-1014-D, 746.47-746.88, 9% Cu, 103ppm Ag
Brecciated quartz-calcite vein with interstitial bn

HA-1014-D	64998/D	751.67	752		10.49	83.21
HA-1014-D	64999/D	752	753		2.96	29.04
HA-1014-D	65000/D	752	753		3.058	30.3
HA-1014-D	65001/D	753	754		3.662	34.59

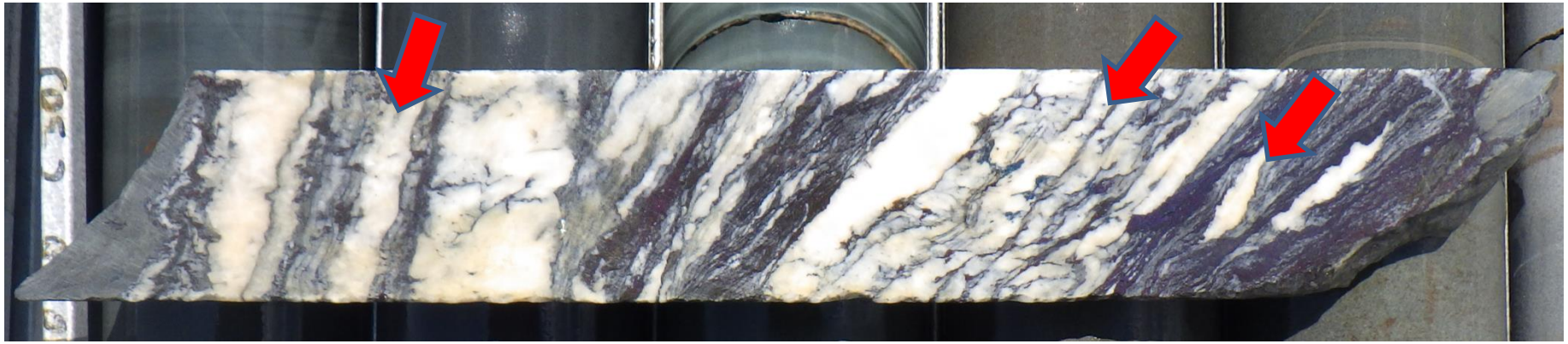

HA-1014-D, 751.67-752; 10.5% Cu, 83.2ppm Ag both low and high angle shear Quartz-calcite-bn vein. Essentially parallel to bedding

HA-1014-D	65019/D	766.52	766.94		6.7	84.5
HA-1014-D	65020/D	766.94	766.94		0.199	19.9
HA-1014-D	65021/D	766.94	767.47		7.294	150
HA-1014-D	65022/D	767.47	768.18		0.509	8.37

HA-1014-D, 766.52-766.94; 6.7% Cu, 84.5ppm
Ag Qtz-cal- bn ± cc vein

HA-1020-D	66452/D	1188	1188.68		2.464	23.7
HA-1020-D	66453/D	1188.68	1189.37		10.55	126.3
HA-1020-D	66454/D	1189.37	1190.18		0.859	8.9
HA-1020-D	66455/D	1190.18	1190.61		17.005	132.6
HA-1020-D	66456/D	1190.61	1191.5		2.205	24.7
HA-1020-D	66457/D	1191.5	1191.95		2.403	26.8
HA-1020-D	66458/D	1191.95	1192.95		1.507	15.2
HA-1020-D	66459/D	1192.95	1193.57		1.762	16
HA-1020-D	66460/D	1193.57	1193.57		0.648	60.4
HA-1020-D	66461/D	1193.57	1194.29		8.228	68.4

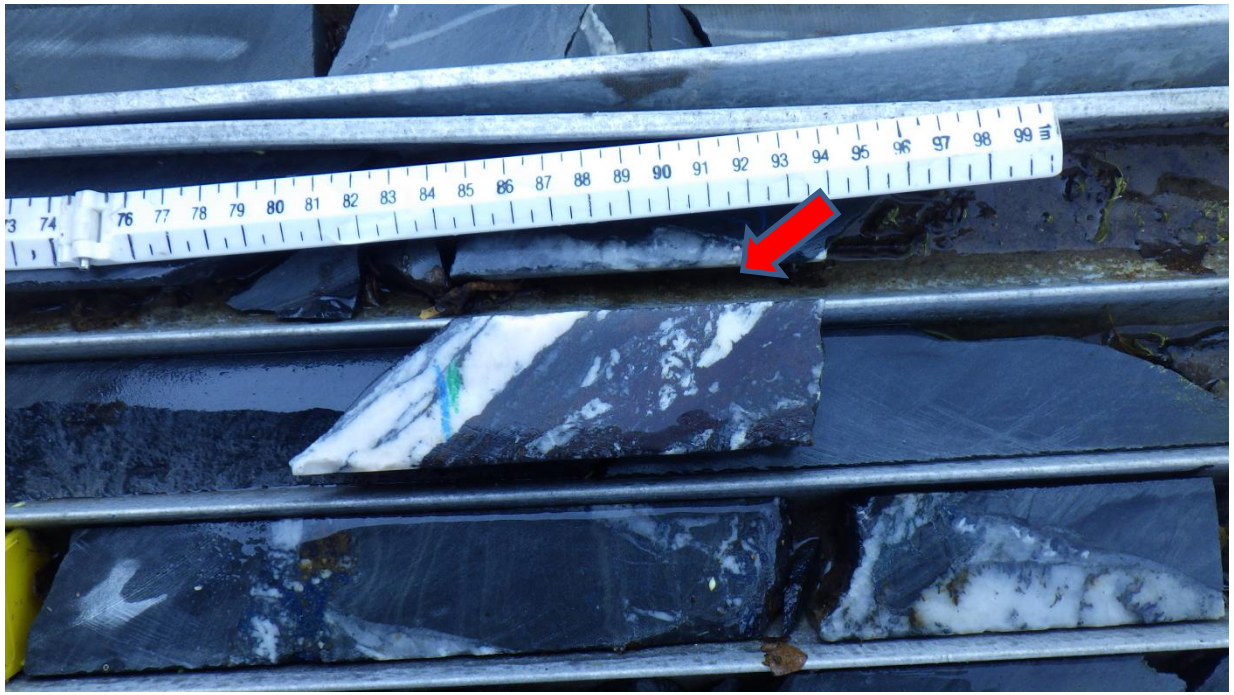

HA-1020-D, 1188.68-1189.37; 10.55% Cu, 126.3ppm Ag
Richly mineralized quartz-calc- bn ± cc

HA-1020-D	66452/D	1188	1188.68		2.464	23.7
HA-1020-D	66453/D	1188.68	1189.37		10.55	126.3
HA-1020-D	66454/D	1189.37	1190.18		0.859	8.9
HA-1020-D	66455/D	1190.18	1190.61		17.005	132.6
HA-1020-D	66456/D	1190.61	1191.5		2.205	24.7
HA-1020-D	66457/D	1191.5	1191.95		2.403	26.8
HA-1020-D	66458/D	1191.95	1192.95		1.507	15.2
HA-1020-D	66459/D	1192.95	1193.57		1.762	16
HA-1020-D	66460/D	1193.57	1193.57		0.648	60.4
HA-1020-D	66461/D	1193.57	1194.29		8.228	68.4

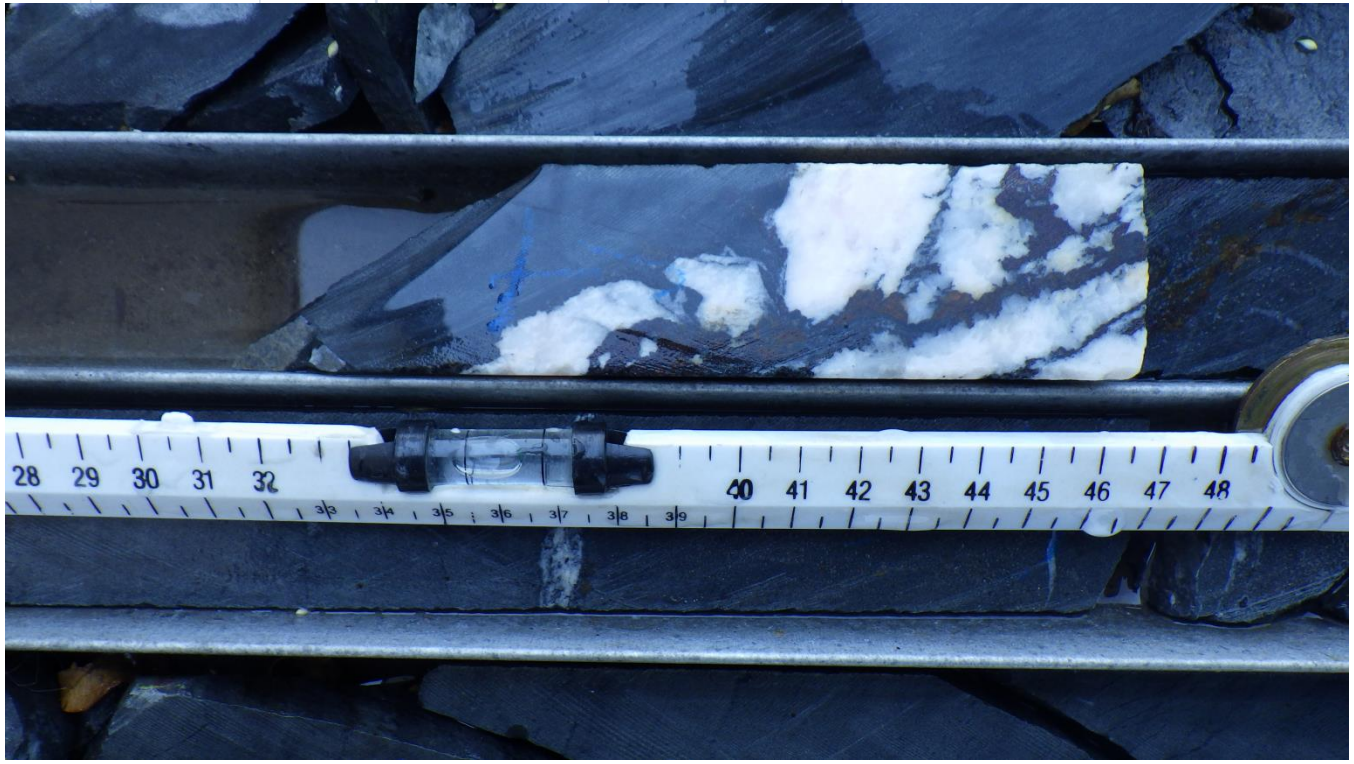

HA-1020-D, 1190.18-1190.61; 17% Cu, 132.6ppm Ag
quartz-calc- bn ± cc

HA-1020-D	66452/D	1188	1188.68		2.464	23.7
HA-1020-D	66453/D	1188.68	1189.37		10.55	126.3
HA-1020-D	66454/D	1189.37	1190.18		0.859	8.9
HA-1020-D	66455/D	1190.18	1190.61		17.005	132.6
HA-1020-D	66456/D	1190.61	1191.5		2.205	24.7
HA-1020-D	66457/D	1191.5	1191.95		2.403	26.8
HA-1020-D	66458/D	1191.95	1192.95		1.507	15.2
HA-1020-D	66459/D	1192.95	1193.57		1.762	16
HA-1020-D	66460/D	1193.57	1193.57		0.648	60.4
HA-1020-D	66461/D	1193.57	1194.29		8.228	68.4

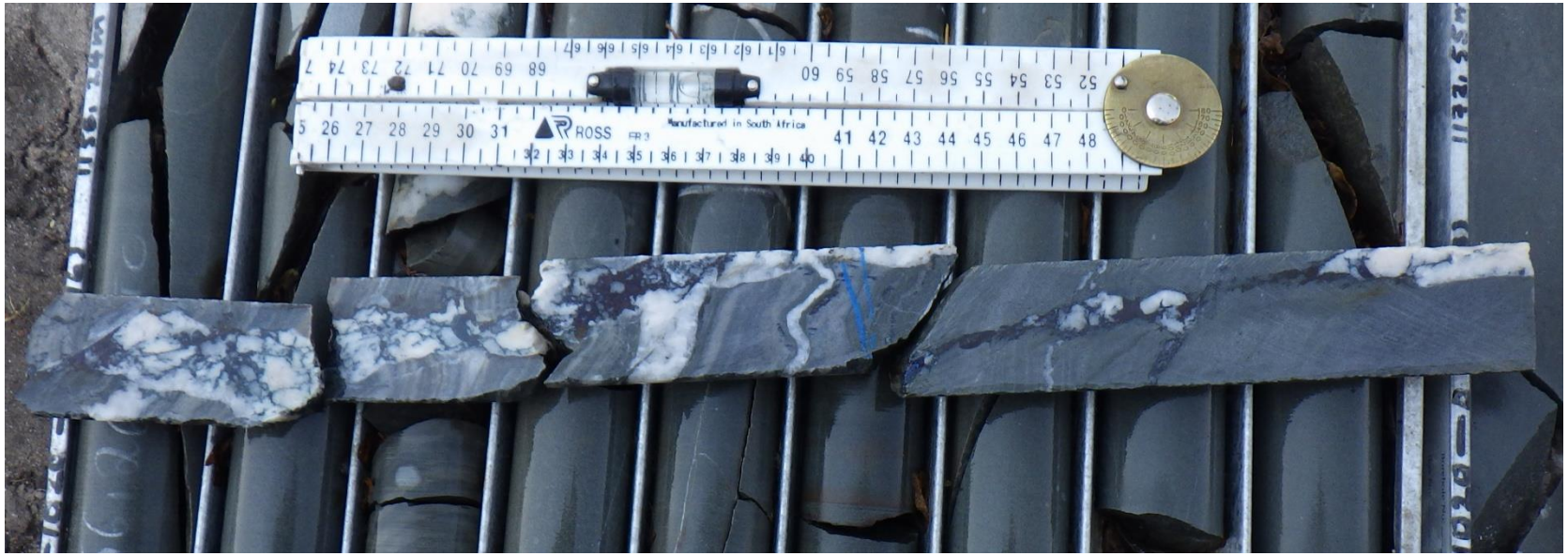

HA-1020-D, 1193.57-1194.29; 8.2% Cu, 68.4ppm Ag
High angle quartz-calc- bn ± cc cutting across bedding, in the process
Impregnating veinlets along bedding

HA-1020-D	66467/D	1198.78	1199.17		4.807	53.3
HA-1020-D	66468/D	1199.17	1200		10.961	146.8
HA-1020-D	66469/D	1200	1200.5		16.843	243
HA-1020-D	66470/D	1200	1200.5		16.092	229.5
HA-1020-D	66471/D	1200.5	1201.23		10.77	160.5

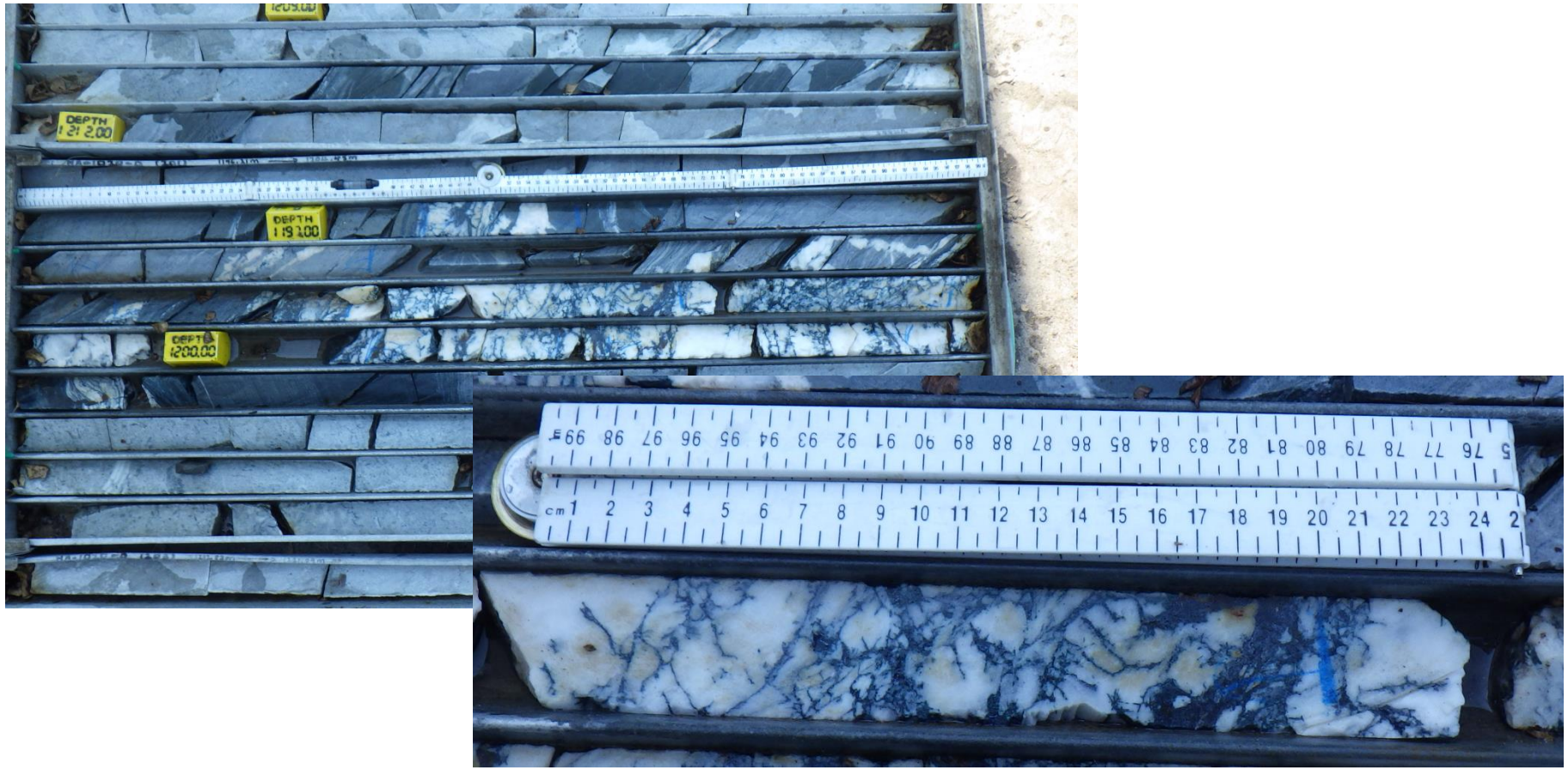

HA-1020-D, 1199.17-1200; 11% Cu, 147ppm Ag
Discordant quartz-calc- bn ± cc vein

HA-1049-D	67256/D	1102.42	1103.18		0.564	6.6
HA-1049-D	67257/D	1103.18	1104		5.601	58.8
HA-1049-D	67258/D	1104	1104.55		9.22	88.9
HA-1049-D	67259/D	1104.55	1105.02		17.29	218.5

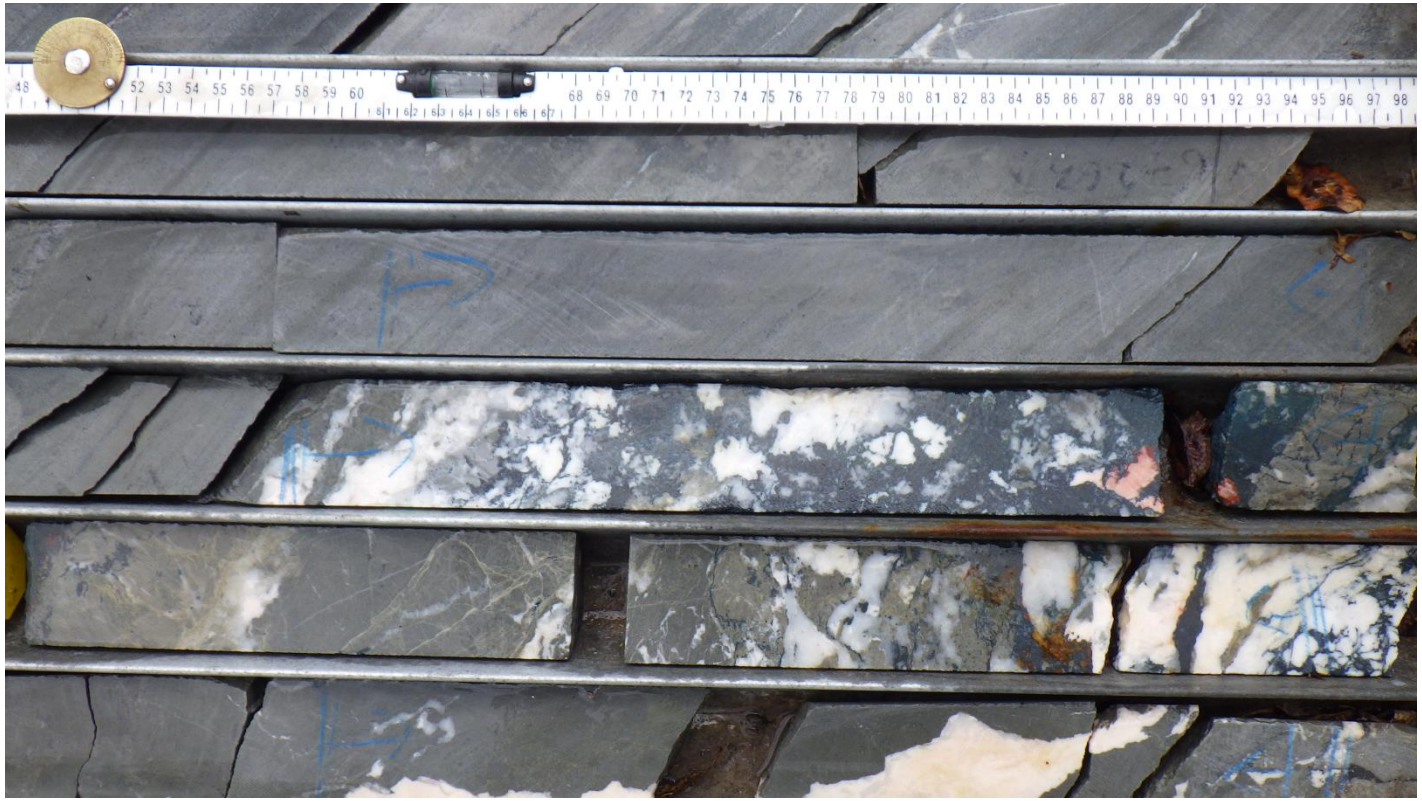

HA-1049-D, 1104-1104.55; 9.22% Cu, 88 ppm Ag
1104.55-1105.2; 17.29% Cu, 218.5ppm Ag
quartz-calc- bn ± cc vein

APPENDIX B
MINERAL CHEMISTRY DATA

	Detection limit (ppm)	111	152	195	346	87	101	47	189	230	76	157	
No.	**Mineral**	**Fe**	**Cu**	**Zn**	**As**	**Co**	**Ni**	**S**	**Pb**	**Bi**	**Ag**	**Sb**	**Total**
7	Chalcocite	0.12	77.95	0.04	0.07	0.01	–	20.55	–	0.041	0.025	0.00	99
14	Chalcocite	0.02	79.91	0.01	0.02	0.01	–	20.71	–	0.039	0.207	0.02	101
17	Chalcocite	0.12	79.84	0.07			–	20.65	–	0.005	0.233	–	101
27	Chalcocite	0.00	79.56	0.05	0.04	0.01	–	20.23	–	0.016	0.422	–	100
28	Chalcocite	0.01	79.80	0.04	0.03		–	20.08	–	0	0.461	–	100
29	Chalcocite	–	80.43	0.07	0.08		–	20.11	–	0	0.42	–	101
30	Chalcocite	0.03	78.79	0.07	0.11	0.01	–	20.08	–	0.023	0.461	–	100
34	Chalcocite	0.00	79.48	0.05	0.08		–	19.94	–	0.019	0.458	–	100
36	Chalcocite	0.06	70.52	0.05		0.01	–	18.04	–	–	0.243	0.01	89
24	Chalcocite	0.03	80.02	0.04	0.07	0.00	–	20.57	–	–	0.316	0.00	101
44	Chalcocite	0.04	78.28	0.05		0.00	–	20.30	0.007	0.016	0.224	0.01	99
48	Chalcocite	0.12	78.35	0.05	0.06		–	19.94	0	0	0.447	–	99
49	Chalcocite	0.12	78.45	0.05	0.05		–	19.84	0.008	0.017	0.46	–	99
50	Chalcocite	0.01	78.30	0.07	0.06		–	19.85	0	0.012	0.425	0.02	99
51	Chalcocite	0.03	79.48	0.07	0.09	0.01	–	20.07	0.001	0.009	0.416	0.00	100
52	Chalcocite	0.02	78.93	0.05	0.04	0.01	–	20.06	0	0	0.399	–	100
53	Chalcocite	0.04	79.07	0.07	0.09	0.00	–	20.57	0	0.011	0.235	–	100
54	Chalcocite	0.01	79.01	0.04	0.06	0.01	–	19.84	0	0.013	0.425	0.01	99
26	Chalcocite	0.03	80.33	0.07	0.03		–	20.12	0.002	0.018	0.494	–	101
63	Chalcocite	0.16	76.85	0.04	0.05		–	20.13	0	0	0.117	–	97
64	Chalcocite	0.09	79.49	0.05	0.12		–	20.22	0	0.009	0.096	–	100
65	Chalcocite	0.03	79.66	0.04	0.02		–	20.65	0.017	0.041	0.136	–	101
66	Chalcocite	0.04	79.45	0.08	0.04		–	20.63	0.016	0.019	0.073	0.01	100
75	Chalcocite	0.50	78.04	0.03	0.11		–	19.92	0	0.002	0.034	–	99
76	Chalcocite	0.71	78.28	0.07		0.00	–	19.95	0	0.052	0.019	–	99
82	Chalcocite	0.20	78.11	0.05	0.00	0.01	–	19.80	0	0	0.028	–	98
84	Chalcocite	0.00	78.54	0.05	0.05		–	20.48	0.017	0	0.026	0.01	99
69	Chalcocite	0.09	79.41	0.05	0.02		–	20.58	0	0	0.061	–	100
70	Chalcocite	0.05	79.50	0.04			–	20.68	0	0.015	0.038	0.01	100
94	Chalcocite	1.81	77.05	0.03	1.41	0.02	–	20.51	0	0.028	0.036	–	101
57	Chalcocite	0.05	78.83	0.07			–	20.89	0	0.013	0.037	0.02	100
58	Chalcocite	0.01	78.46	0.04	0.02	0.01	–	20.63	0	0.009	0.029	–	99
59	Chalcocite	0.02	78.62	0.03	0.02		–	20.69	0.024	0.021	0.061	0.00	99
60	Chalcocite	0.43	77.57	0.04	0.06	0.02	–	20.40	0	0.031	0.037	0.00	99
61	Chalcocite	1.41	74.41	0.03	0.02	0.00	–	19.77	0	0.023	0.088	0.01	96
95	Chalcocite	0.04	78.85	0.05	0.03		–	20.40	0.007	0.021	0.028	–	99
9	Chalcocite	0.05	79.61	0.01	0.10		–	20.28	0	0.023	0.021	–	100
204	Chalcocite	0.03	67.78	0.02	0.00	0.00	–	32.11	0	0	0.0503	0.00	100
205	Chalcocite	0.01	67.76	0.02		0.00	–	32.16	0.0036	0.0063	0.0435	–	100
206	Chalcocite	0.04	68.22	0.06	0.05		–	31.59	0	0	0.0434	0.01	100
215	Chalcocite	0.03	67.40	0.03	0.05	0.01	–	32.36	0.0024	0	0.1263	–	100
216	Chalcocite	0.04	67.38	0.06			–	32.40	0.0029	0	0.1177	0.00	100
217	Chalcocite	0.03	67.43	0.06	0.04		–	32.31	0	0	0.1206	0.01	100
239	Chalcocite	0.07	66.95	0.05	0.05	0.00	–	32.73	0	0.0012	0.1366	–	100
240	Chalcocite	0.00	66.84	0.01	0.05		–	32.97	0	0	0.1365	–	100
241	Chalcocite	0.03	67.45	0.03	0.03		–	32.30	0	0.0061	0.1414	0.00	100
242	Chalcocite	0.01	67.35	0.05	0.08	0.01	–	32.48	0.0008	0.0083	0.0101	0.00	100
243	Chalcocite	0.00	67.53	0.03	0.04	0.00	–	32.35	0	0.0014	0.031	0.00	100
10	Chalcopyrite	28.65	34.32	0.02	0.05	0.04	–	34.65	0.014	0.046	0.029	–	98
12	Chalcopyrite	28.66	34.01	0.00	0.09	0.05	–	34.80	0.042	0.05	0.014	0.00	98
72	Chalcopyrite	27.79	34.11	0.03	0.05	0.04	–	34.27	0	0.041	0	–	96
73	Chalcopyrite	28.20	34.17	0.00	0.09	0.05	–	34.48	0.021	0.035	0.005	0.01	97
74	Chalcopyrite	28.39	34.27	0.05		0.06	–	34.20	0	0.005	0.017	0.01	97
77	Chalcopyrite	0.22	77.59	0.06	0.07		–	19.92	0	0.01	0.022	0.01	98
151	Chalcopyrite	25.06	25.37	0.01	0.05	0.04	–	49.45	0	0.0097	0.0066	–	100
152	Chalcopyrite	25.12	25.43	0.00		0.03	–	49.40	0	0.0065	0.0129	–	100
153	Chalcopyrite	24.37	25.25	0.60	0.03	0.03	–	49.69	0.0046	0.0053	0.01	0.00	100
154	Chalcopyrite	24.58	25.25	0.03	0.01	0.05	0	50.07	0	0.0033	0.0053	0.00	100

APPENDIX B
MINERAL CHEMISTRY DATA

	Detection limit (ppm)	111	152	195	346	87	101	47	189	230	76	157	
No.	**Mineral**	**Fe**	**Cu**	**Zn**	**As**	**Co**	**Ni**	**S**	**Pb**	**Bi**	**Ag**	**Sb**	**Total**
155	Chalcopyrite	24.97	25.26	0.01	0.05	0.03	0	49.66	0.001	0.0065	0.0124	–	100
156	Chalcopyrite	24.52	25.33	0.01	0.04	0.05	0	50.04	0.0003	0.0028	0.008	–	100
157	Chalcopyrite	24.91	25.24	0.05	0.05	0.04	0.0023	49.69	0.0018	0.0149	0.0054	–	100
158	Chalcopyrite	24.67	25.17	0.02	0.02	0.04	–	50.06	0.0096	0	0.0138	–	100
159	Chalcopyrite	24.80	25.11	0.03	0.04	0.03	–	49.98	0	0.0115	0.0039	–	100
160	Chalcopyrite	24.82	25.33	0.02	0.02	0.04	–	49.76	0.0029	0.0059	0.012	0.00	100
161	Chalcopyrite	25.13	25.59	0.04	0.05	0.04	–	49.13	0.0028	0.0056	0.0074	0.00	100
162	Chalcopyrite	25.44	25.33	0.02	0.03	0.03	–	49.13	0.0024	0.0047	0	0.00	100
163	Chalcopyrite	24.70	25.09	0.01	0.05	0.04	–	50.08	0.0083	0.0125	0.0039	–	100
164	Chalcopyrite	24.71	25.12	0.02	0.02	0.05	–	50.08	0	0.0012	0.0027	–	100
165	Chalcopyrite	24.72	25.18	0.00	0.02	0.04	–	50.04	0	0	0.0046	–	100
166	Chalcopyrite	24.34	25.01	0.01	0.05	0.04	–	50.52	0.0079	0.0106	0.0045	0.00	100
167	Chalcopyrite	24.60	25.24	0.10	0.05	0.02	–	49.98	0.0063	0.0052	0	–	100
168	Chalcopyrite	24.89	25.31	0.02		0.04	–	49.74	0.009	0	0.0045	0.00	100
169	Chalcopyrite	24.83	25.34	0.02	0.08	0.05	–	49.64	0.0112	0.0095	0.0114	0.00	100
170	Chalcopyrite	25.05	25.24	0.01	0.03	0.04	–	49.61	0	0.0065	0.0153	–	100
15	Bornite	10.41	63.05	0.04	0.01	0.02	–	25.50	0	0.065	0.21	–	99
16	Bornite	10.86	63.52	0.07	0.02	0.02	–	25.45	0.028	0.085	0.261	–	100
18	Bornite	10.57	62.89	0.05		0.03	–	25.46	0.022	0.022	0.118	0.00	99
19	Bornite	10.69	63.15	0.01	0.02	0.01	–	25.35	0	0.053	0.131	–	99
20	Bornite	10.62	63.07	0.00	0.00	0.00	–	25.40	0	0.032	0.104	–	99
21	Bornite	10.64	63.46	0.01		0.01	–	25.31	0	0.077	0.172	–	100
22	Bornite	10.45	63.11	0.06	0.06	0.01	–	25.37	0	0.039	0.141	0.02	99
23	Bornite	10.25	62.80	0.04	0.07	0.01	–	25.31	0.005	0.068	0.151	0.00	99
31	Bornite	10.51	62.58	0.03		0.02	–	25.08	–	0.065	0.323	–	99
32	Bornite	10.55	62.40	0.05	0.07	0.02	–	25.28	–	0.102	0.341	–	99
33	Bornite	10.45	61.77	0.03		0.01	–	25.10	–	0.101	0.405	0.00	98
25	Bornite	10.36	63.61	0.03	0.02	0.02	–	25.13	–	0.06	0.365	0.01	100
37	Bornite	10.24	62.26	0.07	0.00	0.02	–	25.19	–	0.024	0.291	0.00	98
38	Bornite	10.33	62.31	0.03	0.08	0.01	–	25.46	–	0.074	0.306	–	99
41	Bornite	10.05	62.04	0.01	0.03	0.02	–	25.40	–	0.072	0.312	–	98
42	Bornite	9.38	55.48	0.04	0.02	0.01	–	22.20	–	0.091	0.374	–	88
43	Bornite	10.40	62.32	0.05	0.03	0.02	–	25.05	–	0.046	0.33	–	98
45	Bornite	10.37	61.99	0.03		0.02	–	25.20	–	0.093	0.319	–	98
46	Bornite	10.05	61.23	0.02	0.03	0.01	–	25.11	0.032	0.028	0.325	0.01	97
47	Bornite	9.96	61.25	0.04		0.01	–	24.97	–	0.053	0.312	–	97
55	Bornite	10.45	62.92	0.04	0.04	0.03	–	25.13	0.037	0.013	0.3	0.00	99
56	Bornite	10.18	62.06	0.03	0.04	0.01	–	24.82	–	0.092	0.292	–	98
207	Bornite	10.00	51.14	0.02	0.01	0.02	–	38.71	–	0	0.1	–	100
208	Bornite	9.81	51.46	0.02	0.04	0.01	–	38.52	0.0074	0.0041	0.1165	0.01	100
209	Bornite	9.89	50.82	0.01	0.00	0.01	–	39.13	0	0.0179	0.1149	0.00	100
210	Bornite	9.95	50.97	0.01	0.03	0.02	–	38.91	0	0.0004	0.1046	0.00	100
211	Bornite	9.88	50.75	0.03	0.04	0.02	–	39.17	0.0022	0.0096	0.1079	–	100
212	Bornite	9.90	50.85	0.04	0.03	0.02	–	39.06	0	0.0093	0.1099	–	100
213	Bornite	9.89	50.76	0.01	0.05	0.02	–	39.16	0.0067	0	0.1062	–	100
214	Bornite	9.97	50.66	0.01	0.02	0.03	–	39.20	0	0.0033	0.1036	–	100
39	sulfarsenide	7.35	2.82	–	42.93	16.49	9.501	18.24	0.026	0	0	–	97
40	sulfarsenide	8.26	3.12	–	43.37	13.99	11.415	17.58	0.018	0	0.005	–	98
218	Arsenopyrite	34.87	0.18	–	32.88	0.06	0.0034	31.99	0.0081	0.0036	0	–	100
219	Arsenopyrite	34.65	0.33	–	32.42	0.06	0	32.53	0.0066	0	0.0007	–	100
220	Arsenopyrite	34.55	0.29	–	32.50	0.05	0	32.60	0	0	0	–	100
221	Arsenopyrite	34.54	0.68	–	32.18	0.08	0.0173	32.50	0.0017	0	0	–	100
222	Arsenopyrite	31.88	5.00	0.02	29.47	0.40	0	33.21	0.0052	0	0.0177	0.01	100
223	Arsenopyrite	34.37	0.78	0.00	32.35	0.07	0	32.43	0.0022	0	0.0004	0.01	100
224	Arsenopyrite	33.54	1.74	0.01	31.42	0.19	0.0089	33.07	0	0.0111	0.0024	0.01	100
225	Arsenopyrite	35.01	0.04	0.01	33.23	0.08	0	31.62	0.0005	0	0.0005	–	100
226	Arsenopyrite	35.03	0.09	–	32.99	0.06	0	31.81	0	0	0	0.01	100

APPENDIX B
MINERAL CHEMISTRY DATA

	Detection limit (ppm)	111	152	195	346	87	101	47	189	230	76	157	
No.	**Mineral**	**Fe**	**Cu**	**Zn**	**As**	**Co**	**Ni**	**S**	**Pb**	**Bi**	**Ag**	**Sb**	**Total**
227	Arsenopyrite	34.16	0.27	0.00	33.17	0.05	0	32.34	0.0053	0.0037	0	0.00	100
228	Arsenopyrite	34.60	0.12	0.00	33.05	0.03	0	32.19	0.0107	0	0.0002	0.00	100
229	Arsenopyrite	33.87	0.03	0.00	33.54	0.54	1.0186	31.00	0	0	0	–	100
230	Arsenopyrite	34.33	0.06	0.00	33.04	0.07	0	32.47	0.0135	0	0.0038	0.00	100
231	Arsenopyrite	34.03	0.04	0.01	33.17	0.34	0.098	32.32	0	0	0	–	100
232	Arsenopyrite	34.51	0.03	0.01	33.11	0.14	0.0527	32.14	0	0	0.0047	0.00	100
233	Arsenopyrite	34.27	0.03	0.00	32.94	0.23	0.0757	32.47	0	0	0.0007	–	100
234	Arsenopyrite	34.04	0.04	0.00	32.99	0.35	0.3061	32.27	0.0118	0	0	–	100
235	Arsenopyrite	34.64	0.03	0.00	33.20	0.22	0.0221	31.88	0.0095	0	0	–	100
236	Arsenopyrite	33.36	0.00	0.02	33.56	0.71	0.5986	31.74	0	0	0.0057	–	100
237	Arsenopyrite	34.39	0.12	0.01	33.27	0.06	0.0071	32.14	0	0.0012	0	0.00	100
238	Arsenopyrite	31.50	5.37	0.00	30.75	0.08	0.0044	32.28	0.0017	0.0023	0.0117	0.00	100
92	Arsenopyrite	34.40	0.00	0.00	44.07	0.12	0.011	19.59	0	0.017	0	0.01	98
93	Arsenopyrite	33.87	0.00	0.03	43.54	0.15	0	19.79	0	0.018	0	0.01	97
79	Arsenopyrite	32.72	0.00	0.00	44.30	0.56	0.104	19.58	0	0	0	0.01	97
80	Arsenopyrite	33.46	0.05	0.03	43.80	0.05	0.023	19.64	0.045	0	0.015	0.00	97
81	Arsenopyrite	29.72	0.10	0.00	44.50	2.46	1.772	19.05	0.036	0.027	0.002	0.00	98
8	Arsenopyrite	35.01	0.01	0.00	43.63	0.08	0.02	19.85	0.042	0.029	0.006	0.00	99
83	Arsenopyrite	32.32	0.23	0.00	44.41	0.71	0.42	19.21	0.023	0	–	0.00	97
34	Sphalerite	5.79	0.00	43.31	0.00	0.01	0.0061	50.87	0	0.0047	–	0.00	100
35	Sphalerite	5.68	0.00	43.76	0.02	0.01	0	50.53	0	0.011	–	0.00	100
36	Sphalerite	5.86	0.00	44.05	0.06	0.01	0.0112	50.00	0	0.01	–	–	100
37	Sphalerite	5.35	0.00	43.87	0.02	0.01	0.0051	50.74	0	0.0071	–	–	100
38	Sphalerite	5.65	0.00	43.67		0.01	0	50.67	0	0.0013	–	–	100
39	Sphalerite	5.56	0.00	43.91	0.02	0.01	0.0019	50.49	0.0019	0.007	–	–	100
103	Sphalerite	1.16	0.03	48.45	0.06		0.0031	50.28	–	0.0097	–	0.00	100
104	Sphalerite	1.32	0.00	48.02	0.06	0.01	0	50.58	–	0.0038	–	0.00	100
105	Sphalerite	1.08	0.00	48.73	0.08	0.01	0.005	50.10	–	0.003	–	–	100
115	Sphalerite	1.02	0.01	48.50	0.13		0.0015	50.32	–	0.0159	–	–	100
116	Sphalerite	1.56	0.01	47.04	0.19		0.0061	51.19	0.0058	0	–	–	100
117	Sphalerite	1.29	0.07	47.96	0.06		0	50.62	–	0.0058	–	0.00	100
118	Sphalerite	1.39	0.00	47.78	0.13		0	50.71	–	0.0029	–	0.00	100
119	Sphalerite	1.12	0.00	47.96	0.16		0	50.75	–	0	–	0.00	100
120	Sphalerite	1.24	0.01	47.97	0.14	0.01	0	50.61	–	0.0129	–	0.00	100
131	Sphalerite	1.40	0.00	48.53	0.05		0.0042	50.01	–	0.0098	–	0.00	100
132	Sphalerite	1.40	0.00	48.19	0.02	0.01	0.0093	50.36	–	0.0007	–	0.00	100
171	Sphalerite	2.76	0.41	46.68	0.10	0.01	0.0007	50.01	0.0012	0.019	–	0.00	100
172	Sphalerite	3.22	0.61	46.29	0.08	0.02	0.0139	49.76	0.0053	0.0124	–	0.00	100
173	Sphalerite	3.02	0.32	47.08	0.07	0.02	0.0112	49.47	0.0013	0.0104	–	0.00	100
174	Sphalerite	2.76	0.78	46.55	0.02	0.00	0.0068	49.87	0	0.0077	–	0.00	100
175	Sphalerite	2.50	2.37	45.58	0.06		0	49.47	0	0.0049	–	0.01	100
176	Sphalerite	3.08	1.08	46.28	0.15	0.00	0.0026	49.39	0.0076	0.0061	–	0.00	100
177	Sphalerite	3.15	0.04	46.75	0.13	0.01	0	49.90	0.0133	0.0068	–	0.00	100
178	Sphalerite	3.09	0.03	46.83	0.09	0.01	0.0143	49.93	0.0067	0.0064	–	0.01	100
179	Sphalerite	3.27	0.07	46.87	0.06		0.0065	49.70	0.007	0	–	0.00	100
180	Sphalerite	3.04	0.22	46.96	0.01		0.0022	49.77	0.0041	0.0018	–	0.00	100
181	Sphalerite	3.14	0.02	46.76	0.11	0.01	0.0095	49.95	0	0.0043	–	0.00	100
182	Sphalerite	3.03	0.04	46.74	0.10	0.01	0	50.07	0.0035	0.0073	–	–	100
183	Sphalerite	2.77	2.78	44.60	0.07	0.00	0.0048	49.74	0.0012	0	0.0259	–	100
184	Sphalerite	2.55	0.99	46.23	0.12	0.01	0	50.09	0.0096	0.0026	–	0.00	100
185	Sphalerite	3.08	0.04	46.82	0.07		0	49.97	0	0.0109	–	–	100
186	Sphalerite	1.56	0.48	48.10	0.09		0.0034	49.73	0.0331	0.0081	–	–	100
187	Sphalerite	2.57	0.98	45.99	0.13		0	50.31	0.0192	0.0027	–	0.01	100
19	Sphalerite	3.59	0.00	46.02	0.09	0.00	0.0086	50.27	0	0.0117	–	–	100
20	Sphalerite	3.23	0.00	45.64	0.10	0.01	0.0127	50.87	0.1329	0	–	0.00	100
21	Sphalerite	3.14	0.00	46.09	0.09	0.01	0.0056	50.66	0	0.0048	–	0.00	100
22	Sphalerite	3.46	0.00	45.28	0.09		0	51.17	0	0.0056	–	–	100

APPENDIX B
MINERAL CHEMISTRY DATA

	Detection limit (ppm)	111	152	195	346	87	101	47	189	230	76	157	
No.	**Mineral**	**Fe**	**Cu**	**Zn**	**As**	**Co**	**Ni**	**S**	**Pb**	**Bi**	**Ag**	**Sb**	**Total**
23	Sphalerite	4.13	–	44.30	0.82	0.01	0.0064	49.10	1.6219	0.0187	–	–	100
24	Sphalerite	3.41	–	46.25	0.06	0.01	0	50.21	0.0542	0	–	0.00	100
33	Sphalerite	5.75	–	44.10		0.00	0	50.13	–	0.0102	–	–	100
40	Recrystallized framboidal pyrite	33.32	–	0.04	0.02	0.06	0	66.55	–	0.0058	–	–	100
41	Recrystallized framboidal pyrite	33.81	–	1.32	0.04	0.08	0.0122	64.72	–	0.0025	–	0.00	100
42	Recrystallized framboidal pyrite	39.98	–	0.12	0.00	0.10	0.0193	59.76	–	0.009	0.0054	0.00	100
43	Recrystallized framboidal pyrite	33.39	–	0.02	0.09	0.07	0.0221	66.38	–	0.0098	0	0.01	100
44	Recrystallized framboidal pyrite	34.18	–	0.04	0.06	0.06	0.0078	65.64	0.0076	0.0084	0	0.00	100
45	Recrystallized framboidal pyrite	33.51	–	0.04	0.05	0.05	0.0153	66.31	–	0.0041	0.0043	0.00	100
46	Recrystallized framboidal pyrite	33.31	–	0.05	0.04	0.07	0.0148	66.50	–	0.013	0	0.01	100
47	Recrystallized framboidal pyrite	33.68	–	0.02	0.07	0.07	0.0262	66.12	–	0.0156	0.0005	0.00	100
48	Recrystallized framboidal pyrite	33.64	0.02	0.01	0.04	0.04	0.0074	66.23	0.0115	0.0045	0	0.01	100
49	Recrystallized framboidal pyrite	33.62	–	0.02	0.06	0.06	0.0155	66.21	–	0.0162	0	0.01	100
50	Recrystallized framboidal pyrite	34.60	–	0.02	0.06	0.07	0	65.23	–	0.007	0	0.01	100
51	Recrystallized framboidal pyrite	34.65	–	0.00	0.09	0.06	0.0105	65.17	–	0.0083	0.0034	0.00	100
54	Recrystallized framboidal pyrite	35.02	–	0.00	0.05	0.06	0.0037	64.84	0.0059	0.0088	–	0.01	100
55	Recrystallized framboidal pyrite	33.84	–	0.00	0.03	0.06	0.0078	66.06	–	0	–	0.00	100
56	Recrystallized framboidal pyrite	33.31	–	0.01	0.05	0.07	0.0095	66.55	–	0.0106	–	0.00	100
57	Recrystallized framboidal pyrite	34.80	–	0.01	0.09	0.05	0.0049	65.02	0.0001	0.0052	–	0.01	100
58	Recrystallized framboidal pyrite	34.42	–	0.02	0.00	0.06	0	65.49	–	0.0014	–	0.00	100
59	Recrystallized framboidal pyrite	33.30	–	0.00	0.01	0.05	0	66.63	–	0.0048	–	0.00	100
60	Recrystallized framboidal pyrite	34.29	0.02	0.00	0.06	0.06	0.0078	65.54	0.013	0.0082	–	0.00	100
61	Recrystallized framboidal pyrite	34.18	0.00	0.01	0.06	0.08	0.0291	65.63	–	0.0137	–	0.00	100
62	Recrystallized framboidal pyrite	33.48	0.00	0.00	0.02	0.05	0.0013	66.44	–	0.0057	–	0.00	100
4	Recrystallized framboidal pyrite	33.56	0.00	0.00	0.08	0.07	0.004	66.29	–	0.0058	–	0.00	100
5	Recrystallized framboidal pyrite	33.92	0.01	0.01	0.02	0.06	0.0046	65.98	–	0.0067	–	0.00	100
6	Recrystallized framboidal pyrite	33.32	0.00	0.00	0.05	0.06	0.0209	66.52	–	0.0073	0.0029	–	100
7	Recrystallized framboidal pyrite	34.20	0.00	0.00	0.08	0.07	0.0129	65.63	–	0.0095	0	0.00	100
8	Recrystallized framboidal pyrite	33.42	0.00	0.02	0.09	0.06	0.0241	66.37	–	0.0158	0.005	0.00	100
9	Recrystallized framboidal pyrite	33.98	0.02	0.06	0.03	0.05	0.0098	65.81	0.0083	0.0256	0.0006	0.00	100
10	Recrystallized framboidal pyrite	34.24	0.01	0.02	0.05	0.07	0.0249	65.58	–	–	–	–	100
11	Recrystallized framboidal pyrite	33.84	0.01	0.01	0.10	0.12	0.0263	65.89	–	0.0033	0.0017	0.00	100
12	Recrystallized framboidal pyrite	33.67	0.00	0.00	0.02	0.05	0	66.24	–	0.009	0.0013	0.00	100
52	Recrystallized framboidal pyrite	33.39	0.01	0.01	0.38	0.04	0.1785	65.98	–	0.0081	–	–	100
53	Recrystallized framboidal pyrite	33.49	0.00	0.07	0.08	0.06	0.0156	66.27	–	0.0102	–	0.00	100
71	Recrystallized framboidal pyrite	33.72	0.00	0.01	0.06	0.06	0.0586	66.09	–	0.0056	0.001	–	100
72	Recrystallized framboidal pyrite	34.02	0.00	0.00	0.15	0.04	0.0607	65.72	–	0.0041	0	–	100
73	Recrystallized framboidal pyrite	33.57	0.00	0.00	0.30	0.05	0.1255	65.94	–	0.0085	0	–	100
74	Recrystallized framboidal pyrite	33.60	0.03	0.02	0.37	0.05	0.1888	65.74	–	0.01	0	–	100
75	Recrystallized framboidal pyrite	33.53	0.00	0.00	0.02	0.05	0.1251	66.27	–	0.012	0.0002	–	100
90	Recrystallized framboidal pyrite	32.76	0.01	0.00	0.06	0.05	0.0374	67.07	–	0.003	0	–	100
91	Recrystallized framboidal pyrite	32.52	0.01	0.00	0.06	0.04	0.0474	67.31	–	0.0119	0.0017	0.00	100
92	Recrystallized framboidal pyrite	32.88	0.00	0.00	0.14	0.05	0.0089	66.90	–	0.0037	0.0097	0.00	100
93	Recrystallized framboidal pyrite	33.09	0.00	0.00	0.11	0.06	0.0158	66.72	–	0.0073	0.0007	0.00	100
94	Recrystallized framboidal pyrite	33.14	0.02	0.00	0.10	0.05	0.0177	66.67	–	0.0092	0	0.00	100
95	Recrystallized framboidal pyrite	33.95	0.00	0.03	0.11	0.06	0	65.84	–	0.0098	0.0049	0.00	100
96	Recrystallized framboidal pyrite	33.71	0.00	0.00	0.14	0.05	0.095	65.99	–	0.0144	0.0007	0.00	100
97	Recrystallized framboidal pyrite	33.21	0.00	0.01	0.26	0.05	0.1262	66.34	–	0.0094	0	0.00	100
98	Recrystallized framboidal pyrite	33.06	0.00	0.01	0.27	0.05	0.1012	66.50	–	0.0074	0	0.00	100
99	Recrystallized framboidal pyrite	32.72	0.01	0.00	0.23	0.06	0.0616	66.90	0.0042	0.0099	0.0032	0.00	100
112	Recrystallized framboidal pyrite	34.00	0.00	0.00	0.40	0.05	0.1061	65.43	0	0.0084	0.0042	0.00	100
113	Recrystallized framboidal pyrite	32.74	0.00	0.00	0.35	0.06	0.0954	66.74	0	0.0026	0.004	0.00	100
114	Recrystallized framboidal pyrite	33.77	0.00	0.00	0.32	0.05	0.0951	65.75	0	0.0169	0.0035	0.00	100
124	Recrystallized framboidal pyrite	33.46	0.00	0.00	0.23	0.06	0.0497	66.18	0.0022	0.0145	0.002	0.00	100
125	Recrystallized framboidal pyrite	33.41	0.00	0.01	0.36	0.04	0.1962	65.97	0.0021	0.0074	0	0.00	100
126	Recrystallized framboidal pyrite	33.86	0.00	0.00	0.06	0.05	0.0946	65.94	0	0.0027	0.0026	0.00	100
127	Recrystallized framboidal pyrite	34.47	0.00	0.00	0.51	0.06	0.3271	64.63	0	0.0079	0.0034	0.00	100

APPENDIX B
MINERAL CHEMISTRY DATA

	Detection limit (ppm)	111	152	195	346	87	101	47	189	230	76	157	
No.	**Mineral**	**Fe**	**Cu**	**Zn**	**As**	**Co**	**Ni**	**S**	**Pb**	**Bi**	**Ag**	**Sb**	**Total**
128	Recrystallized framboidal pyrite	34.28	–	0.00	0.16	0.05	0.1605	65.33	0	0.0164	0.0036	–	100
129	Recrystallized framboidal pyrite	33.15	–	0.02	0.58	0.05	0.3334	65.86	0	0.0061	0	–	100
130	Recrystallized framboidal pyrite	34.29	–	0.00	0.29	0.05	0.1298	65.23	0	0.0091	0	–	100
1	Recrystallized framboidal pyrite	33.72	–	0.01	0.13	0.04	0.0331	66.06	0	0.0084	0	–	100
2	Recrystallized framboidal pyrite	33.78	–	0.00	0.06	0.06	0.0617	66.03	0	0.0035	0	–	100
3	Recrystallized framboidal pyrite	33.88	–	0.01	0.05	0.05	0.0329	65.97	0	0.0118	0	–	100
13	Recrystallized framboidal pyrite	33.41	–	0.04	0.24	0.05	0.0602	66.19	0	0.0009	0	–	100
14	Recrystallized framboidal pyrite	34.26	–	0.00	0.28	0.05	0.0794	65.32	0	0.0063	0	–	100
15	Recrystallized framboidal pyrite	34.08	–	0.00	0.26	0.06	0.0966	65.49	0	0.0115	0	–	100
16	Recrystallized framboidal pyrite	33.95	–	0.00	0.20	0.06	0.0794	65.71	0	0	0	–	100
17	Recrystallized framboidal pyrite	34.21	–	0.09	0.17	0.05	0.0544	65.41	0	0.006	0.0015	–	100
18	Recrystallized framboidal pyrite	35.70	–	0.04		0.05	0.0219	64.16	0.0205	0.0104	0	–	100
25	Recrystallized framboidal pyrite	34.57	0.04	0.22	0.06	0.06	0.0122	65.02	0	0.0043	0	–	100
26	Recrystallized framboidal pyrite	34.08	0.25	0.35	0.12	0.07	0.0236	65.08	0	0.0123	0	–	100
27	Recrystallized framboidal pyrite	33.98	0.00	0.00	0.04	0.05	0.0014	65.91	0	0.0057	0.0106	–	100
28	Recrystallized framboidal pyrite	34.30	0.01	0.01	0.06	0.05	0.0057	65.56	0	0.0021	0	–	100
29	Recrystallized framboidal pyrite	34.13	0.01	0.02	0.18	0.06	0.066	65.52	0	0.0091	0	–	100
30	Recrystallized framboidal pyrite	34.03	0.02	0.00	0.06	0.07	0.0139	65.80	0.0029	0.0021	0.0026	–	100
31	Recrystallized framboidal pyrite	34.64	0.00	0.00	0.05	0.06	0.0019	65.24	0	0.0001	0.0012	–	100
32	Recrystallized framboidal pyrite	33.63	0.00	0.00	0.45	0.05	0.2419	65.61	0	0.009	0	–	100
138	Covellite	0.11	50.61	0.05	0.27	0.00	0	48.83	0.0439	0.0097	0.0572	–	100
139	Covellite	0.13	49.39	0.05	0.59		0	48.80	0.9716	0.0061	0.0604	–	100
140	Covellite	0.16	46.77	0.02	2.04		0.0005	48.06	2.8788	0.0093	0.0738	–	100
141	Covellite	0.15	50.54	0.04	0.25		–	48.93	0	0.0105	0.0739	–	100
142	Covellite	0.29	51.38	0.13	0.02	0.00	–	48.07	0.0095	0.0052	0.0926	–	100
143	Covellite	0.63	50.98	0.25	0.05	0.00	–	48.01	0.0033	0.0045	0.0739	–	100
144	Covellite	0.96	49.94	0.33	0.08	0.01	–	48.47	0.101	0.0025	0.1093	–	100
145	Covellite	15.51	10.48	31.81	0.12	0.02	–	41.91	0.0652	0.0055	0.0642	0.02	100
146	Covellite	1.22	50.36	0.49	0.04		–	47.82	0.0038	0	0.0658	–	100
147	Covellite	23.38	38.46	0.64	0.01	0.04	–	37.35	0.0143	0.0026	0.0819	0.01	100
148	Covellite	12.66	43.67	0.33	0.10	0.02	–	43.13	0.0054	0.0041	0.0589	0.01	100
149	Covellite	1.28	50.64	0.15	0.02	0.00	–	47.77	0.0292	0.0066	0.1048	0.00	100
150	Covellite	1.42	50.70	0.12	0.11		–	47.48	0.0505	0.0034	0.1107	0.00	100
202	Covellite	0.41	50.24	0.03	0.25		0.0001	48.93	0.0644	0.0133	0.0583	0.01	100
203	Covellite	0.25	3.10	0.00	24.82	0.01	0.0443	35.73	35.958	0.0887	0	0.00	100
11	Covellite	0.68	65.17	0.03	0.55	0.01	0	31.64	1.508	0	0.26	0.00	100
13	Covellite	0.49	66.36	0.03	0.34		0	31.09	0.838	0.017	0.257	0.00	99
63	unnamed	10.27	0.00	–	0.78		0	0.28	0	81.016	7.6453	0.00	100
64	unnamed	6.97	0.00	–	7.71		0	1.53	0	79.044	2.8612	1.88	100
65	unnamed	13.21	0.00	–	5.65		0		0	76.661	2.9971	1.48	100
66	unnamed	15.84	0.97	–	3.00	1.66	0	1.11	0	73.401	3.7231	0.30	100
67	unnamed	11.89	1.55	–	4.80	0.34	0.2931		0	77.147	3.9795	0.00	100
68	unnamed	49.88	0.00	–	5.09	1.19	0		0	43.699	0	0.14	100
69	unnamed	43.45	0.38	–	1.97		0		0	54.203	0	0.00	100
70	unnamed	48.68	0.00	–	1.84		0.3522		0	47.564	1.5671	0.00	100
76	Galena	0.07	0.00	–	26.46	0.00	0	36.74	36.611	0.1144	–	–	100
77	Galena	0.07	0.02	–	24.95		0.0168	36.87	37.968	0.1162	–	–	100
78	Galena	0.06	–	–	24.80		0.0169	36.85	38.132	0.1414	–	–	100
79	Galena	0.17	–	–	25.93		0.0102	36.69	37.097	0.1018	–	–	100
80	Galena	0.46	–	–	25.64		0.0172	37.25	36.478	0.1496	–	–	100
81	Galena	0.33	0.05	–	24.47		0.0036	36.92	38.108	0.1136	–	–	100
82	Galena	0.23	–	0.05	26.15	0.02	0.0032	36.96	36.481	0.1131	–	–	100
83	Galena	0.05	–	–	25.37		0	37.16	37.302	0.1203	–	–	100
84	Galena	0.03	–	–	26.12	0.01	0.0411	37.11	36.541	0.1445	–	–	100
85	Galena	0.02	–	–	25.30		0.0146	36.93	37.584	0.1475	–	–	100
86	Galena	0.06	0.01	–	26.20	0.01	0.0061	37.00	36.596	0.1194	–	–	100
87	Galena	0.05	–	–	25.07		–	36.85	37.893	0.138	–	–	100

APPENDIX B
MINERAL CHEMISTRY DATA

	Detection limit (ppm)	111	152	195	346	87	101	47	189	230	76	157	
No.	**Mineral**	**Fe**	**Cu**	**Zn**	**As**	**Co**	**Ni**	**S**	**Pb**	**Bi**	**Ag**	**Sb**	**Total**
88	Galena	0.06	0.00	–	26.71		0.0025	36.87	36.221	0.1307	–	–	100
89	Galena	0.01	0.01	–	26.70	0.00	0	36.49	36.63	0.1547	–	–	100
100	Galena	0.07	0.00	–	26.23		0	37.03	36.524	0.1427	–	–	100
101	Galena	0.13	0.04	–	25.43		0.0019	37.07	37.199	0.1309	–	–	100
102	Galena	0.07	0.00	–	26.45	0.00	0.0048	36.78	36.57	0.1285	–	–	100
106	Galena	0.02	0.00	–	26.20	0.01	0	36.88	36.768	0.1338	–	–	100
107	Galena	0.04	0.00	–	26.22	0.02	0	36.81	36.805	0.1139	–	–	100
108	Galena	0.04	0.00	–	24.70	0.01	0	36.83	38.302	0.1218	–	–	100
109	Galena	0.04	0.00	–	24.81		0.0286	36.91	38.076	0.1308	–	–	100
110	Galena	0.04	0.00	–	25.40		0	36.98	37.454	0.1268	–	–	100
111	Galena	0.16	0.00	–	26.00	0.02	0.0154	36.41	37.25	0.1524	–	–	100
121	Galena	0.01	0.01	0.02	25.78		0	36.57	37.478	0.1328	–	–	100
122	Galena	0.03	0.00	0.00	26.02		0	36.62	37.204	0.1232	–	–	100
123	Galena	0.02	0.00	0.00	25.98		0.0045	36.74	37.092	0.157	–	–	100
133	Galena	0.02	0.01	0.07	25.09		0.0098	36.87	37.83	0.0977	–	–	100
134	Galena	0.03	0.00	0.39	25.73		0	36.89	36.82	0.1343	–	–	100
135	Galena	0.00	0.06	0.17	26.10	0.01	0.0166	36.59	36.951	0.1124	–	0.00	100
136	Galena	0.06	0.22	0.80	25.88		0	36.33	36.567	0.1349	–	–	100
137	Galena	0.05	0.40	1.03	25.64		0.0329	35.96	36.773	0.121	–	–	100
188	Galena	0.00	0.03	0.05	25.87		0.0013	36.29	37.635	0.1193	–	–	100
189	Galena	0.02	0.00	0.00	25.78	0.00	0	36.31	37.76	0.1316	–	–	100
190	Galena	0.00	0.02	0.00	26.27		0	35.92	37.682	0.104	–	–	100
191	Galena	0.01	0.00	0.00	26.58		0	35.80	37.49	0.1234	–	–	100
192	Galena	0.07	0.01	0.00	26.35		0.0218	36.05	37.386	0.1151	–	–	100
193	Galena	0.00	0.02	0.00	26.31		0	36.19	37.351	0.1316	–	–	100
194	Galena	0.01	0.00	0.12	26.07		0.0123	36.30	37.343	0.1427	–	–	100
195	Galena	0.04	0.04	0.22	25.72		0	36.14	37.722	0.1107	–	–	100
196	Galena	0.00	0.00	0.00	26.46		0.0093	36.74	36.65	0.1287	–	0.01	100
197	Galena	0.02	0.00	0.02	26.53	0.03	0	36.35	36.932	0.1195	–	–	100
198	Galena	0.01	0.01	0.14	26.32	0.00	0.0197	36.38	36.998	0.1258	–	–	100
199	Galena	0.03	0.04	0.02	26.54		0.0037	36.35	36.892	0.1283	–	–	100
200	Galena	0.00	0.05	0.01	26.32		0.0082	36.34	37.154	0.1131	–	–	100
201	Galena	0.01	0.02	0.01	26.31		0.0037	36.58	36.964	0.0962	–	–	100

Note 1: – = 0.00

Note 2: concentrations are given in wt. %